FIBRE BRAGG GRATINGS AND THEIR SENSING APPLICATIONS

PING LU

Your file Votre référence
ISBN: 978-0-494-33431-7
Our file Notre référence
ISBN: 978-0-494-33431-7

Fibre Bragg Gratings and Their Sensing Applications

by

Ping Lu

A Thesis Submitted in Partial Fulfillment of
the Requirements for the Degree of

Master of Science

Department of Physics and Physical Oceanography
Memorial University of Newfoundland

September 18, 2007

St. John's Newfoundland

Abstract

Fibre Bragg gratings have been investigated for their sensing of environmental parameters, including temperature, humidity, axial strain, bending and flow rate. The changes in different environmental parameters result in monotonous spectrum shift of the fibre Bragg gratings. The sensitivities of acrylate-coating fibre Bragg grating on temperature, axial strain and flow rate are 0.0102 nm/°C, 0.732 pm/με and 0.0092 nm/cm^3s^{-1}, respectively. The sensitivities of polyimide-coating fibre Bragg grating on temperature, humidity and axial strain are 0.0094 nm/°C, 2.60 pm/%RH and 0.99 pm/με, respectively. The experimental results on the polarization characterization indicate that the maximum polarization dependent loss of a single mode polyimide-coated fibre Bragg grating and the Bragg wavelengths corresponding to the fast-axis mode and slow-axis mode of a polarization maintaining fibre Bragg grating will increase with the rising temperature.

We propose and demonstrate for the first time that a new multiplexed fibre Bragg grating sensor system is capable of achieving simultaneous measurement of different measurands. The multiplexed sensor system, which consists of two fibre Bragg gratings with different coating materials of acrylate and polyimide, exhibits distinguishable characteristics to different measurands owing to the unique hygroscopic and swelling properties of the polyimide coating. Experimental results on the simultaneous measurement of temperature and saccharinity/salinity indicated corresponding

sensitivities of 0.0102 nm/°C and 0.0012 nm/°Bx / 0.0038 nm/%. Simultaneous measurement of temperature and axial strain has also been achieved.

The results achieved in this thesis are promising for applications on multi-measurand, quasi-distributed and in-situ sensing measurement using multiplexed FBG sensors.

Acknowledgements

I gratefully acknowledge Dr. Qiying Chen for giving me this great opportunity to work and learn in his research group and for his invaluable guidance, constructive discussion and perpetual encouragement throughout my two years of graduate study.

I would like to thank Professor John Whitehead, Professor Martin Plumer and Professor John Lewis for their courses and instructions. I am grateful to thank the School of Graduate Studies at the Memorial University of Newfoundland, the physics department and my supervisor for financial support.

I would also like to thank my father and mother, for the countless years of support. Most special thanks go to my wife, Jing Ping, for her support and encouragement.

Contents

List of Tables

List of Figures

Chapter 1

Fibre Bragg Gratings

1.1 Introduction

With the increasing interests in the studies of all-fibre systems, fibre Bragg gratings (FBGs) have received considerable attention recently. A FBG is a type of distributed Bragg reflector constructed in a short segment of optical fibre that reflects specific wavelengths of light and transmits all the other components. Photosensitivity phenomenon in optical fibres was first observed by the interference between counter-propagating waves inside the fibre core in 1978 [1]. The first FBG was imprinted in Ge-doped silica single mode fibre by transverse coherent 244 nm UV beams produced by a tunable excimer-pumped dye laser with a frequency-doubled crystal [2]. Since then, FBGs have been revolutionizing telecommunication and impacting the optical fibre

sensor field due to their unique advantages and versatility as in-fibre devices. Nowadays FBGs have become important components in a variety of lightwave communication applications such as fibre laser [3, 4], fibre amplifier [5], fibre Bragg filter [6-9], the wavelength division multiplexers/demultiplexers [10, 11], and dispersion compensation [12]. Meanwhile FBGs have been considered as excellent sensor elements which are suitable for measuring many environmental parameters, including temperature and strain [13], torsion and bending [14], refractive index [15], pressure [16], current [17] and solution concentration [18].

In this chapter, basic physical properties of FBGs will be discussed as well as their fabrication techniques. A mathematical model will be used to simulate the spectral properties of FBGs. Applications of FBGs for sensing environmental parameters will be reviewed.

1.2 Properties of Fibre Bragg Grating

1.2.1 Optical Properties

A FBG consists of a periodic modulation of the refractive index in the core of an optical fibre. The phase fronts of this type of fibre gratings are perpendicular to the fibre longitudinal axis and the grating planes are of a constant period (Fig. 1-1). Light guided along the core of an optical fibre will be scattered by each grating plane. If the Bragg condition ($2\Lambda \sin\theta = n\lambda$, Λ, the spacing between the grating planes; θ, the angle

between the incident ray and the scattering planes; n is an integer; λ, light wavelength) is not satisfied, the reflected light from each of the subsequent planes becomes progressively out of phase and will eventually cancel out. When the Bragg condition is satisfied, the contributions of reflected light from each grating plane add constructively in the backward direction to form a back-reflected peak with a centre wavelength defined by the grating parameters, which is usually referred to as Bragg wavelength.

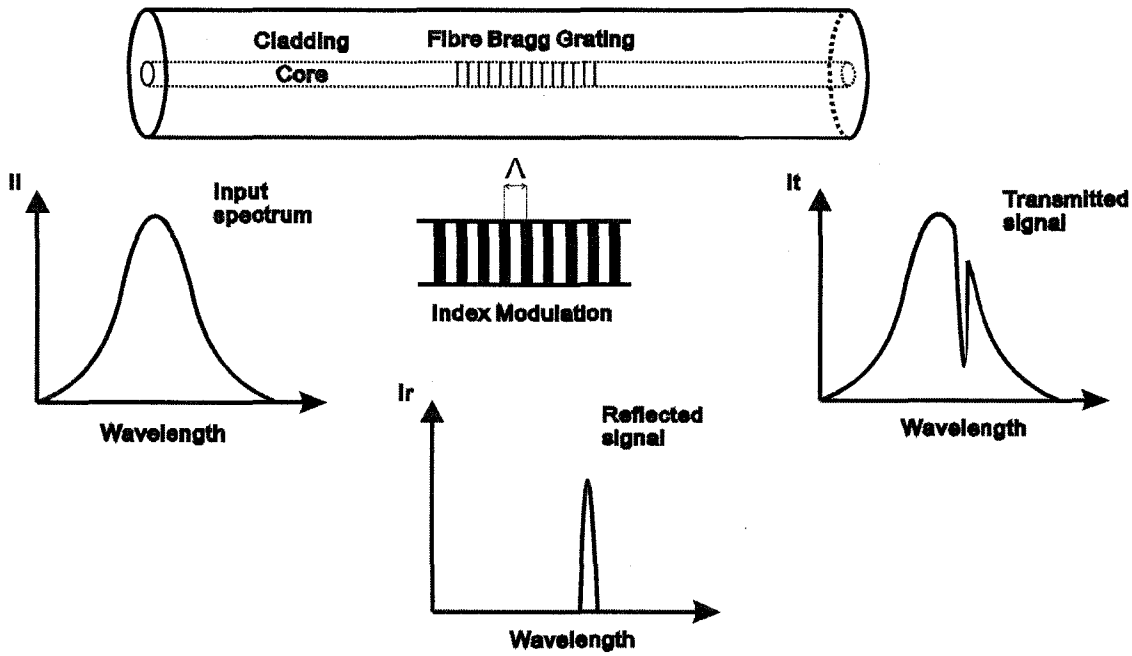

Figure 1-1: Illustration of a uniform fibre Bragg grating.

The Bragg grating condition is simply the requirement to satisfy both energy and momentum conservation. Energy conservation ($\hbar\omega_f = \hbar\omega_i$) requires that the frequencies of the incident radiation and the reflected radiation should be the same. Momentum conservation requires that the incident wave vector, $\vec{k}_i$, plus the grating wave vector, $\vec{K}$,

equal the wave vector of the scattered radiation $\vec{k}_f$, which can be simply expressed as

$$\vec{k}_i + \vec{K} = \vec{k}_f \tag{1-1}$$

where the grating wave vector $\vec{K}$ has a direction normal to the grating plane with a magnitude $2\pi/\Lambda$, Λ is the grating spacing as shown in Fig. 1-1.

The diffracted wave vector is equal in magnitude but opposite in direction to the incident wave vector. Hence, the momentum conservation condition becomes

$$2\left(\frac{2\pi n_{eff}}{\lambda_B}\right) = \frac{2\pi}{\Lambda} \tag{1-2}$$

which simplifies to the first-order Bragg condition

$$\lambda_B = 2n_{eff}\Lambda \tag{1-3}$$

where the Bragg grating wavelength, λ_B, is the free-space centre wavelength of the input light that will be back-reflected from the Bragg grating, and n_{eff} is the effective refractive index of the fibre core at the free-space centre wavelength.

Consider a uniform FBG formed within the core of an optical fibre with an average refractive index n_0. The refractive index profile can be expressed as [19]

$$n(x) = n_0 + \Delta n \cos\left(\frac{2\pi x}{\Lambda}\right) \tag{1-4}$$

where Δn is the amplitude of the induced refractive index perturbation, and x is the distance along the fibre longitudinal axis. The reflectivity of a grating with constant modulation amplitude and period is given by the following expression [19]:

$$R(l,\lambda)=\frac{\Omega^2\sinh^2(sl)}{\Delta k^2\sinh^2(sl)+s^2\cosh^2(sl)} \tag{1-5}$$

where $R(l,\lambda)$ is the reflectivity which is a function of the grating length l, and wavelength λ; Ω is the coupling coefficient; $\Delta k = k - \pi/\lambda$ is the detuning wave vector; $k = 2\pi n_0/\lambda$ is the propagation constant; and $s=\sqrt{\Omega^2-\Delta k^2}$. The coupling coefficient Ω for the sinusoidal variation of index perturbation along the fibre axis is given by

$$\Omega=\frac{\pi\Delta n\eta(V)}{\lambda} \tag{1-6}$$

where $\eta(V)$ is a function of the normalized frequency V of the fibre that represents the fraction of the fibre mode power contained in the core, $\eta(V)\approx 1-V^{-2}$. The normalized frequency V can be expressed as [19]

$$V=\left(2\pi/\lambda\right)a\left(n_{co}^2-n_{cl}^2\right)^{1/2} \tag{1-7}$$

where a is the core radius, n_{co} and n_{cl} are refractive indices of the core and cladding, respectively.

At the Bragg grating centre wavelength, there is no wave-vector detuning and $\Delta k = 0$, therefore, the expression for the reflectivity becomes

$$R(l,\lambda)=\tanh^2(\Omega l). \tag{1-8}$$

The reflectivity increases as the change in the induced index of refraction increases. Similarly, as the length of the grating increases so does the resultant reflectivity. A

simulated reflection spectrum as a function of the wavelength detuning is shown in Fig. 1-2. The side lobes of the resonance are due to multiple reflections to and from opposite ends of the grating region.

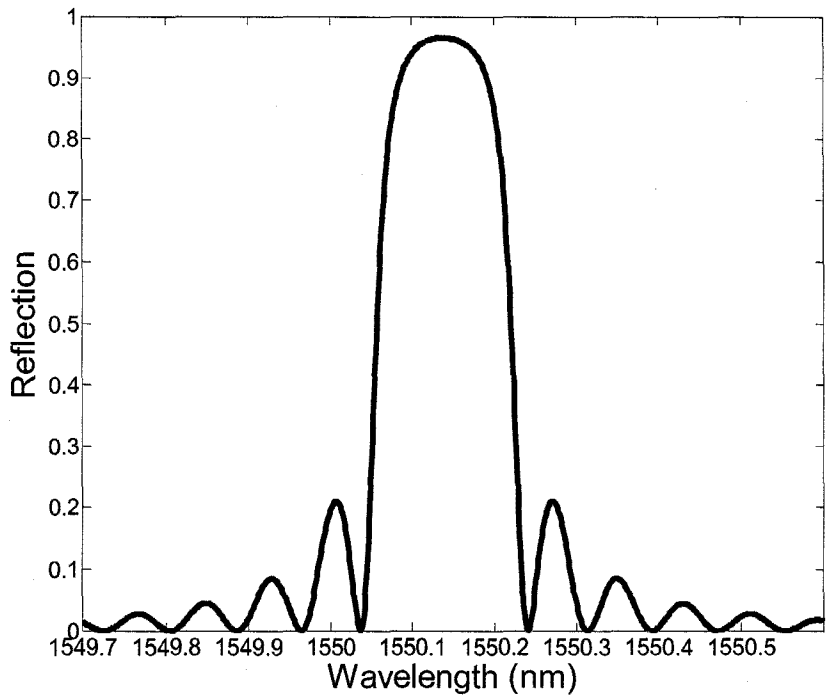

Figure 1-2: Simulation of reflection spectrum of a Bragg grating as a function of wavelength detuning.

Bragg gratings written in a highly photosensitive fibre exhibit a pronounced transmission feature on the short-wavelength side of the Bragg peak (Fig. 1-3). This feature is only observable in the transmission spectrum and only the main peak is visible in the reflection spectrum. Accordingly this structure must be due to the light leaving the fibre from the side. Radiation-mode coupling as a loss mechanism on core-mode transmission has been suggested to explain this phenomenon [20, 21]. For the cylindrical

cladding-air interface, the transmission spectrum of the Bragg grating consists of multiple sharp peaks that modulate the radiation-mode coupling. The light energy in the grating will be coupled to other modes at shorter wavelengths: some will be reflected or absorbed, and others will be radiated away from the fibre. These interactions are seen as a series of many transmission dips in the spectrum at wavelengths that are shorter than the Bragg wavelength.

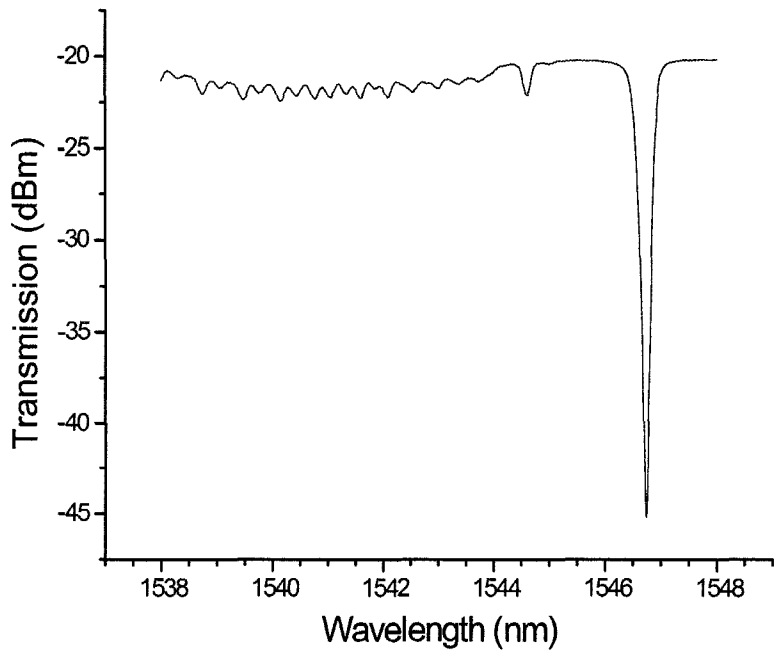

Figure 1-3: Transmission spectrum of a strong fibre Bragg grating exhibiting loss to radiation modes on the short-wavelength side.

1.2.2 Photosensitivity and Fabrication Techniques

Photosensitivity in optical fibre refers to a permanent change in the index of refraction of

the fibre core when exposed to light with characteristic wavelength and intensity that depends on the core material. Photosensitivity in optical fibres has significant importance, which has resulted in a new class of in-fibre phase structures, such as FBGs.

The first observation of index of refraction changes was noticed in germanosilica fibres and was reported by Hill *et al.* [1, 22] in 1978. They described a permanent grating written in the core of the fibres by an argon ion laser line at 488 nm launched into the fibre. This particular grating had a very weak index modulation, which was estimated to be of the order of 10^{-6} resulting in a narrow-band reflection filter at the writing wavelength. In 1989, Meltz *et al.* [2] showed that a strong index of refraction change occurred when a germanium-doped fibre was exposed to UV light close to the absorption peak of a germania-related defect at a wavelength range of 240–250 nm in 1989. In recent years, direct optical inscription of high quality gratings into the core of optical fibres has been achieved by various techniques, three of the most useful being the interferometric technique, phase mask technique, and point-by-point exposure to ultraviolet laser light.

Bragg gratings have been written in many types of optical fibres using various methods. However, the mechanism of index change is not fully understood. Several models have been proposed for these photoinduced refractive-index changes, for instance, the color centre model [23, 24], the dipole model [25], the compaction model [26], the stress-relief model [27-29]. The only common elements in these theories are that the germanium–oxygen vacancy defects, Ge–Si or Ge–Ge, are responsible for the photoinduced index changes.

Photosensitivity of optical fibres can be thought of as a measure of the amount of refractive index change in a fibre core. It is desirable to fabricate photoinduced devices in standard optical fibres for compatibility with existing systems, however, the standard single mode telecommunication fibres, doped with 3% germania, typically display weak index changes of 10^{-5}, far below the demand of the order of 10^{-4}. Hydrogen loading (hydrogenation) [30-32], flame brushing [33], boron co-doping [34, 35], and short wavelength light source [36, 37] have been used for enhancing the photosensitivity in silica optical fibres.

Different FBG fabrication techniques can be classified as internal inscription and external inscription techniques. Bragg gratings were first fabricated using the internally writing technique [1, 22]. These techniques adopt relatively simple experimental setup, however, these gratings are limited to operate at a Bragg wavelength coinciding with the excitation laser wavelength. Nowadays the internal inscription technique has been superseded by the external inscription technique due to the intrinsic limitation of internally written gratings. There are three main externally written fabrication techniques: the interferometric technique, the phase mask technique, and the point-by-point technique.

The interferometric fabrication technique, the first external writing technique of forming Bragg gratings in photosensitive fibres, was demonstrated by Meltz *et al.* [2], who utilized an interferometer that split the incoming UV light into two beams and then recombined them to form an interference pattern. The interference pattern was used to expose a photosensitive fibre, inducing a refractive index modulation in the core. Fibre

Bragg gratings have been fabricated using both the amplitude-splitting and the wave-front-splitting interferometers.

One of the most effective methods for inscribing Bragg gratings in photosensitive fibre is the phase-mask technique [38, 39]. This method employs a diffractive optical element (phase mask) to spatially modulate the UV writing beam. The phase-mask grating has a one-dimension surface-relief structure fabricated in a high-quality fused silica flat transparent to the UV writing beam. The profile of the periodic gratings is chosen such that, when an UV beam is incident on the phase mask, the zero-order diffracted beam is suppressed to less than a few percent of the transmitted power. In addition, the diffracted plus and minus first orders are maximized to contain, typically, more than 35% of the transmitted power. A near-field fringe pattern is produced by the interference of the plus and minus first-order diffracted beams. The period of the fringes is one-half that of the mask. The interference pattern photoimprints a refractive-index modulation in the core of a photosensitive optical fibre placed in contact with or in close proximity immediately behind the phase mask. A cylindrical lens may be used to focus the fringe pattern along the fibre core. The phase mask greatly reduces the complexity of the fibre grating fabrication system. The simplicity of using only one phase mask provides a robust and an inherently stable method for reproducing FBGs.

The point-by-point technique [40] for fabricating Bragg gratings is accomplished by inducing a change in the index of refraction a step at a time along the core of the fibre. Each grating plane is produced separately by a focused single pulse from an excimer laser. A single pulse of UV light from an excimer laser passes through a mask containing a slit.

A focusing lens images the slit onto the core of the optical fibre from the side and the refractive index of the core in the irradiated fibre section increases locally. The fibre is then translated through a distance Λ corresponding to the grating pitch in a direction parallel to the fibre axis and the process is repeated to form the grating structure in the fibre core. Essential to the point-by-point fabrication technique is a very stable and precise submicron translational system. The main advantage of the point-by-point writing technique lies in its flexibility to alter the Bragg grating parameters. The disadvantage of the point-by-point technique is that it is a tedious process. Because it is a step-by-step procedure, this method requires a relatively long process time. Errors in the grating spacing due to thermal effects and/or small variations in the fibre's strain can occur. This limits the gratings to a very short length.

According to the different grating pitch or tilt, fibre Bragg gratings can be classified into the common Bragg reflector, the blazed Bragg grating, and the chirped Bragg grating. The simplest and most used FBG is the Bragg reflector, which has a constant pitch. A typical spectral response of a uniform period is shown in Fig. 1-4. The Bragg reflector can function as a narrowband transmission or reflection filter and sensor applications [41-44]. The blazed grating has phase fronts tilted with respect to the fibre axis. The applications of blazed gratings are in mode conversion [45] and sensing field [15, 46]. The chirped grating has an aperiodic pitch, displaying a monotonic increase in the spacing between grating planes. The applications of the chirped Bragg gratings are for dispersion compensation in high-bit-rate transmission systems [47, 48] and sensing elements [49-52].

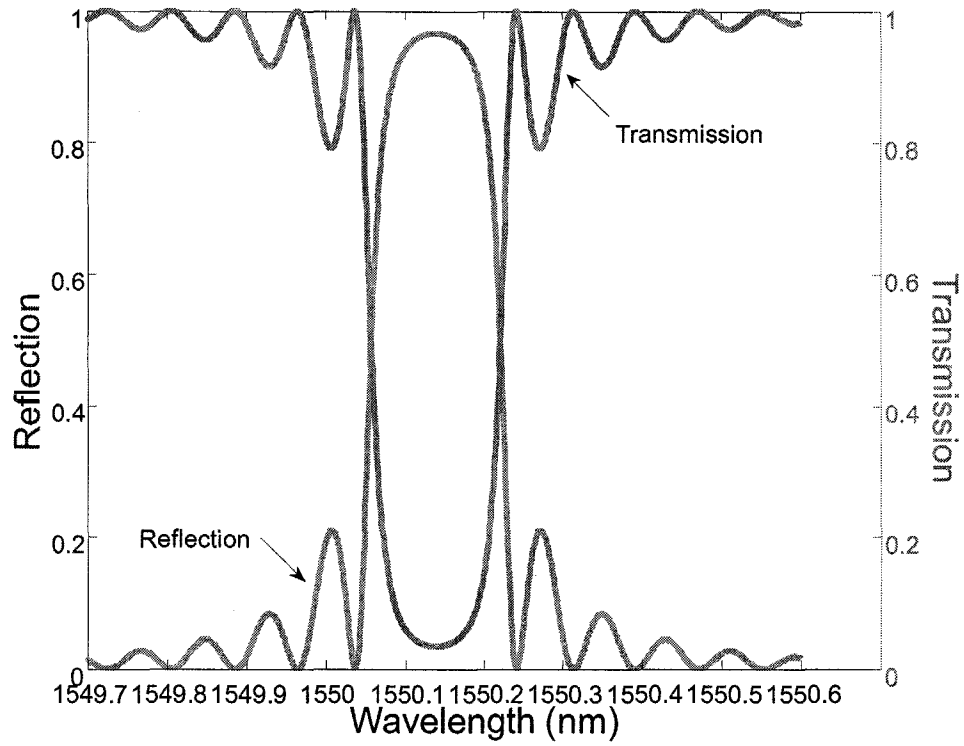

Figure 1-4: Simulated typical spectral response of a Bragg reflector with a uniform period.

1.3 Mathematical Models of Fibre Bragg Gratings

In order to gain a better understanding of Bragg gratings, it is very important to have a qualitative picture of the basic interactions between light and grating [53]. Since a fibre grating is simply an optical diffraction grating, its effect upon a light wave incident on the grating at an angle can be described by the grating equation [54]

$$n\sin\theta_2 = n\sin\theta_1 + m\frac{\lambda}{\Lambda} \tag{1-9}$$

where θ_2 is the angle of the diffracted wave and the integer m determines the diffraction

order (Fig. 1-5). Equation (1-9) determines the directions into which constructive interference occurs.

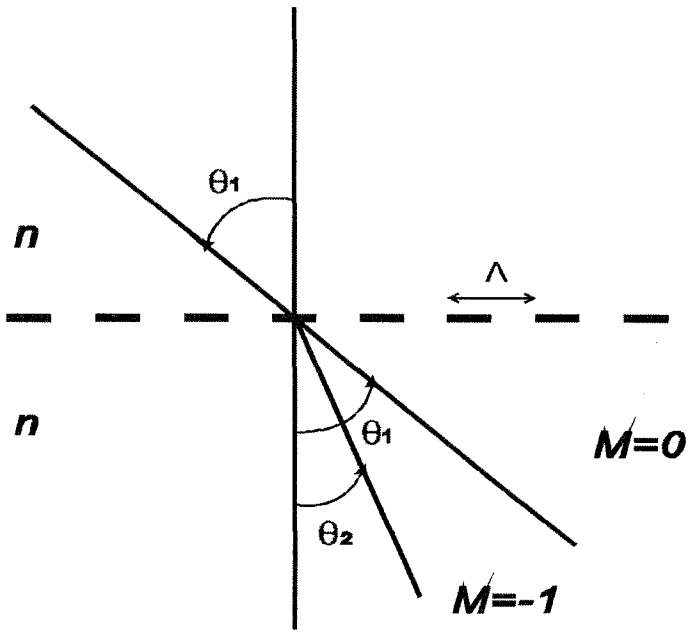

Figure 1-5: The diffraction of a light wave by a grating.

Figure 1-6 illustrates a simple Bragg grating in which light energy is coupled from a mode incident at a bounce angle of θ_1 into the same mode traveling in the opposite direction at an angle $\theta_2 = -\theta_1$. Using n_{co} and n_{cl} to denote the core and cladding refractive indices respectively, we can rewrite Eqn. (1-9) above in terms of the mode propagation constant $\beta = (2\pi/\lambda) n_{eff}$ where $n_{eff} = n_{co} \sin\theta$ as:

$$\beta_2 = \beta_1 + m\frac{2\pi}{\Lambda}. \qquad (1\text{-}10)$$

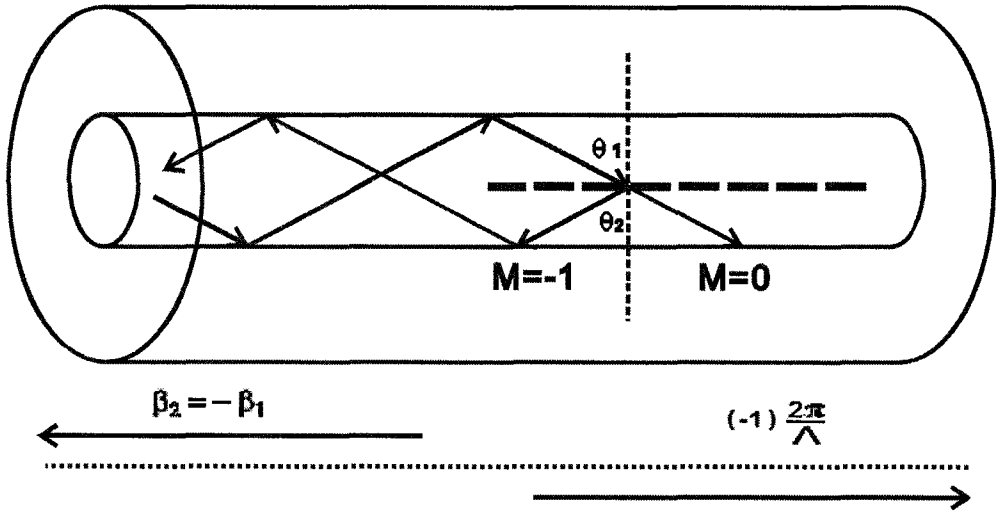

Figure 1-6: Illustration of core-mode Bragg reflection by a fibre Bragg grating.

Considering the dominant first-order diffraction in the fibre grating for which $m=-1$, and realizing that $\beta_2 < 0$, we determine that the resonant wavelength condition for reflection of a mode of index $n_{eff,1}$ into a mode of index $n_{eff,2}$ is:

$$\lambda = \left(n_{eff,1} + n_{eff,2}\right)\Lambda . \tag{1-11}$$

If the two models are identical, the Bragg reflection condition becomes

$$\lambda_B = 2n_{eff}\Lambda . \tag{1-12}$$

Coupled-mode theory is a straightforward and powerful tool for analyzing the diffraction efficiency and spectral dependence of fibre gratings [55, 56]. Coupled-mode theory can accurately models the optical properties of most fibre gratings [53].

For simplicity, we assume that the perturbation to the effective refractive index n_{eff} of the guided mode(s) can be described by [53]

$$\delta n_{eff}(z) = \delta \overline{n}_{eff}(z)\left\{1 + v\cos\left[\frac{2\pi}{\Lambda}z + \phi(z)\right]\right\} \quad (1\text{-}13)$$

where $\delta \overline{n}_{eff}$ is the "DC" index change spatially averaged over a grating period, v is the fringe visibility of the index change, Λ is the nominal period, and $\phi(z)$ describes grating chirp.

By using the ideal-mode approximation in the coupled-mode theory, we assume that the transverse component of the electric field can be written as a superposition of the ideal modes labeled, such that

$$\vec{E}_t(x,y,z,t) = \sum_j \left[A_j(z)\exp(iB_j z) + B_j(z)\exp(-iB_j z)\right]\vec{e}_{jt}(x,y)\exp(-i\omega t) \quad (1\text{-}14)$$

where $A_j(z)$ and $B_j(z)$ are slowly varying amplitudes of the jth mode traveling in the $+z$ and $-z$ directions, respectively. The transverse mode field $\vec{e}_{jt}(x,y)$ describes the bound core or radiation LP modes or cladding modes. While the modes are orthogonal in an ideal waveguide and hence, do not exchange energy, the presence of a dielectric perturbation causes the modes to be coupled such that the amplitudes A_j and B_j of the jth mode evolve along the z axis according to

$$\frac{dA_j}{dz} = i\sum_k A_k(K_{kj}^t + K_{kj}^z)\exp\left[i(B_k - B_j)z\right] + i\sum_k B_k(K_{kj}^t - K_{kj}^z)\exp\left[-i(B_k + B_j)z\right] \quad (1\text{-}15)$$

$$\frac{dB_j}{dz} = -i\sum_k A_k(K_{kj}^t - K_{kj}^z)\exp\left[i(B_k + B_j)z\right] - i\sum_k B_k(K_{kj}^t + K_{kj}^z)\exp\left[-i(B_k - B_j)z\right] \quad (1\text{-}16)$$

where K_{kj}^t is the transverse coupling coefficient between modes j and k given by

$$K_{kj}^{t}(z)=\frac{\omega}{4}\iint_{\infty}dxdy\Delta\varepsilon(x,y,z)\vec{e}_{kt}(x,y)\vec{e}_{jt}^{*}(x,y) \tag{1-17}$$

where $\Delta\varepsilon$ is the perturbation to the permittivity, $\Delta\varepsilon\cong 2n\delta n$. The longitudinal coefficient K_{kj}^{z} is analogous to K_{kj}^{t}, and the longitudinal coefficient is usually neglected.

In most fibre gratings the induced index change $\delta n(x,y,z)$ is approximately uniform across the core and nonexistent outside the core. We can thus describe the core index by an expression similar to Eqn. (1-13), but with $\delta\overline{n}_{eff}(z)$ replaced by $\delta\overline{n}_{co}(z)$. If we define two new coefficients

$$\sigma_{kj}(z)=\frac{\omega n_{co}}{2}\delta\overline{n}_{co}(z)\iint_{core}dxdy(x,y,z)\vec{e}_{kt}(x,y)\vec{e}_{jt}^{*}(x,y) \tag{1-18}$$

$$k_{kj}(z)=\frac{v}{2}\sigma_{kj}(z) \tag{1-19}$$

where σ is a "DC" (period-averaged) coupling coefficient and k is an "AC" coupling coefficient, then the general coupling coefficient can be written

$$K_{kj}^{t}(z)=\sigma_{kj}(z)+2k_{kj}(z)\cos\left[\frac{2\pi}{\Lambda}z+\phi(z)\right]. \tag{1-20}$$

Equations (1-15) – (1-20) are the coupled-mode equations that can be used to describe FBG spectra. Equations (1-15) and (1-16) may be simplified by making the "synchronous approximation" [56]. The resulting equations can be written as

$$\frac{dR}{dz}=i\hat{\sigma}R(z)+ikS(z) \tag{1-21}$$

$$\frac{dS}{dz} = -i\hat{\sigma}S(z) - ik^* R(z) \tag{1-22}$$

where R and S are $R(z) \equiv A(z)\exp\left(i\delta z - \phi/2\right)$ and $S(z) \equiv B(z)\exp\left(-i\delta z + \phi/2\right)$, respectively. In these equations k is the "AC" coupling coefficient from Eqn. (1-19) and $\hat{\sigma}$ is a general "DC" self-coupling coefficient defined as

$$\hat{\sigma} \equiv \delta + \sigma - \frac{1}{2}\frac{d\phi}{dz} \tag{1-23}$$

The detuning δ, which is independent of z for all gratings, is defined to be

$$\begin{aligned} \delta &\equiv \beta - \frac{\pi}{\Lambda} \\ &= \beta - \beta_D \\ &= 2\pi n_{eff}\left(\frac{1}{\lambda} - \frac{1}{\lambda_D}\right) \end{aligned} \tag{1-24}$$

where $\lambda_D \equiv 2n_{eff}\Lambda$ is the "design wavelength" for Bragg scattering by an infinitesimally weak grating ($n_{eff} \to 0$) with a period Λ. Note that when $\delta = 0$, we find $\lambda = 2n_{eff}\Lambda$, which is the Bragg condition predicted by the qualitative grating picture above. The "DC" coupling coefficient σ is defined in Eqn. (1-18). Absorption loss in the grating can be described by a complex coefficient σ, where the power loss coefficient is $\alpha = 2\,\mathrm{Im}(\sigma)$. Light not reflected by the grating experiences a transmission loss of $10\log_{10}(e)\alpha$ with a unit of dB/cm. Finally, the derivative $\left(1/2\right)d\phi/dz$ describes possible chirp of the grating period.

For a single mode Bragg reflection grating, the following simple relations hold [53]:

$$\sigma = \frac{2\pi}{\lambda}\delta\bar{n}_{eff} \tag{1-25}$$

$$\begin{aligned} k &= k^* \\ &= \frac{\pi}{\lambda} v\delta\bar{n}_{eff} \end{aligned} \tag{1-26}$$

If the grating is uniform along z, then $\delta\bar{n}_{eff}$ is a constant and $d\phi/dz = 0$, and thus k, σ, and $\hat{\sigma}$ are constants. Therefore, Eqns. (1-21) and (1-22) are coupled first-order ordinary differential equations with constant coefficients, for which closed-form solutions can be found when appropriate boundary conditions are specified. The reflectivity of a uniform fibre grating of length L can be found by assuming a forward-going wave incident from $z = -\infty$ [when $R\left(-L/2\right) = 1$] and requiring that no backward-going wave exists for $z \geq L/2$ [when $S\left(L/2\right) = 0$]. The amplitude and power reflection coefficients $\rho = S\left(-L/2\right) / R\left(-L/2\right)$ and $r = |\rho|^2$, respectively, can then be shown as [55, 56]

$$\rho = \frac{-k\sinh\left(\sqrt{k^2 - \sigma^2}L\right)}{\sigma\sinh\left(\sqrt{k^2 - \sigma^2}L\right) + i\sqrt{k^2 - \sigma^2}\cosh\left(\sqrt{k^2 - \sigma^2}L\right)} \tag{1-27}$$

and

$$r = \frac{\sinh^2\left(\sqrt{k^2 - \sigma^2}L\right)}{\cosh^2\left(\sqrt{k^2 - \sigma^2}L\right) - \frac{\sigma^2}{k^2}}. \tag{1-28}$$

In an optical fibre, the power of the transmitted signal E_{total} is the combination of

fast axis (x) and slow axis (y) modes.

$$E_{total} = \left(E_x \cdot \rho_x\right)^2 + \left(E_y \cdot \rho_y\right)^2 \tag{1-29}$$

Total transmission coefficient T_{total} can be written as:

$$T_{total} = \frac{1}{2} r_x + \frac{1}{2} r_y \tag{1-30}$$

The transmission and reflection spectra of FBGs inscribed on a standard single mode telecommunication fibre (SMF-28, Corning Inc.) and a polarization maintaining fibre (PANDA, Fujikura Ltd.) are shown in Figs. 1-4 and 1-7, respectively.

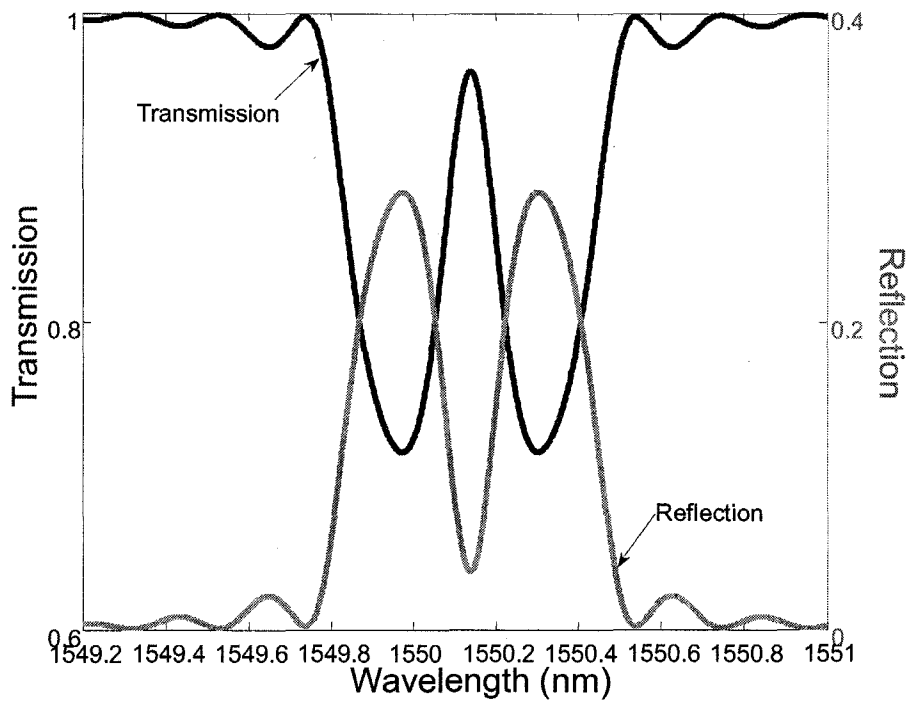

Figure 1-7: Simulation results of transmission and reflection spectra of a polarization maintaining fibre Bragg grating.

1.4 Fibre Bragg Grating Sensors

Sensors based on FBGs have attracted considerable attention since the early stage of the discovery. FBG sensors exceed other conventional electric sensors in many aspects, for instance, immunity to electromagnetic interference, compact sizes, light weight, flexibility, stability, high temperature tolerance, and resistance to harsh environment. Additional advantages of FBG sensors include very low insertion loss, narrowband wavelength reflection, linearity in response over many orders of magnitude and compatibility with the existing fibre optics system, especially their absolute wavelength-encoding of measurand information, making FBG sensors interrupt immune [57].

Fibre Bragg grating sensors can measure many physical parameters. Among these, strain [58-61] and temperature [62, 63] measurements are major fields of interest. Meltz and Morey propounded that the shift in the Bragg grating wavelength was mainly due to strain and temperature changes [64]. The strain response is induced due to both the fractional change in a grating period due to the physical elongation of the optical fibre and the change in fibre index due to photoelastic effects. The thermal response is induced due to both the inherent thermal expansion of the fibre material and the temperature dependence of the refractive index. It is apparent that any shift in Bragg wavelength is the sum of the strain and temperature factors. The sensing measurements of other measurands can be realized by transforming to the strain and temperature factors. FBG sensors used to measure humidity [65, 66], vibration [67], pressure [68-70], and

refractive index [71-74] have been reported recently. No report on the saccharinity measurement using a FBG sensor has been found so far. In this thesis, saccharinity and salinity sensing measurements of a polyimide-coating FBG will be carried out. Owing to the unique properties of the polyimide material, a saccharinity FBG sensor and a salinity FBG sensor are realized. Furthermore, the thesis reports that a steel-bar mounted FBG can be considered as an excellent bending sensor and water flow meter.

As discussed above, FBGs respond to change in both strain and temperature. Therefore it is necessary to discriminate these effects in order to measure each physical parameter or to measure both simultaneously. Great efforts have been focused on this and various methods have been proposed. A simple and practical approach is to use a reference grating or grating pairs [16, 75]. The reference grating or grating pairs, which is isolated from one parameter, e.g., strain, is placed near the sensor FBG. The reference grating can be on the same fibre as the sensor FBG [76]. Another method is to use two FBGs with a large difference in their Bragg wavelengths, which show different responses to the same measurands [77]. FBGs written on fibres of different diameters have also been proposed, which give different strain responses, while the temperature responses are the same [78, 79]. A sensing head for simultaneous measurement of strain and temperature is demonstrated based on two Bragg gratings arranged in a twisted configuration [80]. By writing FBG with close wavelengths in undoped and boron doped fibres, different temperature sensitivities are obtained while the strain sensitivities remain the same [13]. In this thesis, a method using two different polymer-coated FBGs in a multiplexed sensor system to simultaneously measure axial strain and temperature is

proposed. Furthermore this polymer-coated FBGs scheme realized the elimination of the cross sensitivities of saccharinity/salinity and temperature for the first time.

The sensing applications of fibre Bragg grating polarization effects have been studied in the past. When temperature and transverse force affect an FBG, they lead to comparable effects in the spectral evolution. The polarization dependent loss (PDL) and differential group delay (DGD) wavelength evolutions could be used to discriminate the temperature and transverse force [81]. The PDL in single mode FBG was found to be quite sensitive to the temperature and strain changes. It is possible to discriminate the temperature and strain effects by measuring the resonance wavelength shift and the PDL changes [82]. Simultaneous strain and temperature sensor based on the numerical reconstruction of polarization maintaining (PM) fibre Bragg grating's physical parameters was proposed by Caucheteur *et al.* [83] In this thesis, two different methods will be adopted to measure the maximum PDLs and the corresponding wavelengths of a single mode FBG. The Bragg wavelengths of two orthogonal axes and their difference of a PM FBG will also be investigated. The temperature sensing applications based on the polarization properties of the single mode FBG and PM FBG are realized.

A large number of FBG sensors may be integrated at different locations along a single optical fibre or several fibres to form a quasi-distributed sensor [84-86]. The advantage of this FBG array is that each FBG has a unique Bragg wavelength and can be individually interrogated. Such an FBG array can be fabricated with an arbitrary linear distance between the gratings, while the wavelength separation between adjacent Bragg wavelengths is determined only by the wavelength shift of higher and lower wavelengths.

Many papers have reported the field applications of FBG sensors. Fibre Bragg grating sensors offer a number of advantages for spacecraft applications in embedded sensors that monitor the performance and fabrication of reinforced carbon fibre composites and advanced testing of gas turbine engines [87]. There are numerous applications of FBG sensors for structural health monitoring (SHM) in civil engineering, including monitoring of bridges [88], crack detection [89], and power transmission lines [90]. The FBG sensors can also be used in harsh environments [91].

Based on the instinctive temperature and strain sensitivity of FBGs and their unique advantages, FBGs have become more and more important in the sensing fields.

Chapter 2

Temperature, Humidity, Saccharinity and Salinity Sensitivity

2.1 Introduction

This chapter will discuss sensing applications in temperature, humidity, saccharinity and salinity of different polymer-coated FBGs. It will be shown that the temperature changes in different environmental conditions will result in a linear shift of the Bragg resonant wavelength of the FBGs. A polyimide-coated FBG is sensitive to relative humidity due to the unique properties of polyimide polymer. Meanwhile, an acrylate-coated FBG shows insensitivity to relative humidity. A new scheme for simultaneous measurement of temperature and saccharinity/salinity based on polymer-coated FBGs is proposed. It is

demonstrated that a polyimide-coated FBG can be used to measure the saccharinity/salinity while an acrylate-coated FBG can measure the environmental temperature change simultaneously.

Section 2-2 presents temperature sensitivities of FBGs in different environmental conditions. In Section 2-3, the humidity sensitivities of acrylate-coated and polyimide-coated FBGs are investigated. The saccharinity and salinity sensitivities of acrylate-coated and polyimide-coated FBGs are presented in Sections 2-4 and 2-5.

2.2 Temperature Sensitivity

2.2.1 Theory of Fibre Bragg Grating Temperature Sensitivity

The Bragg grating resonance, which is the centre wavelength of light back reflected from a Bragg grating, depends on the effective index of refraction of the core and the periodicity of the grating. The effective index of refraction, as well as the periodic spacing between the grating planes, will be affected by changes in temperature and strain. Using equation $\lambda_B = 2n_{eff}\Lambda$, the shift in the Bragg grating wavelength $\Delta\lambda_B$ due to temperature and strain changes is given by [64, 92]

$$\Delta\lambda_B = 2\left(\Lambda\frac{\partial n}{\partial l} + n\frac{\partial \Lambda}{\partial l}\right)\Delta T + 2\left(\Lambda\frac{\partial n}{\partial l} + n\frac{\partial \Lambda}{\partial l}\right)\Delta l \qquad (2\text{-}1)$$

The first term in Eqn. (2-1) represents the temperature effect on an optical fibre. The changes in the grating spacing and the index of refraction caused by thermal expansion

result in a shift in the Bragg wavelength. This fractional wavelength shift for a temperature change ΔT may be written as [64]

$$\Delta\lambda_B = \lambda_B(\alpha+\zeta)\Delta T \tag{2-2}$$

where $\alpha = \left(1/\Lambda\right)\left(\partial\Lambda/\partial T\right)$ is the thermal expansion coefficient for the fibre (approximately, 0.55×10^{-6} °C^{-1} for silica). The quantity $\zeta = \left(1/n\right)\left(\partial n/\partial T\right)$ represents the thermo-optic coefficient and it approximately equals 8.6×10^{-6} °C^{-1} for a germanium doped silica-core fibre. Clearly, the index change is by far the dominant effect. From Eqn. (2-2), the expected sensitivity at a 1550 nm Bragg grating is approximately 0.0137 nm/°C.

2.2.2 Experimental Details

A standard telecommunication optical fibre (SMF-28, Corning Inc.) was stored in a high hydrogen pressure environment (1900 psi) at room temperature for two weeks. Afterwards, the fibre was stored in a freezer at -70 °C before use. This process can prevent the hydrogen from diffusing out of the optical fibre. Hydrogen loading of a fibre satisfactorily enhanced its photosensitivity. A phase mask of 10 mm in length was used to write 1 cm FBG gratings onto the fibre with the laser irradiation from an ArF excimer laser (193 nm). The transmission spectrum of the FBG was monitored *in-situ* during the laser exposure with a white light source and an optical spectrum analyzer. Since the photosensitivity of optical fibres also resulted in further changes to the central Bragg

wavelength and the peak loss of the attenuation bands generated after fabrication when the hydrogen diffused out of the fibre, the FBG was baked at 150 °C overnight to eliminate the residual hydrogen and to stabilize the UV-induced index changes. The experimental setup for inscribing gratings is shown in Fig. 2-1.

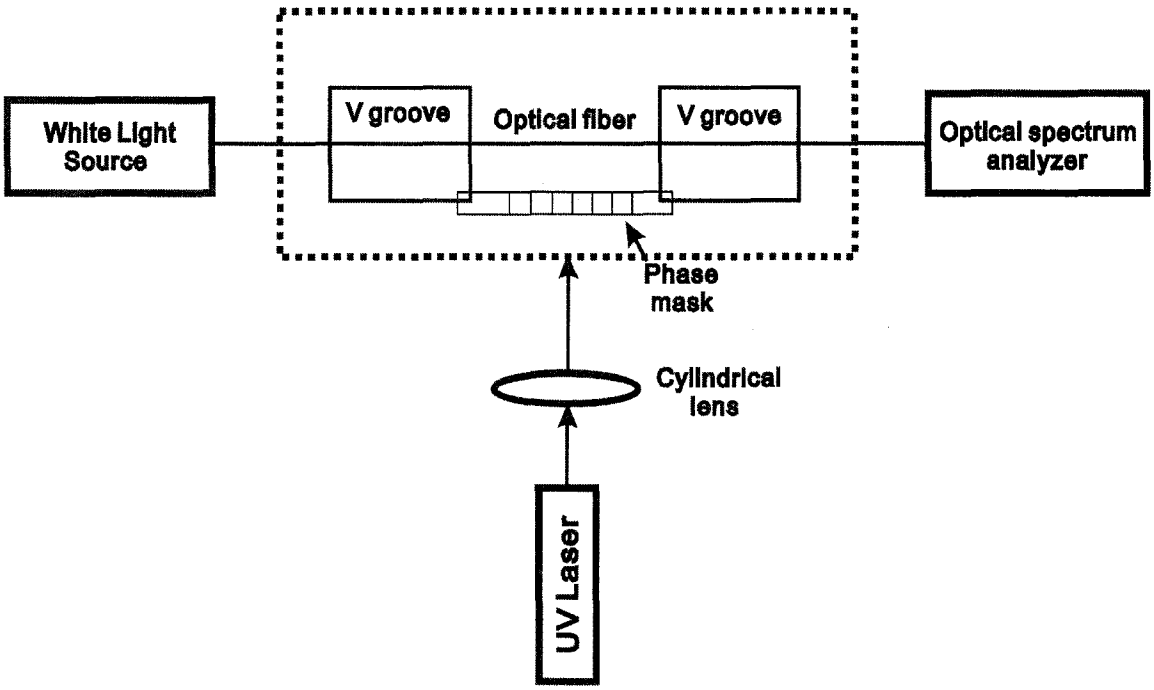

Figure 2-1: Schematic diagram of the fabrication of a fibre Bragg grating.

The transmission spectrum of a typical FBG is shown in Fig. 2-2. A broadband lightwave travels through the optical fibre and enters into the FBG, from which one specific wavelength is reflected back by the FBG. Full width at half maximum (FWHM) is a parameter to characterize the bandwidths of laser beams or optical devices. For a strong FBG, it is normally 3 dBm from the reflectivity peak.

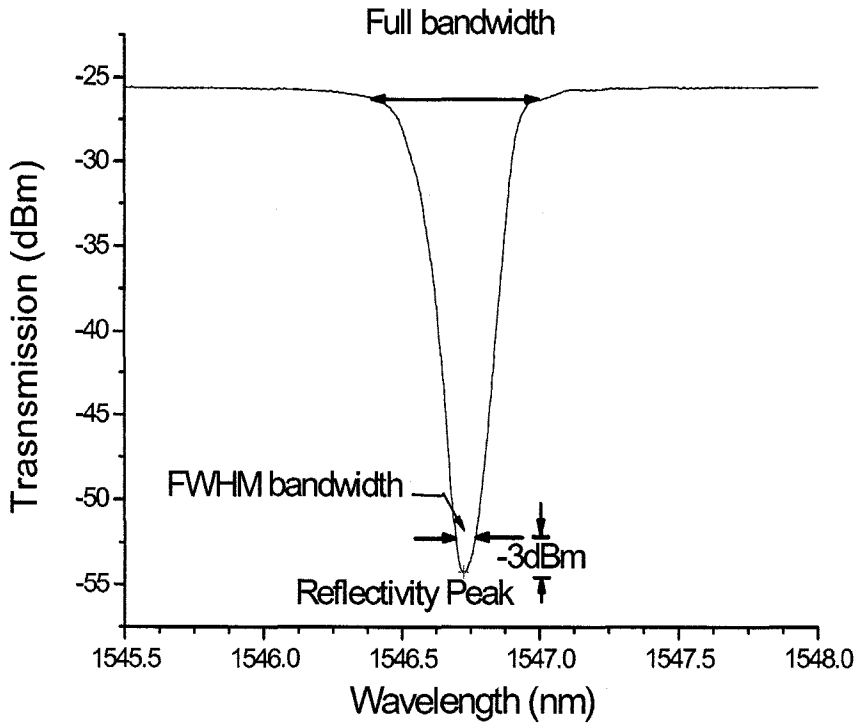

Figure 2-2: Transmission spectrum of a FBG at room temperature.

Figure 2-3 illustrates the setup used to determine the temperature-induced shift in the resonance band of the FBG transmission spectrum. Light from a broadband light source (EBS-7210, MPB Communication, Inc.) was launched into one end of the fibre containing the grating and the transmission spectrum was recorded by an optical spectrum analyzer (ANDO AQ-6315E, Yokogawa Co.). The emission spectrum of the Er^{3+} broadband source is shown in Fig. 2-4, which indicates an output in the wavelength range of 1525-1600 nm. The resolution of the OSA was set at 0.05 nm in the measurement process due to the narrow FWHM bandwidth of the FBG. The temperature of the grating region on the sample was controlled by employing a

microprocessor-controlled water bath (Precision 281). The FBG sample was immersed in the water bath where the temperature was kept constant for half an hour before measurement in order to ensure that the transmission spectrum of the FBG sample was immovable and the system was in a stable condition.

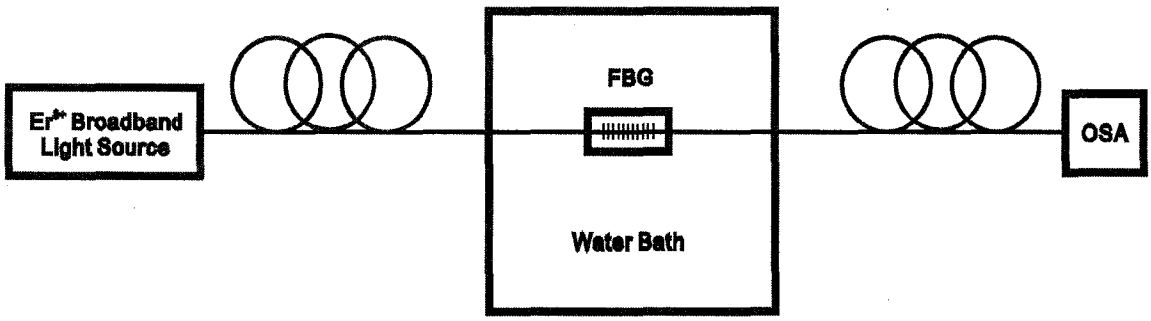

Figure 2-3: Schematic diagram of a temperature sensing measurement system.

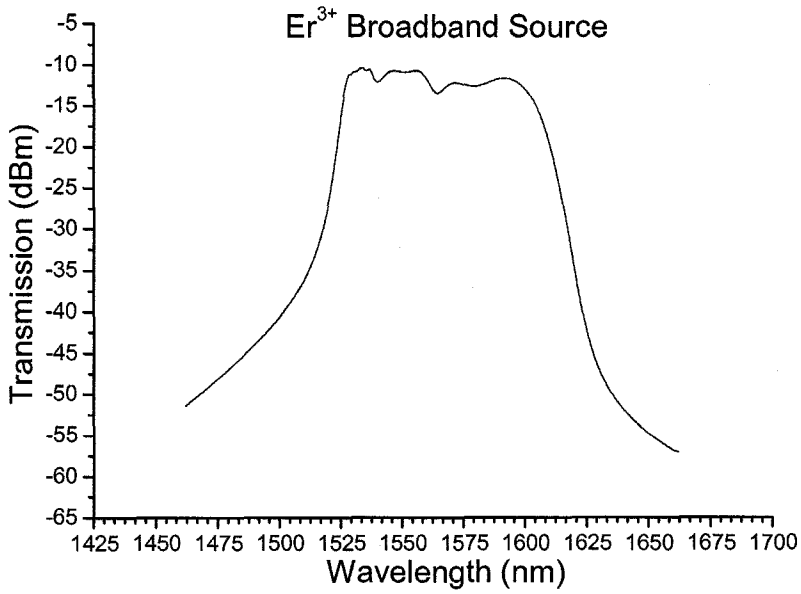

Figure 2-4: Emission spectrum of the Er^{3+} broadband light source used in this study.

2.2.3 Temperature Sensing Response of a Strong Fibre Bragg Grating

For the strong FBG used here, the grating area was not recoated with a polymer layer after grating inscription. After the water temperature in the water bath was first changed from 5 °C to 90 °C with a step of 5 °C, the temperature was then decreased from 90 °C to 35 °C with a step of 5 °C. At each specific temperature, sufficient time for stabilization has been guaranteed to ensure that the thermal equilibrium has reached between the FBG sample and the water reservoir before recording the data. At a temperature of 25 °C, the transmission spectrum is shown in Fig. 2-5.

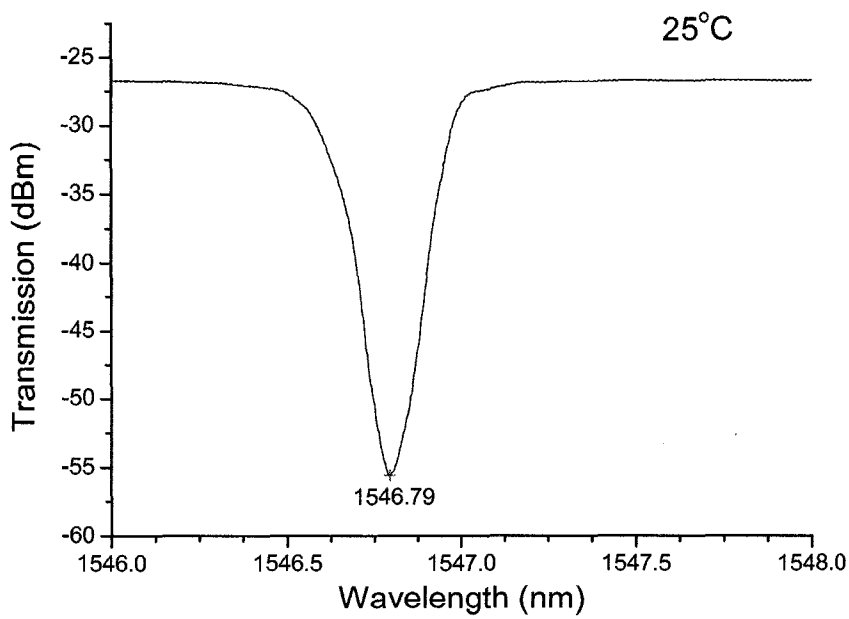

Figure 2-5: Transmission spectrum of a strong FBG at 25 °C.

For the heating process, the observed transmission spectra and the change of Bragg grating wavelength as a function of increasing temperature are shown in Figs. 2-6 and 2-7, respectively. The wavelength red-shift of the FBG resonant peaks with respect to the increasing temperature was measured to be 0.0091 nm/°C.

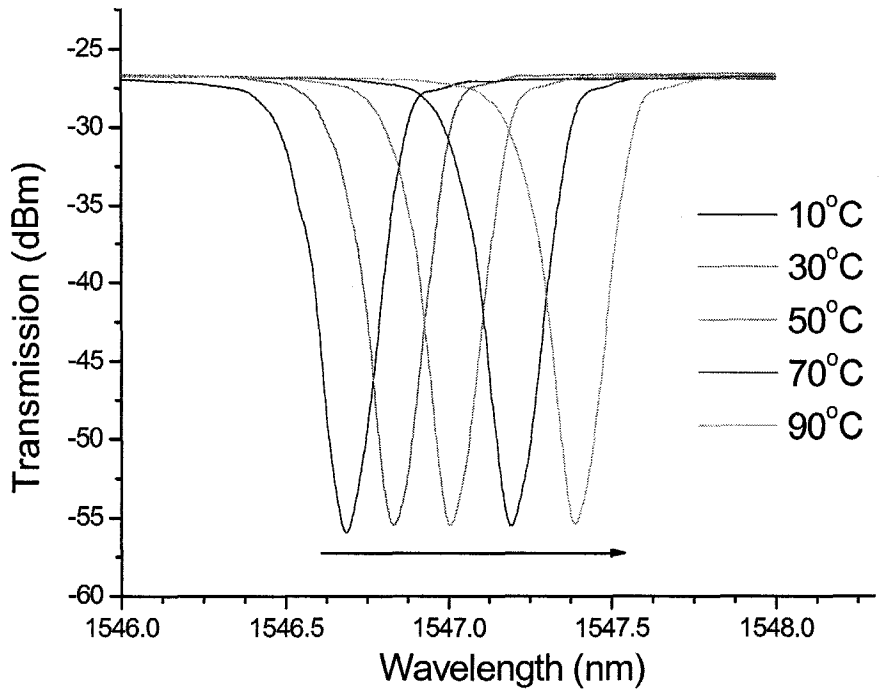

Figure 2-6: Transmission spectra of the FBG as a function of increasing temperature.

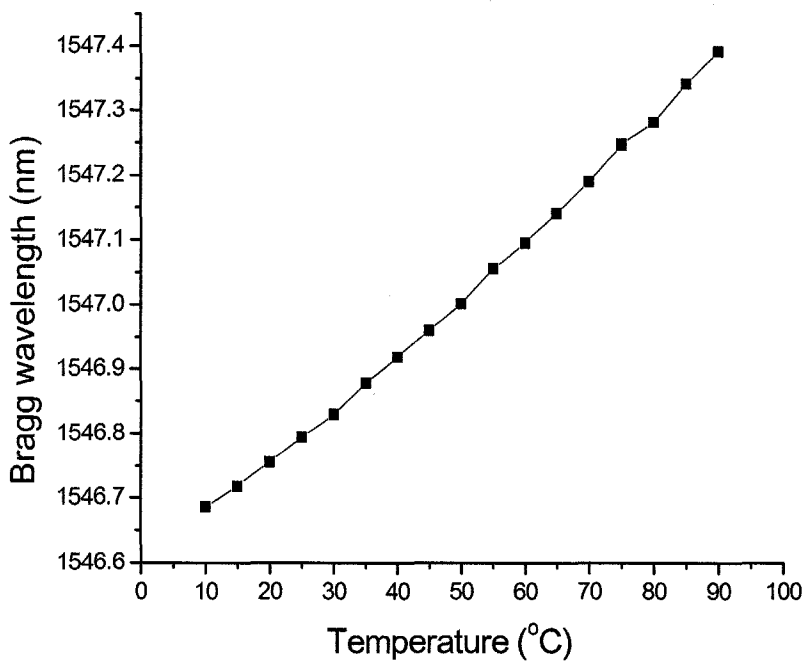

Figure 2-7: Bragg wavelength of the FBG as a function of increasing temperature.

For the cooling process, the measured change of Bragg grating wavelength as a function of decreasing temperature is shown in Fig. 2-8. The shift in the Bragg wavelength with respect to the decreasing temperature was measured to be 0.0098 nm/°C. The experimental results of a Bragg centre wavelength shift as a function of temperature are close to the expected value of 0.0137 nm/°C for a FBG recoated with an acrylate coating. The difference of the temperature sensitivity between the experimental result and theoretical value is mainly due to a discrepancy between different coating materials induced thermal expansion coefficient of the cladding materials and the thermooptic coefficient of different core materials. Results obtained from the heating and cooling processes demonstrated high repeatability of the temperature sensing measurement.

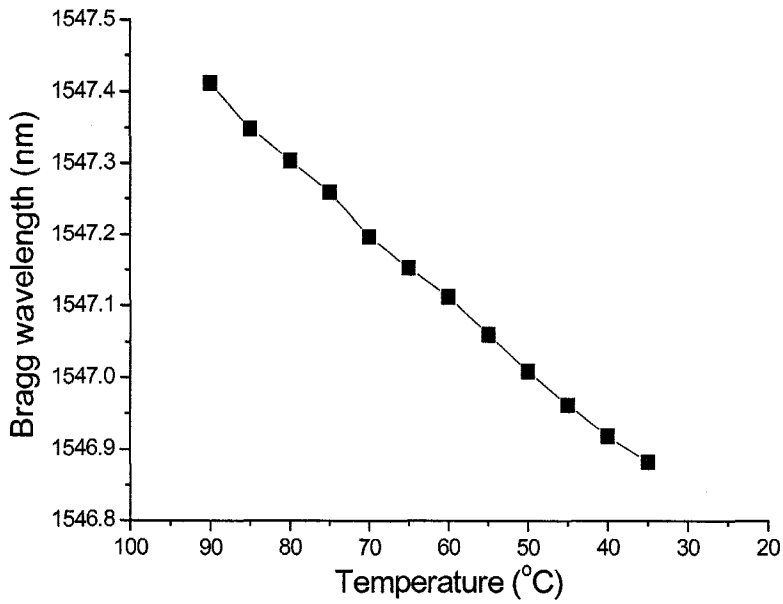

Figure 2-8: Bragg wavelength of the FBG as a function of decreasing temperature.

A general expression for the approximate FWHM bandwidth of a grating is given by [92]

$$\Delta\lambda = \lambda_B s \sqrt{\left(\frac{\Delta n}{2n_0}\right)^2 + \left(\frac{1}{N}\right)^2} \tag{2-3}$$

where N is the number of the grating planes. The parameter s is ~1 for strong gratings (for grating with near 100% reflection) whereas s ~0.5 for weak gratings. The FWHM bandwidth of the FBG loss peak in the heating process is shown in Fig. 2-9 which indicates that the FWHM bandwidth doesn't exhibit a dependence on the changing temperature.

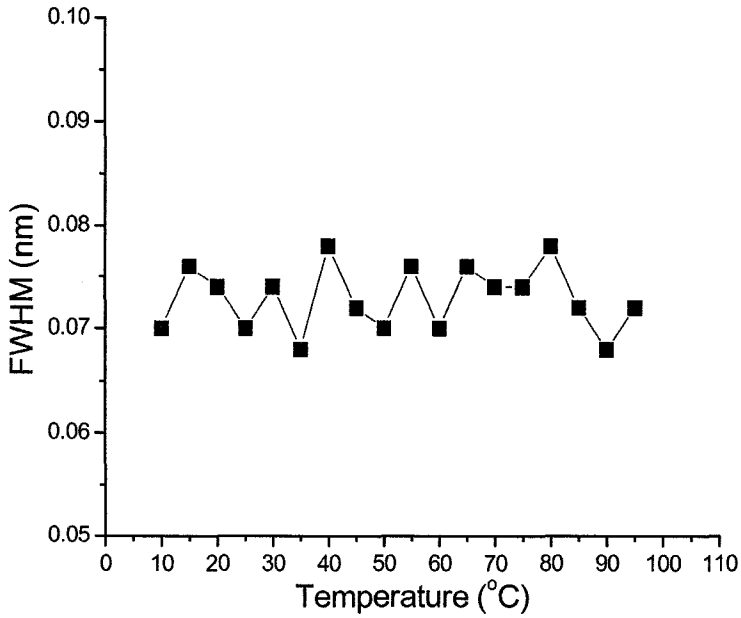

Figure 2-9: Change in the FWHM bandwidth of the FBG during heating process.

2.2.4 Temperature Sensing Response of a Weak Fibre Bragg Grating

Compared with a strong FBG or a FBG with a high reflection, a weak FBG has relatively weak reflection power (contrast index $\Delta n \sim 2-4\times10^{-5}$). A broadband light source with output in the S-band (ASE-FL7200, Thorlabs) was used as the light source in the experimental setup shown in Fig. 2-3. Figure 2-10 shows the emission spectrum of the ASE light source, which gives the output in the wavelength range of 1410-1510 nm with a quick decrease in the output power on both sides away from the peak wavelength. The

transmission spectrum of the weak FBG is shown in Fig. 2-11. The Bragg reflection peak is on the declining section of the output spectrum of the light source which makes it less straightforward to find out the transmission power at the peak.

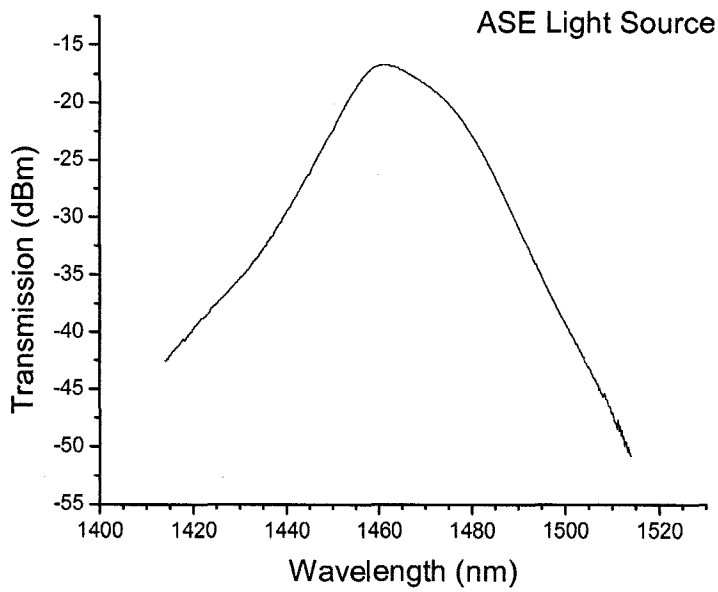

Figure 2-10: Emission spectrum of the ASE light source used in this study.

In order to overcome the light source limitation, two different methods were adopted. First, a data processing algorithm on FBG transmission spectra was adopted, in which three widths were defined, i.e. FWHM (50%), the width at 25% and the width at 75% height that is from reflection peak to full width. It is reasonable to consider the mean value of the three midpoint wavelengths as the peak wavelength. Through this algorithm, a linear relation between Bragg wavelength and changing temperature is obtained (Fig. 2-12).

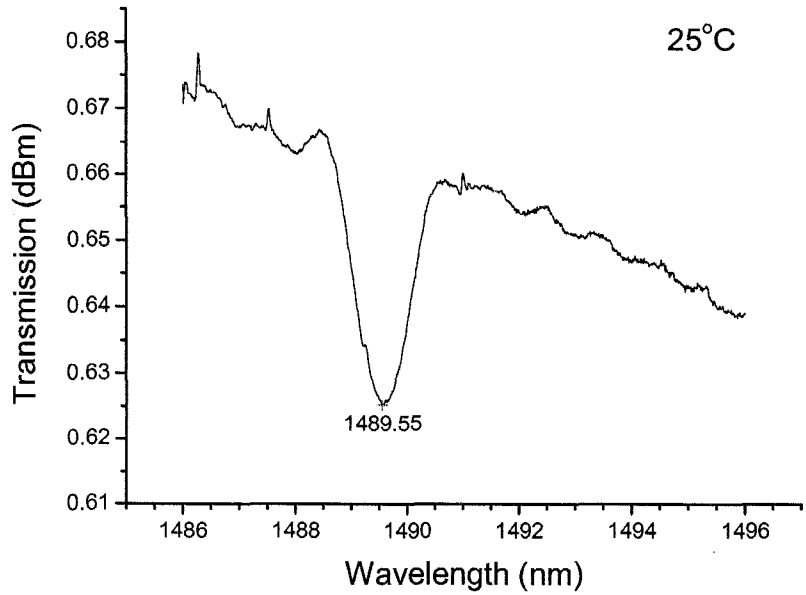

Figure 2-11: Transmission spectrum of the weak FBG obtained by the OSA at 25 °C.

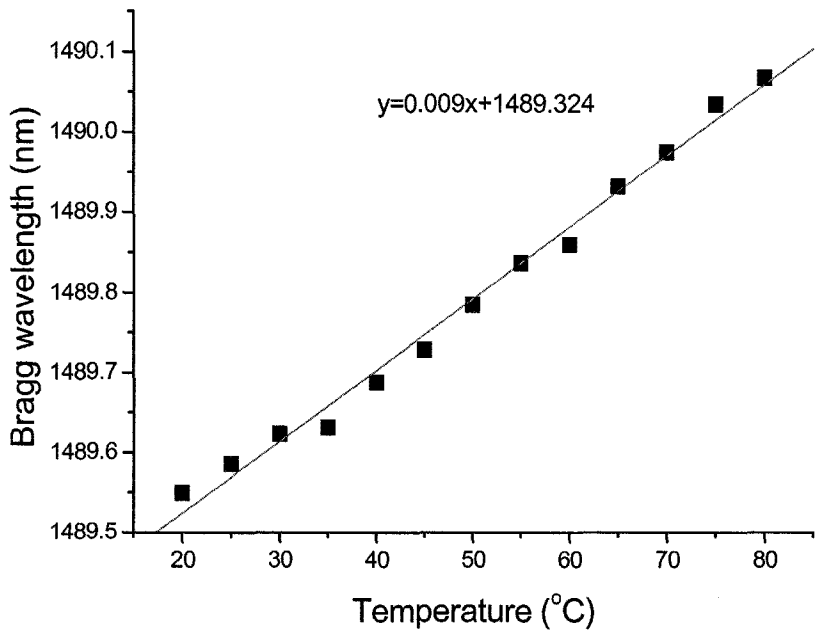

Figure 2-12: Bragg wavelength of the weak FBG obtained through the data processing algorithm.

Secondly, a wavelength scanning method was adopted to pick up the Bragg wavelength directly. The schematic diagram of the wavelength scanning method is shown in Fig. 2-13. In the experimental setup illustrated in Fig. 2-3, a tunable laser (TUNICS-PR, Photonetics) was used instead of a broadband light source. The Bragg wavelength falls in the output wavelength range of the tunable laser. An optical power meter (Newport 2832-C) recorded transmitted powers with a personal computer through LabVIEW control software. Front panels of the LabVIEW driver program for the tunable laser diode and the power meter are shown in Figs. 2-14 and 2-15. The transmission spectrum obtained from the wavelength scanning method is shown in Fig. 2-16.

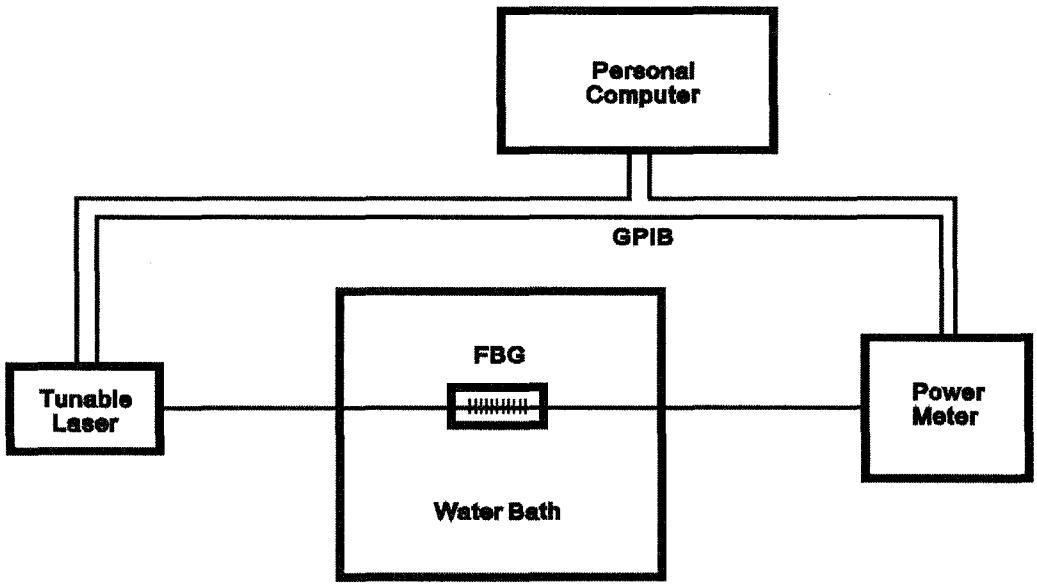

Figure 2-13: Schematic diagram of the wavelength scanning method.

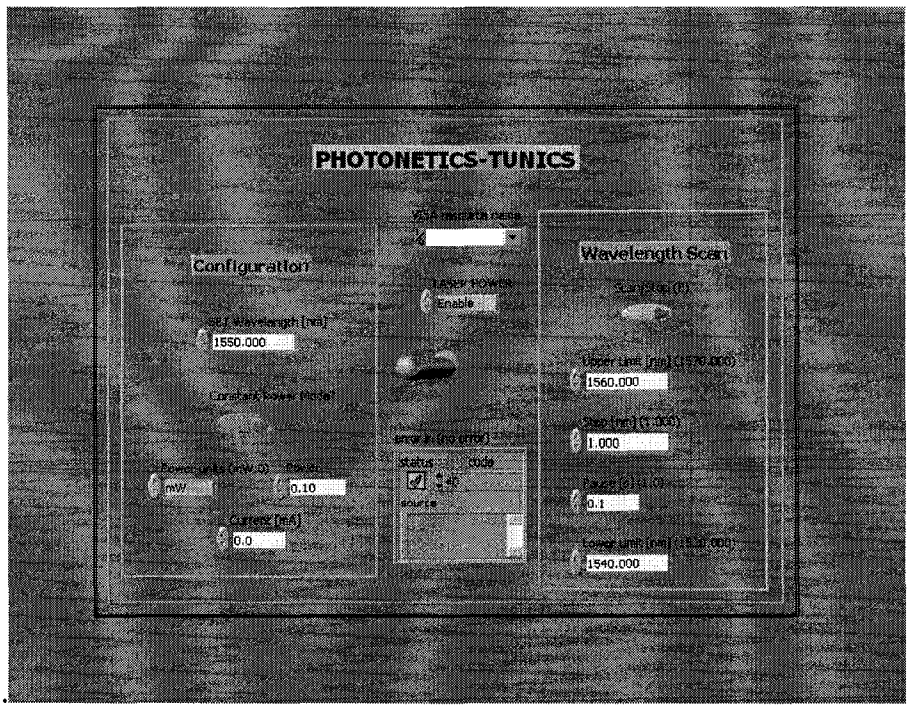

Figure 2-14: Front panel of the LabVIEW driver program for the tunable laser.

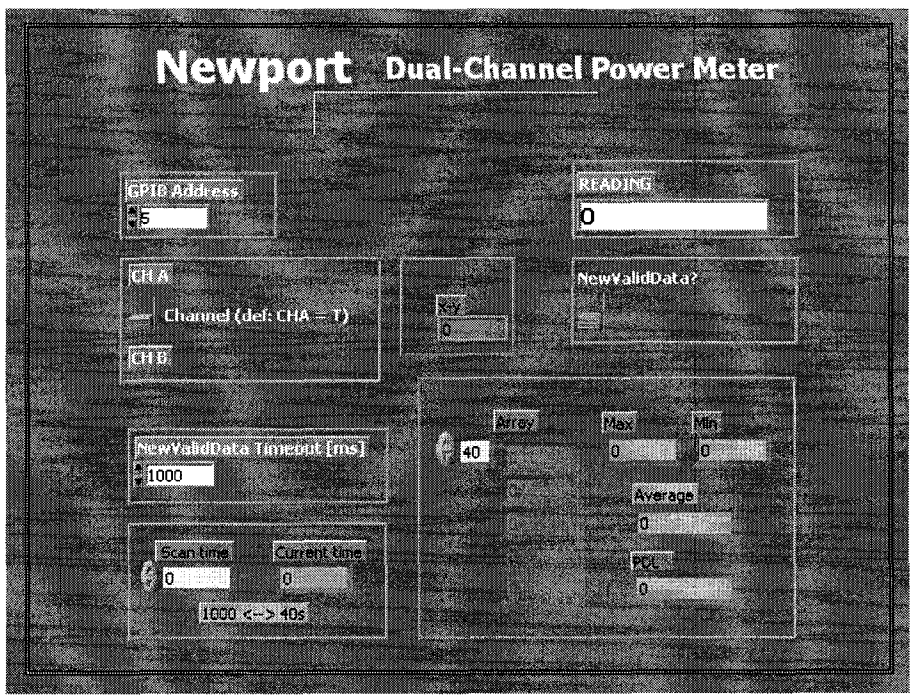

Figure 2-15: Front panel of the LabVIEW driver program for the power meter.

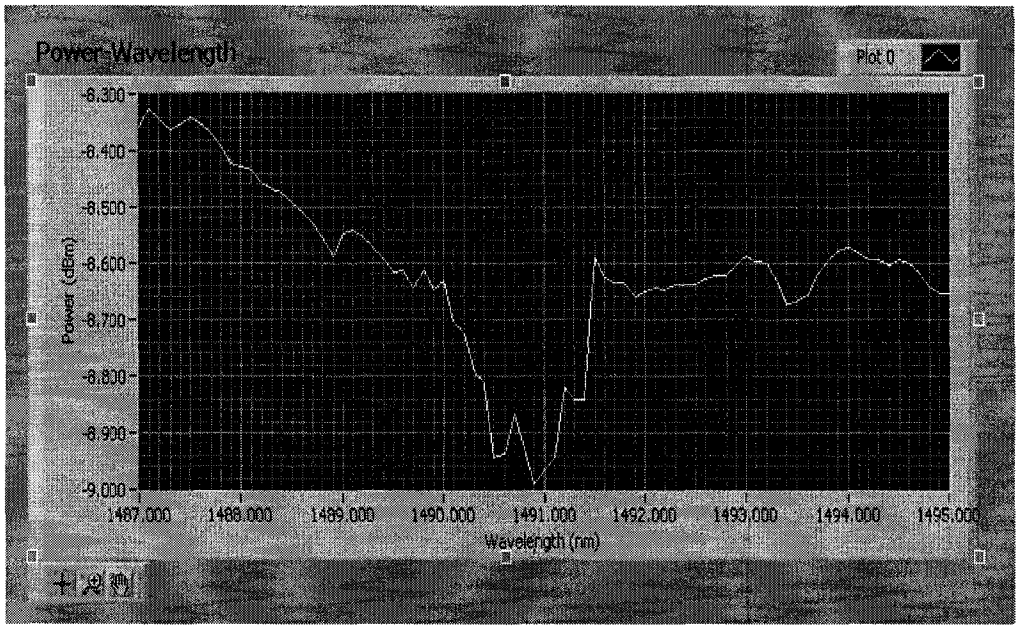

Figure 2-16: Transmission spectrum of the weak FBG
obtained from the wavelength scanning method.

Through this method, a linear relation between Bragg wavelength and changing temperature is obtained (Fig. 2-17). From the data processing algorithm, the temperature sensitivity was found to be 0.0087 nm/°C. For comparison, the temperature sensitivity from the wavelength scanning method gave 0.0094 nm/°C. A good agreement between these two methods is obtained. Also, the temperature sensitivities obtained from both the strong and weak FBGs indicated excellent agreement.

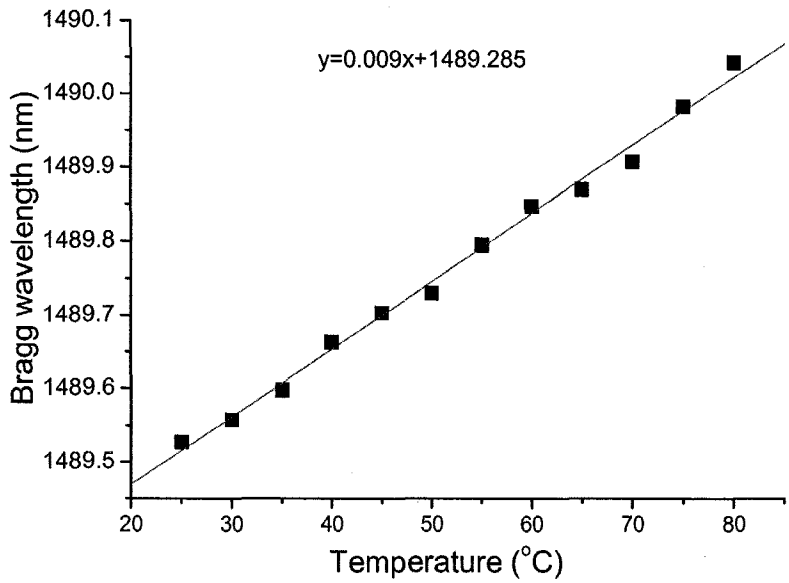

Figure 2-17: Bragg wavelength of the weak FBG obtained from the wavelength scanning method.

2.3 Humidity Sensitivity

2.3.1 Temperature and Humidity Sensitivity of Polyimide-coated Bragg Gratings

Numerous applications such as chemical processing, air conditioning, agriculture, food storage, and civil engineering require humidity sensing. In this section a relative humidity (RH) fibre sensor that uses a polyimide-coated FBG will be discussed in details. Meanwhile, an acrylate-coated FBG will be demonstrated to be insensitive of relative humidity.

Using equation $\lambda_B = 2n_{eff}\Lambda$, the shift in the Bragg wavelength due to thermal expansion changes in the grating spacing and changes in the index of refraction is given by [65]

$$\frac{\Delta\lambda_B}{\lambda_B} = S_{RH}\Delta RH + S_T\Delta T = \left[\beta_{cf} - \hat{P}_e\left(\beta_{cf} - \beta_f\right)\right]\Delta RH + \left[\alpha_{cf} - \hat{P}_e\left(\alpha_{cf} - \alpha_f\right) + \zeta\right]\Delta T \quad (2\text{-}4)$$

where S_{RH} and S_T are the sensor sensitivities to relative humidity and temperature, respectively. ΔRH and ΔT are the changes in relative humidity and temperature accordingly. β_i is the hygroscopic longitudinal expansion coefficient, which is zero for bare fibre, and α_i is the thermal longitudinal expansion coefficient. The subscript stands for bare fibre ($i = f$) and coated fibre ($i = cf$). ζ is the thermo-optic coefficient of the fibre core, and $\hat{P}_e$ is the effective photoelastic coefficient of the coated fibre [65]

$$\hat{P}_e = \frac{n^2}{2}\left[P_{12} - \upsilon\left(P_{11}+P_{12}\right)\right] = 0.213 \quad (2\text{-}5)$$

where P_{11} and P_{12} are the components of the strain-optic tensor, n is the index of refraction of the core, and υ is the Poisson's ratio. For a typical optical fibre P_{11} = 0.113, $P_{12} = 0.252$, $n = 1.482$, $\upsilon = 0.16$, and $\upsilon = -\frac{\varepsilon_{f,r}}{\varepsilon_{f,z}}$ where $\varepsilon_{f,r}$ and $\varepsilon_{f,z}$ are the radial and axial elastic fibre strains, respectively.

The sensor temperature sensitivity S_T can be expressed as

$$S_T = \alpha_{cf} - \hat{P}_e\left(\alpha_{cf} - \alpha_f\right) + \zeta \quad (2\text{-}6)$$

Table 2-1 lists some thermo-optic parameters of the fused silica fibre and the polyimide coating. According to the table, the temperature sensitivity of the sensor can be

calculated to be $S_T = 7.010\times10^{-6}$ $^{o}C^{-1}$. The temperature coefficient K_T, defined as $K_T = \Delta\lambda_B / \Delta T$, is $K_T = 0.0109$ nm/°C at 1550 nm.

Table 2-1. Properties of the fused silica fibre and the polyimide coating.

Parameter	Value	Reference
Thermal expansion coefficient α_f	5×10^{-7}	[93]
Thermal expansion coefficient α_c	4×10^{-5}	[94]
Thermo-optic coefficient ξ	$(55\pm4.8)\times10^{-7}$	[95]
Young's modulus, E (Fibre)	72	[96]
Young's modulus, E (coating)	2.45	[94]
Poisson's ratio, ν (fibre)	0.17	[93]
Poisson's ratio, ν (coating)	0.41	[94]
Hygroscopic expansion coefficient β_f	7×10^{-5}	[65]
Hygroscopic expansion coefficient β_c	10	[97]
Longitudinal expansion coefficient of coated fibre α_{cf}	1.39	[65]
Longitudinal expansion coefficient of coated fibre β_{cf}	1.58	[65]

As we know that the hygroscopic longitudinal expansion coefficient of the bare fibre β_f is zero, the sensor relative humidity sensitivity S_{RH} can be expressed as:

$$S_{RH} = \left(1 - \hat{P}_e\right)\beta_{cf}. \tag{2-7}$$

Following the parameters in Table 2-1, the relative humidity sensitivity S_{RH} is 1.676×10^{-6} %RH^{-1}. The humidity coefficient K_{RH}, defined as $K_{RH} = \Delta\lambda_B / \Delta RH$, is 2.6×10^{-3} nm/%RH at 1550 nm.

2.3.2 Experimental Details

Once the FBG is inscribed onto the SMF-28 fibre, either acrylate or polyimide can be re-coated on the grating section using a fibre recoater to protect the grating. The experimental setup used to characterize the humidity response of the sensor is shown in Fig. 2-18. The broadband light source was connected to the FBG sensor using a 2×2 fibre coupler. The reflected signal from the sensor was monitored using the optical spectrum analyzer. The polyimide-coated FBG sensor was stored inside an environmental chamber with controllable relative humidity. All experiments performed in this work were carried out at a room temperature of 20 °C. Sufficient time was given to allow the test environment to stabilize before readings of the wavelength from the optical spectrum analyzer were recorded.

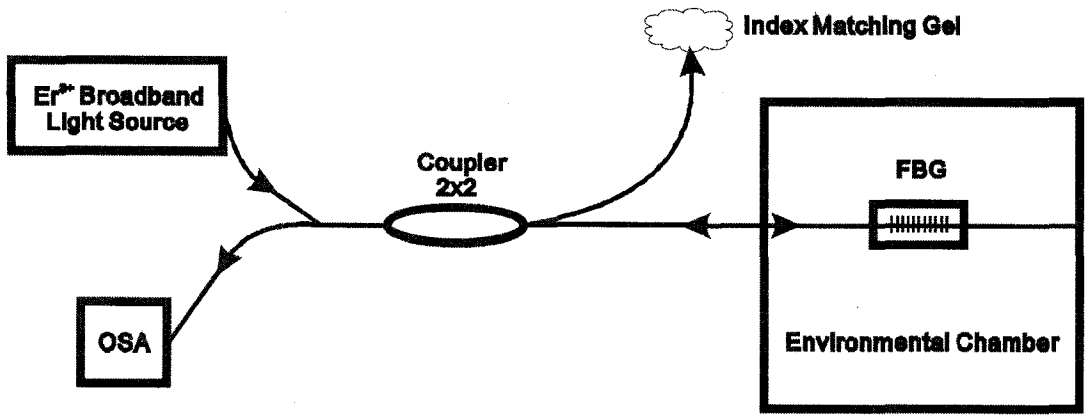

Figure 2-18: Schematic diagram of the humidity measurement system.

2.3.3 Humidity Sensing Response of a Polyimide-coated Fibre Bragg Grating

The polyimide-coated FBG was placed in the environmental chamber where the temperature was kept at 20 °C. At each fixed humidity setting, the output signal from the OSA was allowed to settle for 1 hour before a reading was taken, and this process was carried out three times to ensure reproducibility. The results obtained from a series of tests of the sensor system are shown in Fig. 2-19. The data shows the behavior of the FBG spectral characteristics when the sensor system was exposed to different humidity conditions. From the diagram, the Bragg wavelength shift was observed when the humidity in the test environment was varied from 13 %RH to 91 %RH. As the humidity level increased, the wavelength was found to shift toward the longer wavelength, which is consistent with the elongation of the FBG caused by the expansion of the polymer coating. This humidity change resulted in a wavelength shift of 0.22 nm.

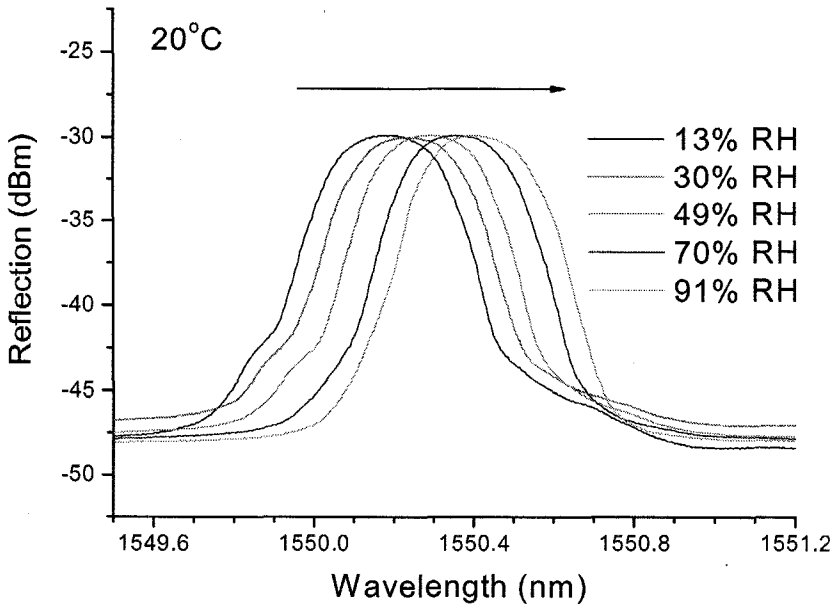

Figure 2-19: Reflection spectra of the polyimide-coated FBG at different relative humidities at 20 °C.

Figure 2-20 shows the shifts of the Bragg wavelength against the relative humidity during three repeated tests. A linear regression was performed to establish the relationship between the wavelength shift due to the material expansion and the humidity level in the test enclosure. The line fitted to the data points reveals a linear relationship between the two parameters and this agrees well with the observations made by Kronenberg *et al.* [65] and Sager *et al.* [97], where the volume expansion of the polyimide film varies linearly with humidity. The humidity sensitivities of the FBG were estimated to be 2.85, 2.62, and 2.60 pm/%RH respectively at 1550 nm. The discrepancy among these test results may be ascribed to the incomplete adhesion between the silica surface and the polyimide layer due to the weak physical bonding at the interface between the fibre and the coating.

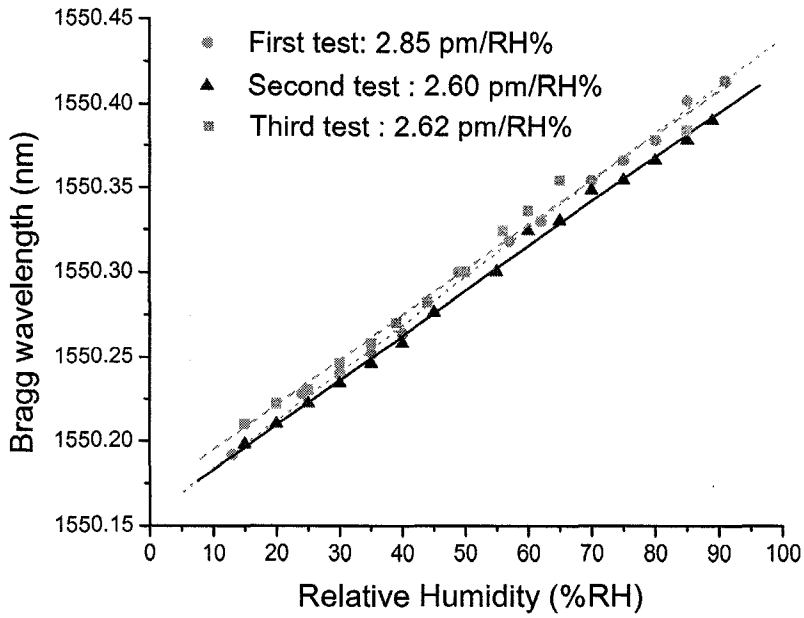

Figure 2-20: Bragg wavelength of the polyimide-coated FBG wavelength as a function of relative humidity in the environmental chamber.

Bare silica fibres are not sensitive to humidity. Polyimide polymers, however, are hygroscopic and will swell in aqueous media as the water molecules migrate into them. The swelling of the polyimide coating strains the fibre, which modifies the Bragg condition of the FBG and thus serves as the basis of the proposed sensor.

2.3.4 Humidity Sensing Response of an Acrylate-coated Fibre Bragg Grating

Following the same procedures mentioned above, FBG wavelengths of an acrylate-coated FBG as a function of increasing and decreasing relative humidity were measured and are shown in Figs. 2-21 and 2-22, respectively. The results in these two figures clearly indicate that the change of relative humidity will not change the centre wavelength of FBG at room temperature. Thus the acrylate-coated FBG is not sensitive to the change in relative humidity.

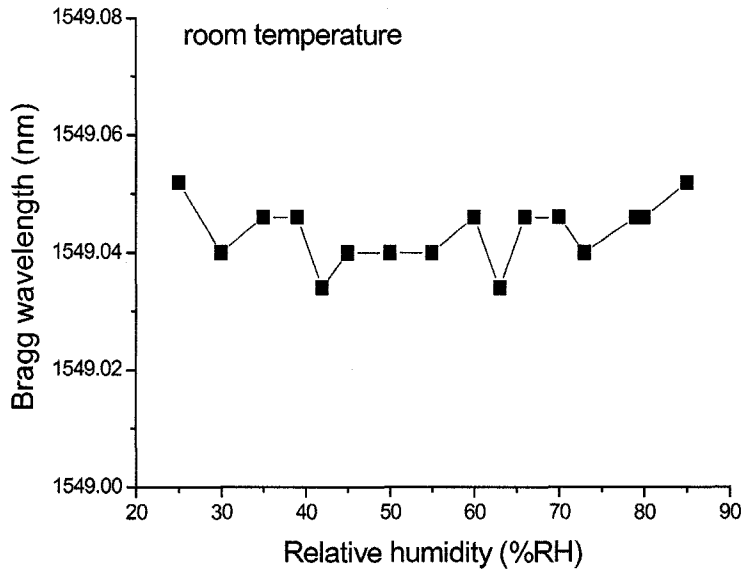

Figure 2-21: Bragg wavelength of the acrylate-coated FBG wavelength as a function of increasing relative humidity.

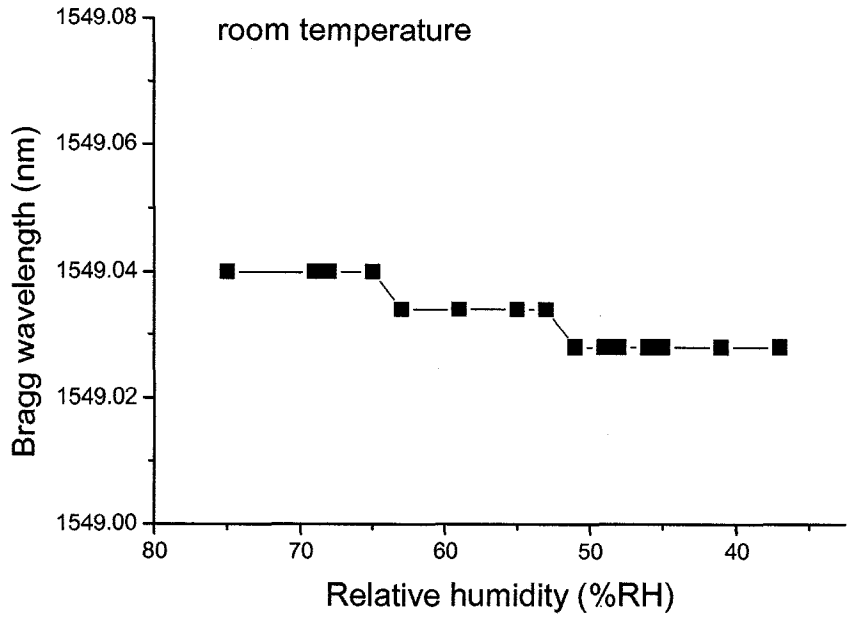

Figure 2-22: Bragg wavelength of the acrylate-coated FBG wavelength as a function of decreasing relative humidity.

2.4 Saccharinity Sensitivity

2.4.1 Principles of Fibre Bragg Grating Saccharinity Sensitivity

In-situ monitoring of physical, chemical, and biological parameters is of great importance for biomedical applications and food industries. Among different parameters, saccharinity and temperature, especially simultaneous measurement of these two parameters, are especially important for disease prevention and therapy in health care and

food production.

This section reports a new scheme constructed with two different polymer-coated FBGs for simultaneous measurement of temperature and saccharinity. Polyimide and acrylate polymers are fibre coating materials, which have excellent strength and can resist breakage. These materials are harmless and will not do any damage to human beings and the environment. Particularly, polyimide polymers are hygroscopic and swell in aqueous media as the water molecules migrate into them [65]. In order to achieve *in-situ* measurement of these two parameters, our sensor system has been designed as a multiplexed system with one acrylate-coated FBG and one polyimide-coated FBG, in which the acrylate-coated FBG is not sensitive to saccharinity and can function as a temperature sensor, only the polyimide-coated FBG can measure saccharinity in sugar solution.

The water accumulation and leakage in the coating material of the FBG is a diffusion process, which can be described by Fick's second law [98]

$$\frac{\partial c}{\partial t} = D\nabla^2 c \tag{2-8}$$

where c is the water concentration, D is the constant diffusion coefficient, and t is the diffusion time.

For radial diffusion in a cylinder as illustrated in Fig. 2-23, the general diffusion equation of Eqn. (2-8) can be expressed in cylindrical coordinates

$$\frac{\partial c}{\partial t} = D\frac{1}{r}\frac{\partial}{\partial r}\left(r\frac{\partial c}{\partial r}\right). \tag{2-9}$$

The boundary condition for the diffusion mass entering the polyimide coating at the

position r along the direction of diffusion at time t is

$$c(a<r<b,t=0)=C_0$$

$$c(r=b,t\geq 0)=C_{ext} \tag{2-10}$$

$$\frac{\partial c}{\partial r}(r=a,t\geq 0)=0.$$

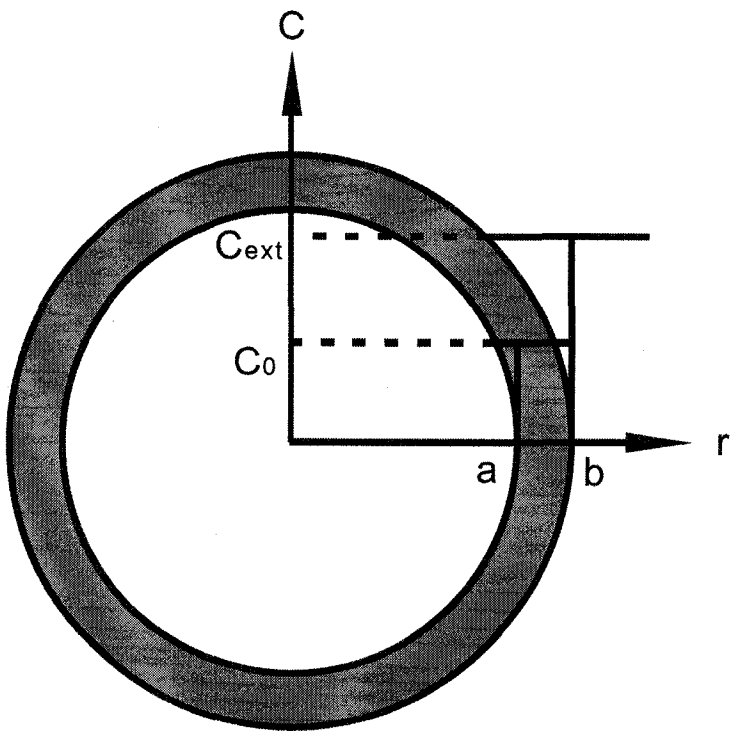

Figure 2-23: Water concentration levels in the fibre layer.

When the FBG is immersed in the water bath, it is reasonable to consider the environmental medium as a constant concentration source, in which the water outside the fibre will diffuse into the fibre coating until it reaches equilibrium. The solution of Eqn. (2-9) is

$$c(r,t) = C_{ext} erfc(\frac{r}{\sqrt{4Dt}}). \quad (2\text{-}11)$$

In the case when sugar is gradually added into the water bath, the water concentration in the fibre coating will be higher than that in the environmental medium and the water will diffuse into the environmental medium from the fibre coating until it reach equilibrium. The solution of Eqn. (2-9) is then

$$c(r,t) = C_{ext} erf\left(\frac{r}{\sqrt{4Dt}}\right). \quad (2\text{-}12)$$

2.4.2 Polymer-coated Fibre Bragg Grating Temperature and Saccharinity Sensor

For a multiplexed FBG system, two FBGs with a grating length of 1 cm for each were inscribed on a hydrogen-loaded fibre. After the grating fabrication, one section of the grating area was then recoated with polyimide polymer while the other grating area recoated with acrylate polymer. The multiplex FBG sensor system is illustrated in Fig. 2-24. The recoating process resulted in the fibre diameter of 173 μm at the grating section. The transmission spectrum of the sensor was measured by the optical spectrum analyzer. Figure 2-25 shows two Bragg wavelengths at 1549.02 and 1550.24 nm with reflection signals of 9.24 and 13.47 dB, respectively. The characteristics of the multiplexed FBG sensor are listed in Table 2-2.

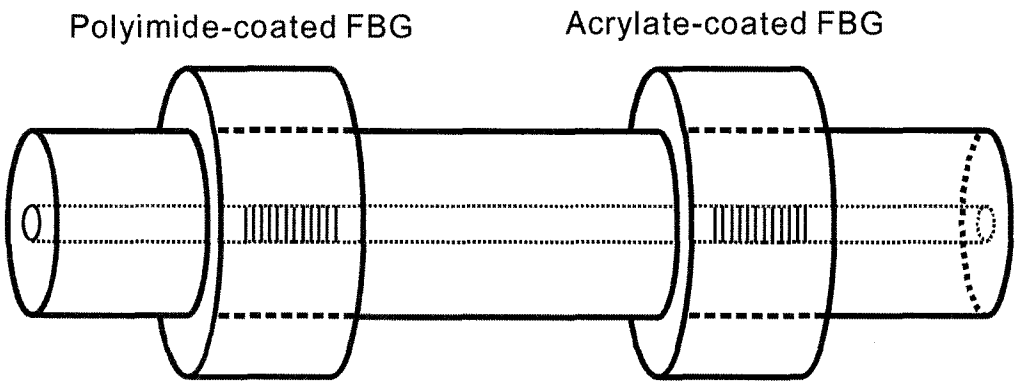

Figure 2-24: Schematic illustration of a multiplexed FBG saccharinity sensor system.

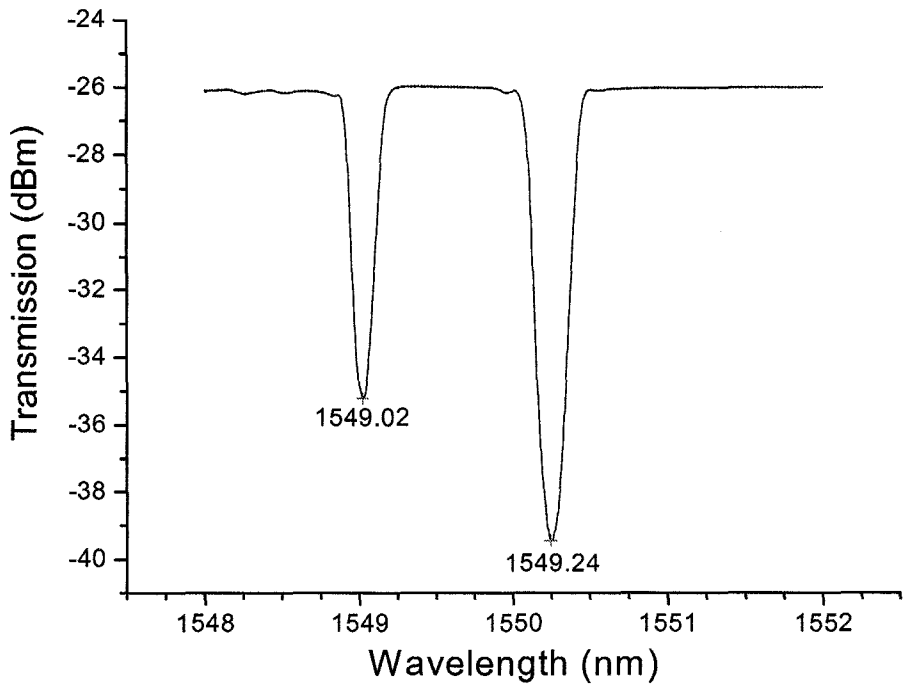

Figure 2-25: The transmission spectrum of the sensor system.

Table 2-2. Specifications of two types of polymer-coated FBGs.

	Polyimide-coated FBG	Acrylate-coated FBG
Fibre Type	SMF-28	SMF-28
Fibre Recoating Type	Polyimide	Acrylate
Grating length (mm)	10	10
Bragg Wavelength (nm) (in air, 20 °C)	1550.24	1549.02
Thickness (μm)	24.1±1.0	24.1±1.0
Bandwidth (nm)	0.29	0.17
Isolation (dB)	13	8
Reflection (%)	97.2	90.0

At first the temperature responses of the multiplexed FBG sensor in different environments were investigated. An microcomputer-controlled water bath and a environmental chamber were used to control the variation of the environmental temperature, in which the air and the water are the corresponding ambient media. Figure 2-26 illustrates the experimental setup used to determine the temperature-induced shift of the FBG transmission spectrum in the environmental chamber or the water bath. After these two sections of the polymer-coated FBGs were completely immersed in the water bath, sugar was added into the water to adjust the saccharinity of the solution. The relationship between the saccharinity of the sugar solution and the Bragg wavelength of the multiplexed FBG sensor will be investigated in the following sections.

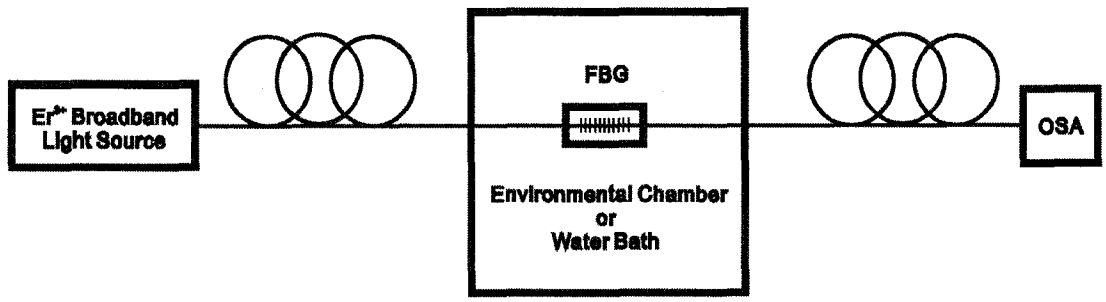

Figure 2-26: Schematic diagram of the humidity measurement system in the environmental chamber or water bath.

2.4.3 Simultaneous Measurement of Temperature and Saccharinity

In the measurement, part of the multiplexed FBG sensor with the polyimide-coated

grating section was immersed in the environmental chamber. The FBG sample was tightened to eliminate the strain or bending cross effects [99]. The relative humidity was set at 25 %RH first to simulate the indoor environment. The Bragg wavelength λ_B was initially 1550.21 nm at a temperature of 20 °C and gradually red-shifted with the increasing temperature in the environmental chamber, as shown in Fig. 2-27. The Bragg wavelength moved to 1550.954 nm at 90 °C, corresponding to a net shift of 0.744 nm. The temperature coefficient of the polyimide-coated FBG in the air, K_{Tair}, which is 0.0106 nm/°C, was obtained from the linear regression equation $\lambda_B = \lambda_0 + K_{Tair} \cdot T$.

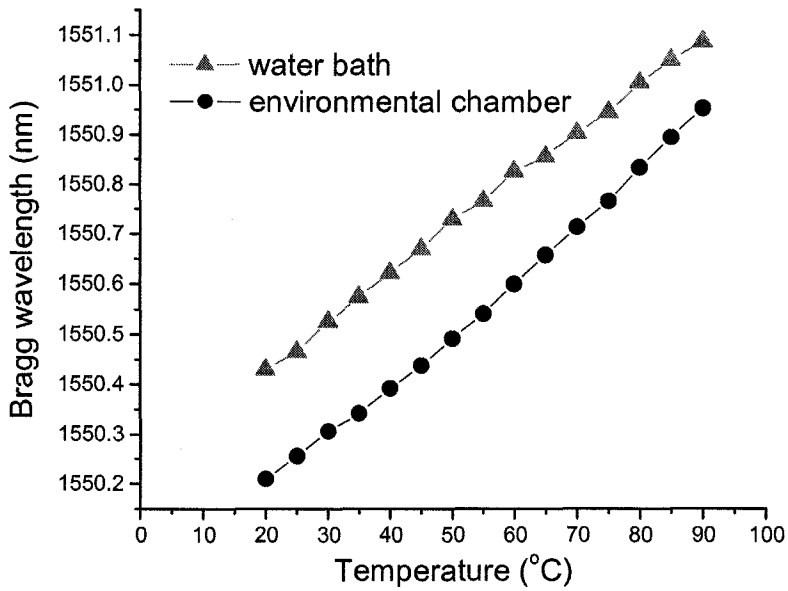

Figure 2-27: Bragg wavelength of the polyimide-coated FBG as a function of temperature in the environmental chamber and water bath.

Since the polyimide-coated FBG is sensitive to humidity [66], the transmission spectra of the polyimide-coated FBG during the process of increase in relative humidity

indicated the spectral shift towards longer wavelengths as shown in Fig. 2-28. The initial FBG resonance wavelength was 1550.19 nm at 13 %RH and gradually red-shifted with the relative humidity increase at a constant temperature of 20 °C in the environmental chamber. The resonance wavelength shifted to 1550.41 nm at 91 %RH, corresponding to a shift of 0.22 nm. The dependence of the Bragg wavelength λ_B on the change of relative humidity ΔRH can be fitted by the equation $\lambda_B = \lambda_0 + K_{RH} \cdot \Delta RH$, where K_{RH} is the resonance wavelength shift coefficient. In this case, the value for K_{RH} is 2.64×10^{-3} nm/%RH. This experimental value and the calculated value 2.6×10^{-3} nm/%RH agree very well.

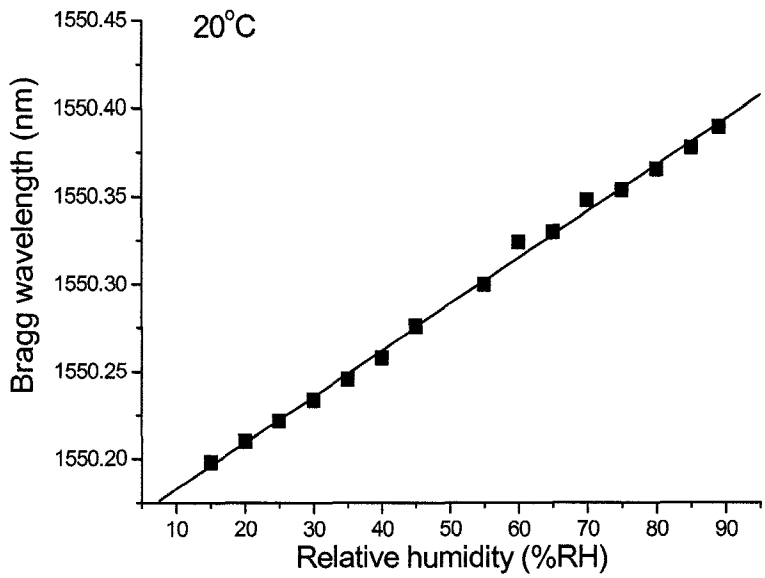

Figure 2-28: Bragg wavelength of the polyimide-coated FBG as a function of relative humidity in the environmental chamber.

The longitudinal expansion coefficient of the coated fibre is the sum of the

stiffness-weighted expansion coefficients of the bare fibre and of the coating [65],

$$\beta_{cf} = k_f \beta_f + k_c \beta_c \tag{2-13}$$

where $k_i = E_i A_i / \sum E_j A_j$ is the stiffness proportion. E_i is Young's modulus and A_i is the cross-section area.

From the relative humidity sensitivity $S_{RH} = 1.676 \times 10^{-6}\,\%\text{RH}^{-1}$ and Eqn. (2-4), we have

$$K_c = \frac{\beta_{cf}}{\beta_c} = \frac{S_{RH}}{(1-\hat{P}_e)\beta_c} = 0.0304. \tag{2-14}$$

By using the parameters in Table 2-1 and the radii of the single mode fibre and its core, the thickness of the polyimide coating can be calculated to be 24.0 μm from Eqn. (2-13). From an optical microscopy, the thickness of the polyimide coating was observed to be 24±1 μm, indicating an excellent agreement between the theoretical analyses and the experimental data.

When the polyimide-coated FBG was transferred from the environmental chamber (25 %RH) to the water bath at a constant temperature of 20 °C, it was found that the Bragg wavelength red-shifted from 1550.218 nm to 1550.408 nm and stabilized after half an hour (Fig. 2-29). Since the polyimide coating can absorb water and swell to stretch the fibre, the Bragg wavelength was increasing due to the expanding grating period which was caused by the stretched fibre. A net shift in the Bragg wavelength with an amount of 0.19 nm matches the above experimental results.

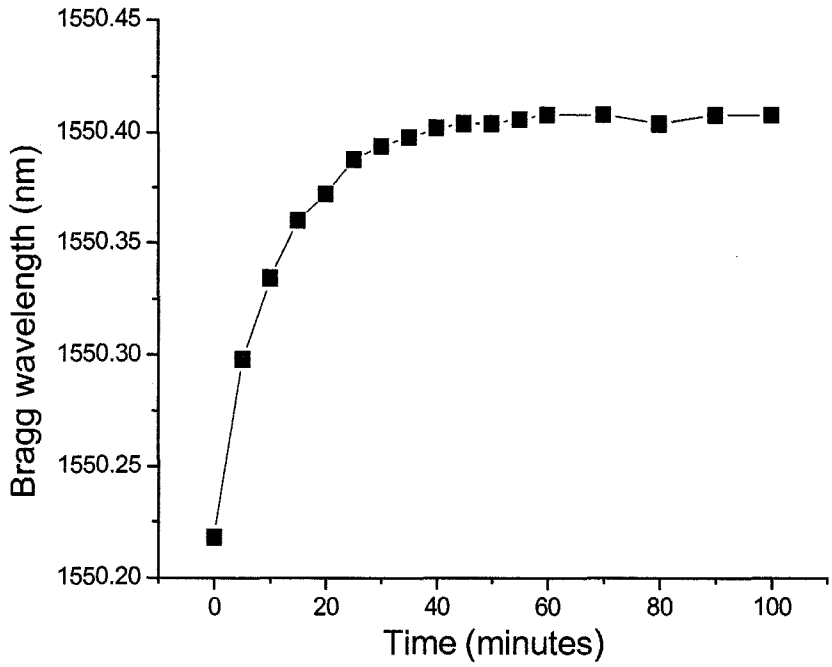

Figure 2-29: Time evolution of the Bragg wavelength of the polyimide-coated FBG transferred from the environmental chamber to the water bath.

In Eqn. (2-11), $D = 10^{-12}\,\mathrm{m^2/s}$ [110], $a = 62.5\,\mu\mathrm{m}$, $b = 86.5\,\mu\mathrm{m}$, and $C_{ext} = 1$. We consider D as a constant for the fibre coating with a radius between a and b. From Fig. 2-28, when we take $t = 2400\,\mathrm{s}$, we can obtain

$$c(24\mu m, t > 2400s) = 0.724\ (\mathrm{W/W\%}) \tag{2-15}$$

where W/W% stands for weight percentage. As for the above calculation, we assume that the layer thickness remains constant, the coating and fibre interface is impermeable, and the water diffuses perpendicularly to the layer surfaces.

After the transmission spectrum of the polyimide-coated FBG in the water bath

reached its stable conditions, the temperature was increased from 20 °C to 90 °C and the Bragg wavelength red shifted from 1550.430 nm to 1551.088 nm (Fig. 2-27). The temperature coefficient of the polyimide-coated FBG in water, K_{Twater}, was 0.0094 nm/°C, which is similar to its temperature coefficient in the air. Figure 2-27 indicates that, for the grating to be stored in either the environmental chamber or the water bath, the Bragg wavelength difference between the two cases decreases from 0.20 nm to 0.15 nm with the increase in temperature. This is mainly due to the reduced hydrophilic capability of the polyimide coating near the water boiling point.

Following the same procedure as mentioned above, the temperature responses of the acrylate-coated grating of the multiplexed FBG sensor in air and water were studied separately. In the environmental chamber, the temperature coefficient of the acrylate-coated grating in air, k_{Tair}, was 0.0099 nm/°C, which is shown in Fig. 2-30. During the process of transferring the acrylate-coated FBG from the environmental chamber to the water bath, no apparent Bragg wavelength shifts appeared (Fig. 2-31). From Fig. 2-30, the temperature coefficient in water, k_{Twater}, was measured to be 0.0102 nm/°C, nearly the same as k_{Tair}. The reason is that the acrylate coating FBG is not sensitive to the change of relative humidity, as indicated in Fig. 2-32.

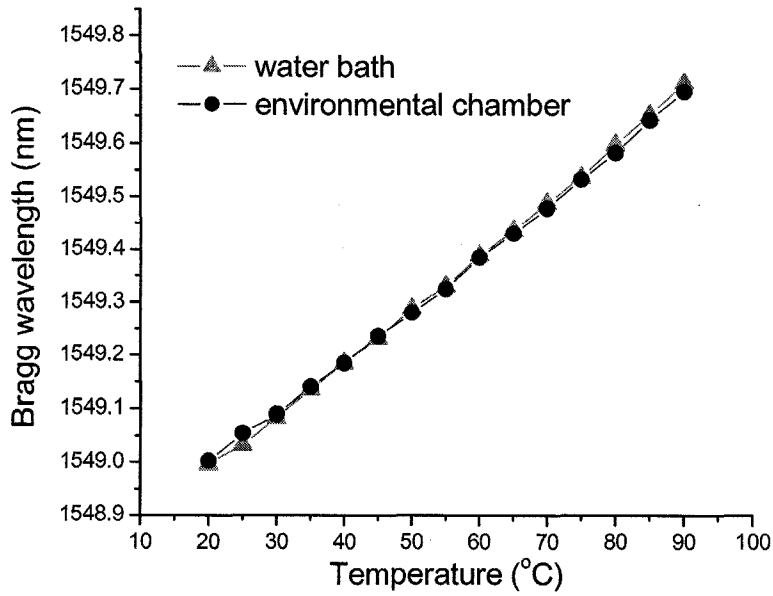

Figure 2-30: Bragg wavelength of the acrylate-coated FBG as a function of temperature in the environmental chamber and water bath.

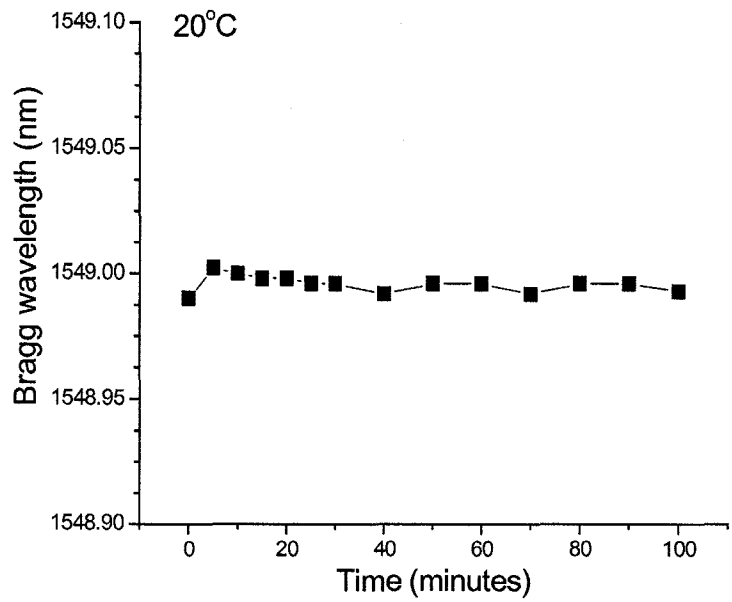

Figure 2-31: Time evolution of the Bragg wavelength of the acrylate-coated FBG transferred from the environmental chamber to the water bath.

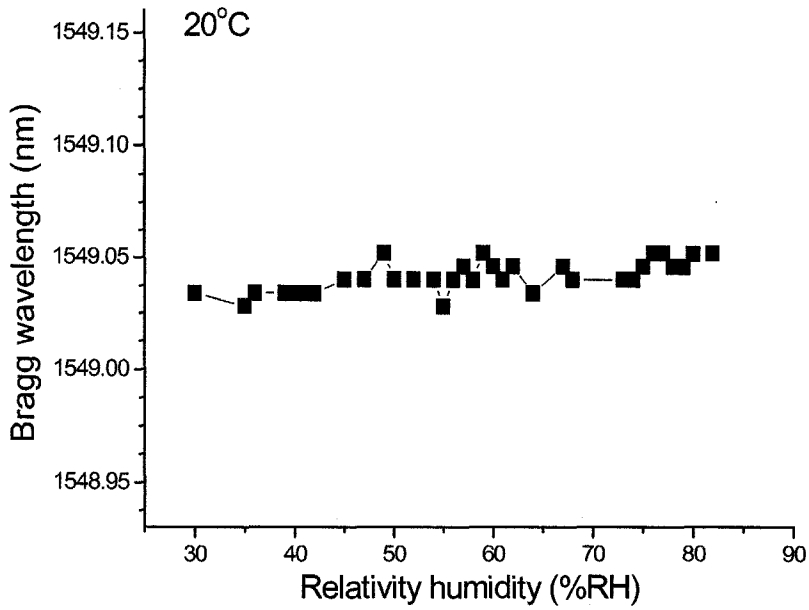

Figure 2-32: Bragg wavelength of the acrylate-coated FBG as a function of relative humidity in the environmental chamber.

After the polyimide-coated FBG and the acrylate-coated FBG were both completely immersed in the water bath for half an hour and kept the water temperature stable at 20 °C, natural granulated sugar was added to the water to produce desired sugar solutions of different saccharinities ranging from 0 to 50 °Bx. The transmission spectra of the polyimide-coated FBG as a function of sugar saccharinity are shown in Fig. 2-33. When the sugar was added into the water bath, the water concentration around the grating decreased, which resulted in the decrease of the corresponding water concentration in the polyimide coating in order to achieve equilibrium. In our experiments, for each time the sugar was added, sufficient waiting time was observed to make the FBG spectrum stable and the stabilization time was recorded.

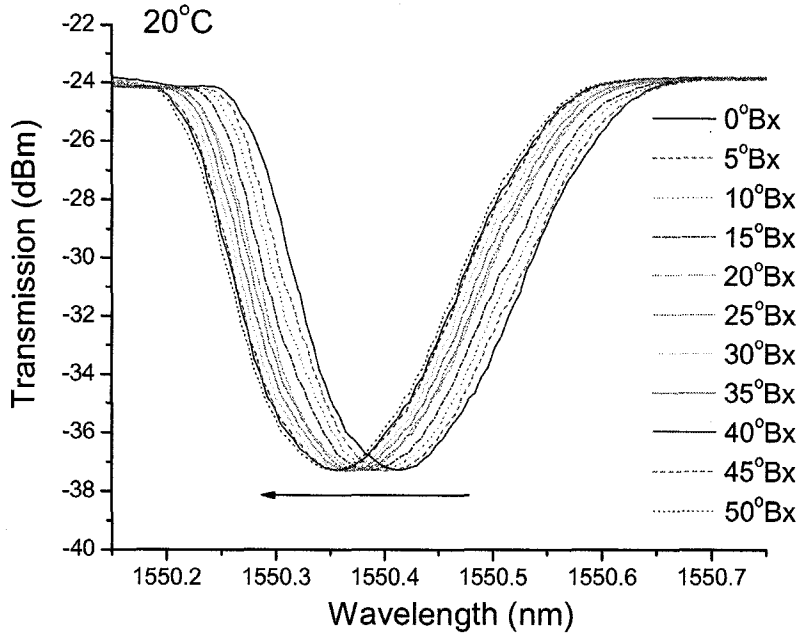

Figure 2-33: Transmission spectra of the polyimide-coated FBG as a function of sugar saccharinity.

According to Eqn. (12), the water concentration in the coating of the polyimide-coated FBG in different sugar solutions can be calculated. For the external water concentration gradually decreased from 1 to 0.5, as shown in Fig. 2-33, the diffusion stabilization time t are 280, 280, 280, 280, 280, 280, 250, 250, 250, and 230 s, respectively. Figure 2-34 shows the relationship between the water concentration in the coating of the polyimide-coated grating and the external sugar saccharinity. The decreasing diffusion stability time leads to less change in water concentration in the coating material.

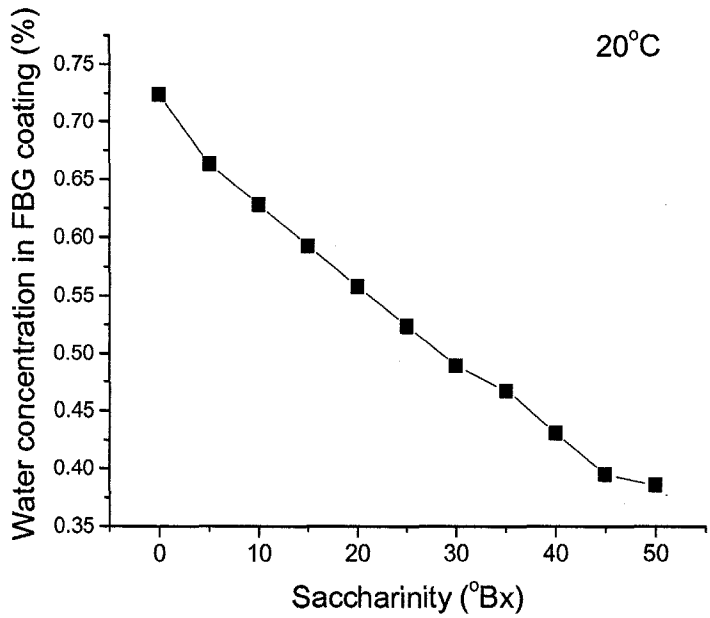

Figure 2-34: The relationship between the water concentrations in the coating of the polyimide-coated FBG and the external sugar saccharinity.

Figure 2-35 shows the Bragg wavelengths of the two FBGs as a function of saccharinity. The sensitivity drops when the polyimide-coated FBG is exposed to a higher saccharinity solution as it approaches saturation. It shows that the sensitivity of the polyimide-coated FBG on saccharinity is 0.0012 nm/°Bx. The comparison of Fig. 2-35 (a) with Fig. 2-34 indicates that the blue-shifted Bragg wavelength is in proportion to the water concentration in the coating material. Thus we obtain the relationship between the Bragg wavelength and the saccharinity,

$$\lambda_{Bragg,Bx} = \lambda_{Bragg,water} \cdot (1 - Bx) erf\left(\frac{r}{\sqrt{4Dt}}\right) \tag{2-16}$$

where $\lambda_{Bragg,water}$ is the Bragg wavelength in water, Bx is the saccharinity,

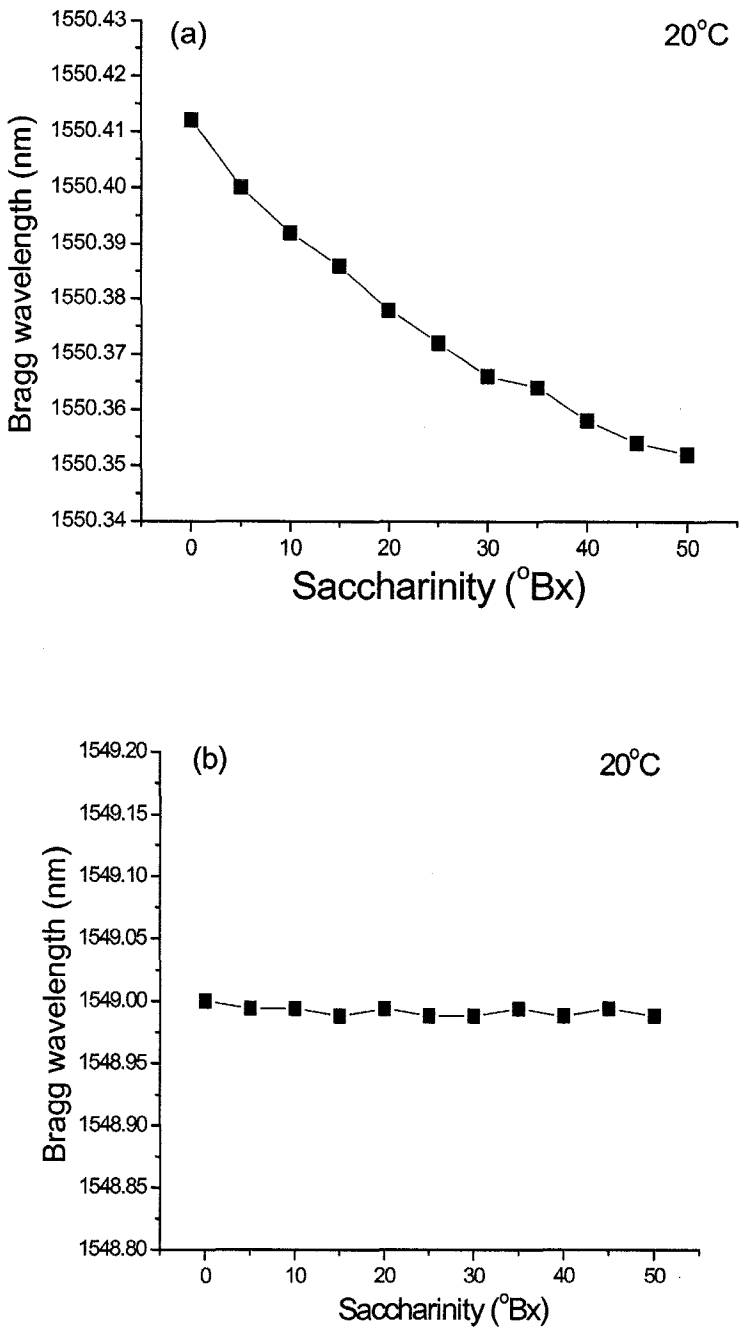

Figure 2-35: Bragg wavelengths as a function of saccharinity:
(a) polyimide-coated FBG, (b) acrylate-coated FBG

The shrinkage of the polyimide coating in sugar solutions resulted in the Bragg wavelength blue-shift of the polyimide-coated FBG, as shown in Fig. 2-35(a). However, the acrylate-coated FBG is not sensitive to the change of saccharinity in the sugar solution, as shown in Fig. 2-35(b). We define a character matrix M_{TS} to represent the sensing performance of the multiplexed sensor.

$$\begin{bmatrix} \Delta\lambda_1 \\ \Delta\lambda_2 \end{bmatrix} = M_{TS} \begin{bmatrix} \Delta T \\ \Delta S \end{bmatrix}. \tag{2-17}$$

In this particular case, the character matrix M_{TS} can be used to determine the variations in the saccharinity of water and its temperature from the readings of the wavelength shifts of the two gratings:

$$\begin{bmatrix} \Delta\lambda_{acrylate} \\ \Delta\lambda_{polyimide} \end{bmatrix} = \begin{bmatrix} 0.0102 & 0 \\ 0.0094 & 0.0012 \end{bmatrix} \begin{bmatrix} \Delta T \\ \Delta Bx \end{bmatrix}. \tag{2-18}$$

2.5 Salinity Sensitivity

The fibre optic sensor for simultaneous measurement of temperature and salinity with the multiplexed polymer-coated FBGs is proposed and demonstrated in this section. Following the same procedures for saccharinity measurement, the temperature responses in air and water were investigated. When the FBGs were completely immersed in the water bath, we added salt into the water gradually to increase the solution salinity from 0 to 25%. The transmission spectra of the polyimide-coated FBG as a function of salinity are shown in Fig. 2-36.

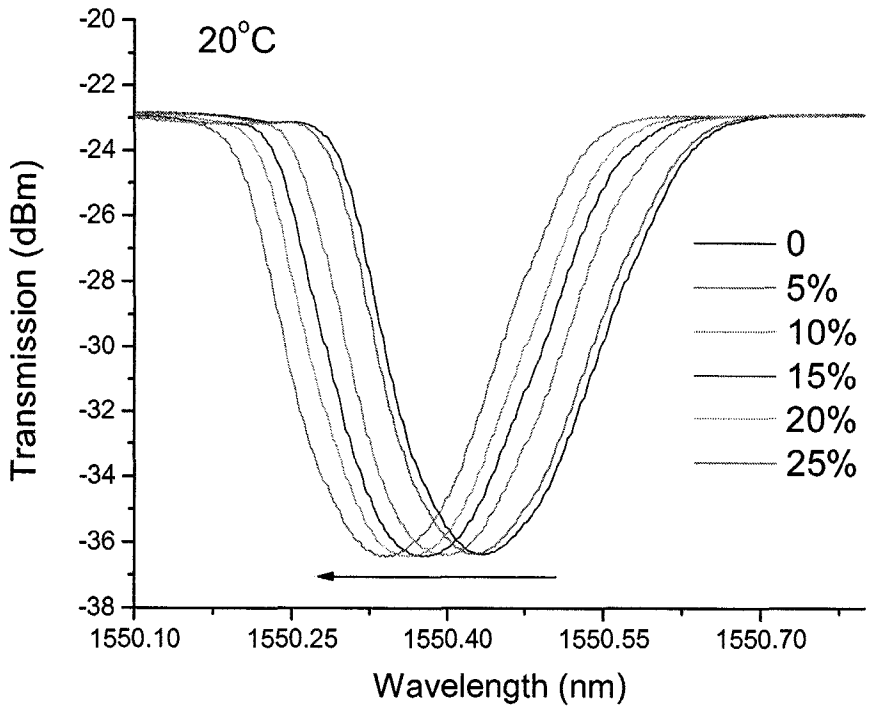

Figure 2-36: Transmission spectra of the polyimide-coated FBG as a function of salinity.

According to Eqn. (2-12), the water concentration in the coating of the polyimide-coated FBG in different salt solutions can be calculated. When the external water concentration gradually decreased from 1 to 0.75 (Fig. 2-36), the diffusion stabilization time t are 140, 165, 200, 260 and 410 s, respectively. Figure 2-37 shows the relationship between the water concentration in the coating of the polyimide-coated grating and the external salinity. A comparison of Fig. 2-34 with Fig. 2-37 shows that salt has a stronger water absorption capability than sugar. Figure 2-38 shows the Bragg wavelengths of the two FBGs as a function of salinity indicating that the sensitivity of

polyimide-coated FBG on salinity is 0.0038 nm/%S.

In this particular case, the character matrix M_{TS} can be used to determine the variations in the salinity of water and its temperature from the readings of the wavelength shifts of the two gratings:

$$\begin{bmatrix} \Delta\lambda_{acrylate} \\ \Delta\lambda_{polyimide} \end{bmatrix} = \begin{bmatrix} 0.0102 & 0 \\ 0.0094 & 0.0038 \end{bmatrix} \begin{bmatrix} \Delta T \\ \Delta S \end{bmatrix} \tag{2-19}$$

where ΔS is the change in salinity.

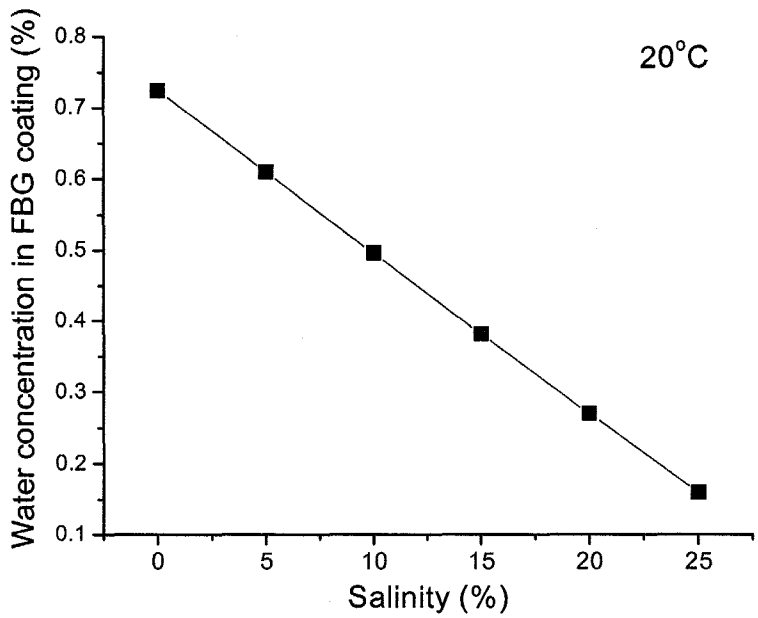

Figure 2-37: The relationship between the water concentrations in the coating of the polyimide-coated FBG and the external salinity.

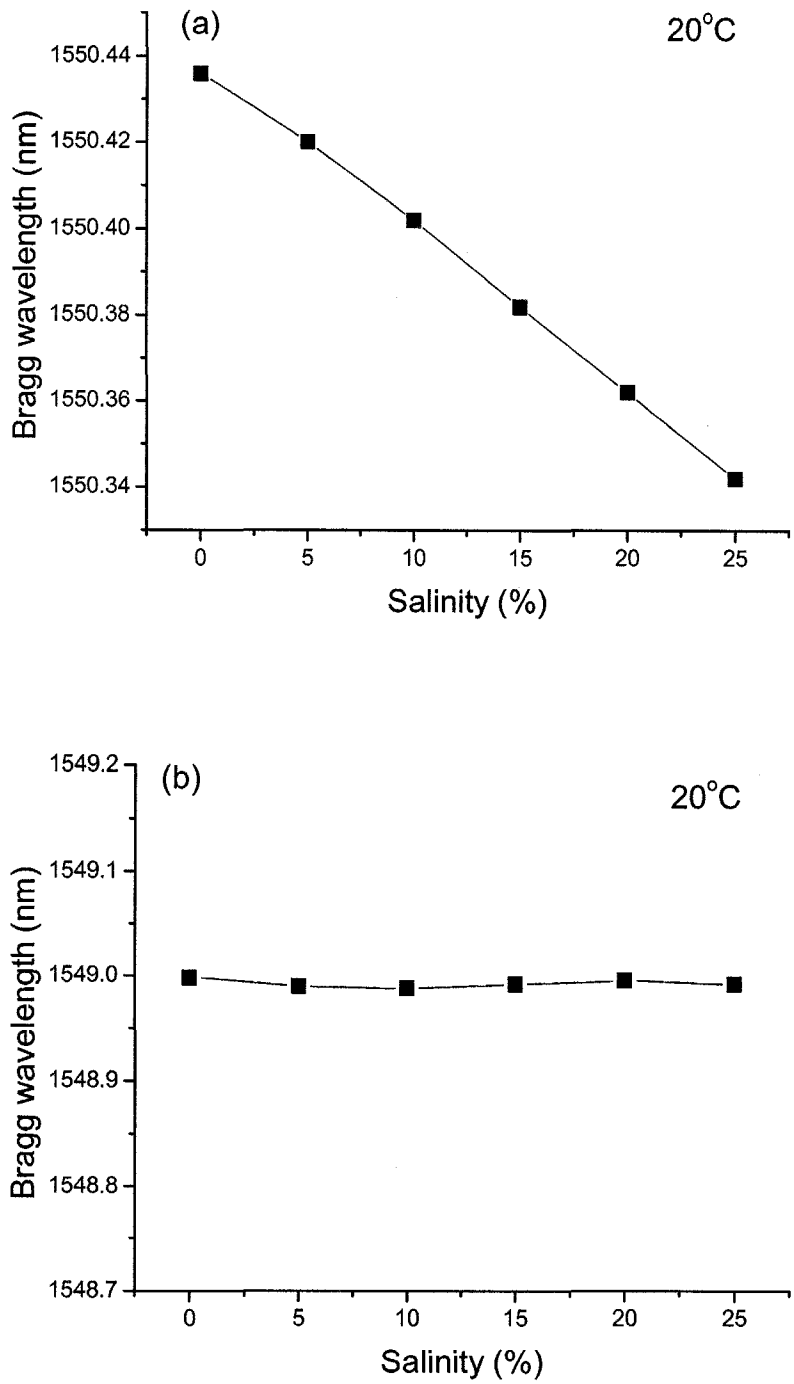

Figure 2-38: Bragg wavelengths as a function of salinity:
(a) polyimide-coated FBG, (b) acrylate-coated FBG.

2.6 Conclusion

This chapter presents several sensing applications of polyimide-coated and acrylate-coated FBGs including temperature, humidity, saccharinity and salinity. The temperature sensitivity in different environmental conditions was studied, which indicated that the temperature changes in different environmental conditions will all result in linear shifts of the Bragg resonant wavelengths of the FBGs. The comparison of sensing characteristics of polyimide- and acrylate-coating FBGs has been discussed. A new scheme for simultaneous measurement of temperature and saccharinity/salinity is proposed. This approach offers a number of advantages over other saccharinity/salinity measurement methods. With this multiplexed FBG sensor, we can utilize the polyimide-coated FBG to measure the saccharinity/ salinity while simultaneously measuring the temperature with the acrylate-coated FBG. Another advantage of this scheme is that only two Bragg wavelengths were monitored, which simplify the measurement systems. The scheme offers the possibility to introduce more wavelength channels to realize a quasi-distributed measurement. With the simple FBG fabrication process and recoating technique, the scheme proposed here will result in low cost saccharinity/salinity sensor devices. Since the two sensing elements have been integrated on one standard single mode telecommunication fibre, it is possible to achieve quasi-distributed in-situ measurement of temperature and saccharinity/salinity over a long distance. Fibre Bragg gratings are attractive sensing elements because they exhibit a response that is reversible, accurate, and stable over long time periods, can be used for

absolute measurements, and can be readily applied to in-line multiplexed sensor chains.

Chapter 3

Strain Sensitivity

3.1 Introduction

Fibre Bragg gratings have been demonstrated as useful fibre optic devices for a growing range of sensing applications including axis strain, bending, and other physical quantities. The strain sensitivity of a FBG and its sensing applications will be discussed in this chapter. Though FBG sensors have several unique advantages over their electrical counterparts, their widespread use had been plagued by their inability effectively discriminate between temperature and strain effects. In this chapter, a method using two different polymer-coated FBGs to simultaneously measure axial strain and temperature is proposed. Results of bending effects are reported by using two different steel bars in a simple steel-mounted FBG bending sensor. Theoretical error analysis and experimental

results of the sensor performance for measuring bending are discussed. A water flow sensor which can measure both the flux and the direction of water flow is fabricated based on the FBG bending sensing principle proposed here. Results of the experimental results show excellent agreement with the theoretical analyses.

3.2 Axial Strain Sensitivity

3.2.1 Theory of Axial Strain Sensitivity

The Bragg wavelength, λ_B, of a FBG is defined by

$$\lambda_B = 2n_{eff}\Lambda \tag{3-1}$$

where n_{eff} is the effective refractive index, Λ is the Bragg grating pitch and $n_{eff} \cdot \Lambda$ is the optical spacing of the periodic refractive index structure which forms the FBG.

The refractive index and Bragg wavelength are highly temperature dependent via the thermo-optic coefficient and, to a lesser extent the thermal expansion coefficient. The refractive index and Bragg wavelength are also dependent upon stress via the photoelastic constants and the mechanically induced elongation. The Bragg wavelength shift as a function of the physical elongation and the Pockels coefficients is described by [101]

$$\Delta\lambda_B = \lambda_B\left(1-\hat{P}_e\right)\varepsilon \tag{3-2}$$

and

$$\hat{P}_e = \frac{n_{eff}^2}{2}\left[P_{12} - \upsilon\left(P_{11}+P_{12}\right)\right] \tag{3-3}$$

where ε is strain; υ is the Poisson ratio; λ_B and $\Delta\lambda_B$ are the Bragg wavelength and its shift respectively, $\hat{P}_e$ is an effective strain optic term, and P_{11}, P_{12} and P_{44} are the strain tensor components related to axial loading where $P_{12} = P_{11} - 2P_{44}$ due to the cylindrical symmetry of the system.

The component of the Bragg wavelength shift which is directly due to the physical elongation of the Bragg grating spacing under tension, is determined by Eqns. (3-2) and (3-3) with $\hat{P}_e$ equal to zero. The $\hat{P}_e$ term modifies the Bragg wavelength shift due to the Pockels coefficients and reduces the overall observed Bragg wavelength shift in fused silica for a given strain by 21%, to a typical strain sensitivity of 1.22 pm/με for a FBG at 1550 nm. The values for P_{11} and P_{44} are 0.113 and -0.069, respectively [57, 102].

3.2.2 Experimental Setup for Axial Strain Sensing Measurement

In this experiment, the strain dependence of acrylate-coated FBG was studied by stretching the FBG axially at a constant temperature (20°C), as shown in Fig. 3-1. An erbium-doped broadband light source was used as the light source. Light passing through the FBG was received by the optical spectrum analyzer. The fibre sample was fixed to two linear translation stages (ATS100, Aerotech, Inc) using epoxy glue in which one

stage was used as a fixed stage and the other one as a motion stage. The accuracy of the motion stage is 1.0 μm. The strain was adjusted by applying tensile force to the FBG. The FBG sample was placed on the thermoplate (Sigma systems) where the temperature was kept constant. Different tensile forces were applied to the FBG with a motion stage through GPIB and LabVIEW control. The front panels of the LabVIEW driver program for the UNIDEX511 motion controller is shown in Fig. 3-2.

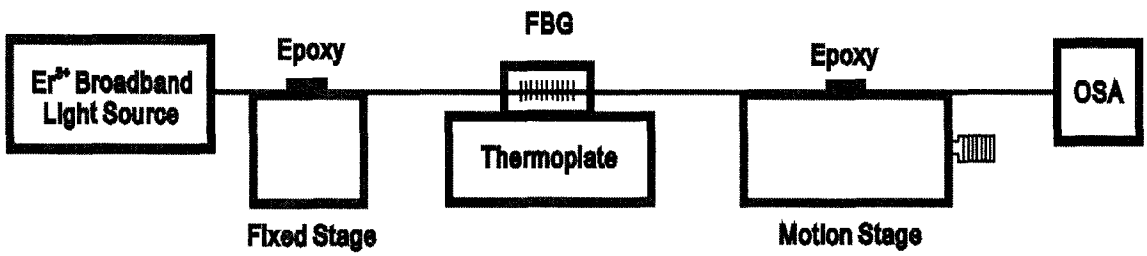

Figure 3-1: Schematic diagram of the axial strain measurement system.

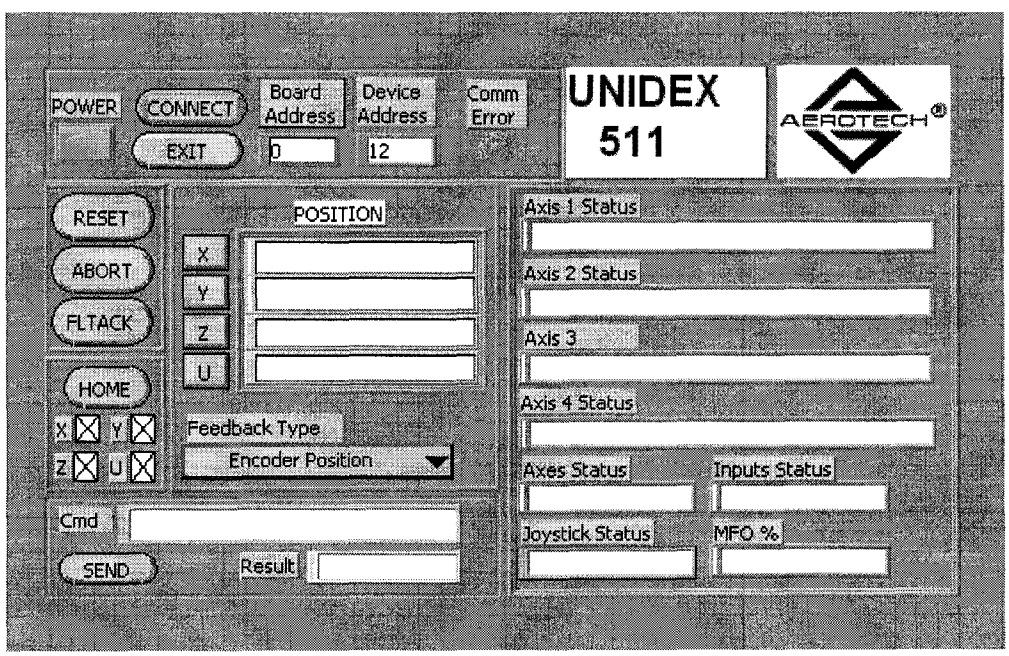

Figure 3-2: The front panel of the driver program for the UNIDEX511 motion controller.

3.2.3 Fibre Bragg Grating Axial Strain Sensing Response

The environmental temperature around the FBG sample was kept at 20 °C. The fibre length between the two epoxy glued points was 742.5 mm. The strain value was changed from 0 to 800 με with a step of 50 με. At each specific stretching state, sufficient time was allowed for the system to stabilize. The change of Bragg grating wavelength as a function of increasing axial strain is shown in Fig. 3-3.

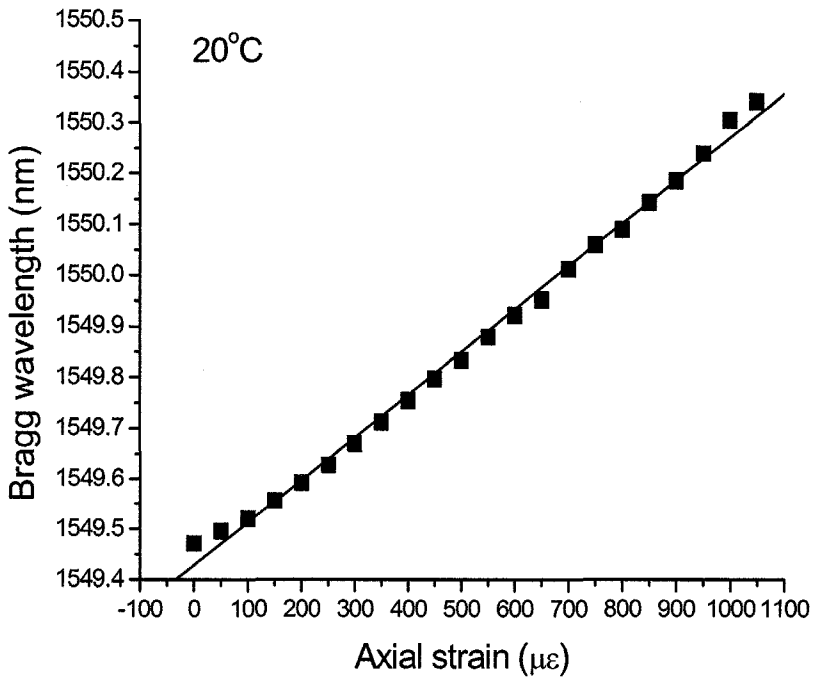

Figure 3-3: Bragg wavelength of the acrylate-coated FBG as a function of axial strain.

The wavelength shift of the FBG resonant peaks with respect to the increasing axial strain was measured to be 0.829 pm/με. The theoretical strain sensitivity at 1550 nm is a

1.22 pm change as a result of applying 1με to the Bragg grating [64]. It is noticed that the experimental value is smaller than the theoretical value, which is mainly due to the effect of the coating layer. The coating layer and the epoxy glue are well fixed in the experiments, however sliding between the coating and cladding of the fibre was observed. The strain force was not directly applied on the FBG whereas on the coating area which resulted in the discrepancy between experimental and theoretical value.

3.3 Simultaneous Measurement of Temperature and Axial Strain

3.3.1 Operation Principle

Fibre Bragg gratings showed excellent performance as temperature and strain sensors. However temperature and strain cannot be determined separately by only measuring the wavelength shift of one FBG sensor, which is sensitive to both measurands. A number of techniques have been reported to overcome this limitation [103-107].

In this section, simultaneous measurements of strain and temperature are realized based on the measurement of the different characteristic wavelength shifts of two types of FBGs. The sensor has two gratings with close Bragg wavelengths written in two spliced sections of a single mode SMF-28 fibre with identical geometry: one of them was recoated with polyimide and the other one with acrylate. In this way, a compact sensing

element with two Bragg gratings of different strain sensitivities and temperature sensitivities can be integrated.

For Eqn. (2-1),

$$\Delta\lambda_B = 2\left(\Lambda\frac{\partial n}{\partial l} + n\frac{\partial \Lambda}{\partial l}\right)\Delta T + 2\left(\Lambda\frac{\partial n}{\partial l} + n\frac{\partial \Lambda}{\partial l}\right)\Delta l \tag{2-1}$$

the first term represents the temperature effect on an optical fibre, while the second term describes the strain effect on an optical fibre. This corresponds to a change in the grating spacing and the strain-optic induced change in the refractive index. The term related with the strain effect may be expressed as

$$\Delta\lambda_B = \lambda_B\left(1 - \hat{P}_e\right)\varepsilon \tag{3-2}$$

where $\hat{P}_e$ is an effective strain-optic constant defined as

$$P_e = \frac{n^2}{2}\left[P_{12} - \upsilon\left(P_{11} + P_{12}\right)\right]. \tag{3-3}$$

From Eqns. (2-2) and (3-2), the expected sensitivity at a 1550 nm Bragg grating is a 1.22 pm/με and the expected temperature sensitivity at a 1550 nm Bragg grating is approximately 0.0137 nm/°C.

3.3.2 Simultaneous Temperature and Axial Strain Sensing Measurement

In this section, we investigated the temperature and axial strain sensitivity of polyimide-coated FBG and acrylate-coated FBG. Due to their different sensitivities,

simultaneous temperature and axial strain sensing measurement can be realized.

The experimental setup for this work is shown in Fig. 3-1. For the polyimide-coated FBG, the fibre length between the two fixed points was 728.5 mm. At first, a thermoplate was used to keep the FBG temperature at 20 °C. The strain value was changed from 0 to 1000 με with a step of 50 με. Figure 3-4 shows that the wavelength shift of the FBG resonant peaks with respect to the increasing axial strain was measured to be 0.972 pm/με.

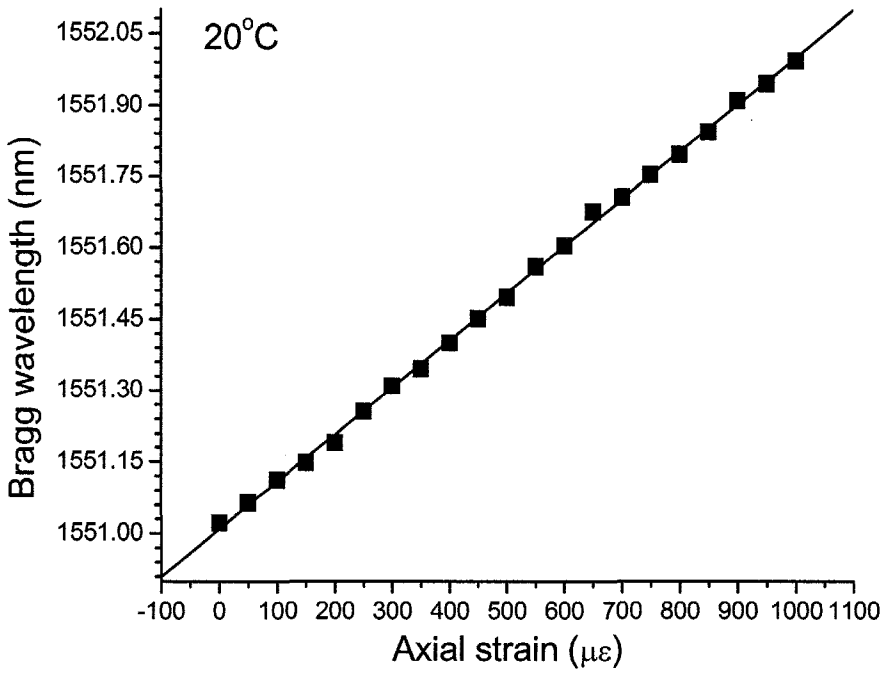

Figure 3-4: Bragg wavelength of the polyimide-coated FBG as a function of axial strain at 20 °C.

The measurement was carried out at different axial strain values from 0 to 1000 με with a step of 200 με. At each axial strain value, the Bragg wavelength as a function of

temperature was measured. Figure 3-5 gives the dependence of the Bragg wavelength of the polyimide-coated FBG on temperature under different axial strain values. The axial strain sensitivities at temperatures of 30, 40, 50, 60, 70, and 80 °C are 0.972, 1.002, 1.002, 1.002, 0.984, and 0.978 pm/με, respectively. The average axial strain sensitivity is 0.99 pm/με that is close to the sensitivity derived from Fig. 3-4. The temperature sensitivities at different strain levels of 0, 200, 400, 600, 800, and 1000 με are 0.0095, 0.0093, 0.0093, 0.0091, 0.009, and 0.0096 nm/°C, respectively. The average temperature sensitivity is 0.0093 nm/°C.

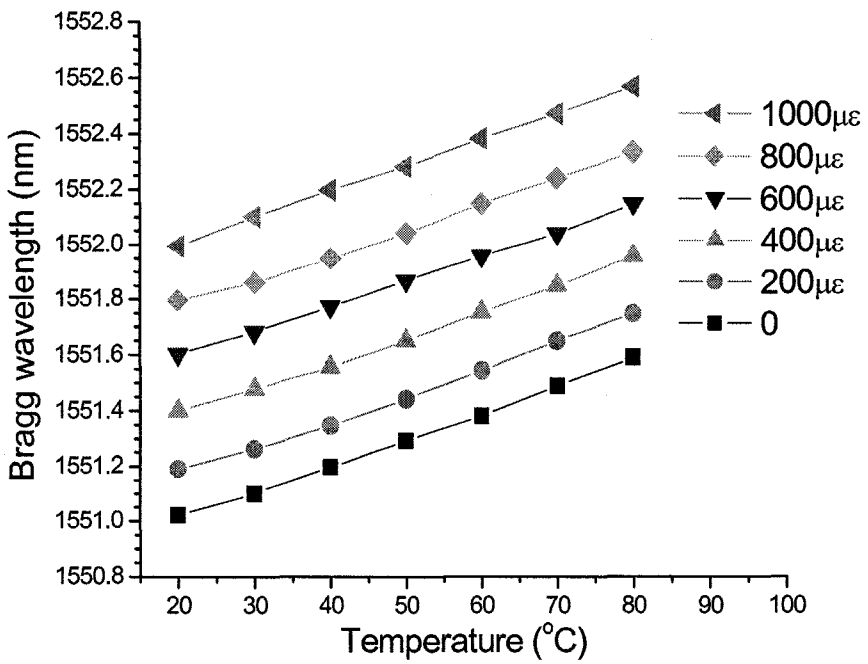

Figure 3-5: Bragg wavelength of the polyimide-coated FBG as a function of temperature under different axial strain values.

For the acrylate-coated FBG, the fibre length between two fixed points was 742.5 mm. At first, a thermoplate was used to keep the FBG temperature at 20 °C. The strain value was changed from 0 to 1000 με with a step of 50 με. Figure 3-6 shows that the wavelength shift of the FBG resonant peaks with respect to the increasing axial strain was measured to be 0.738 pm/με.

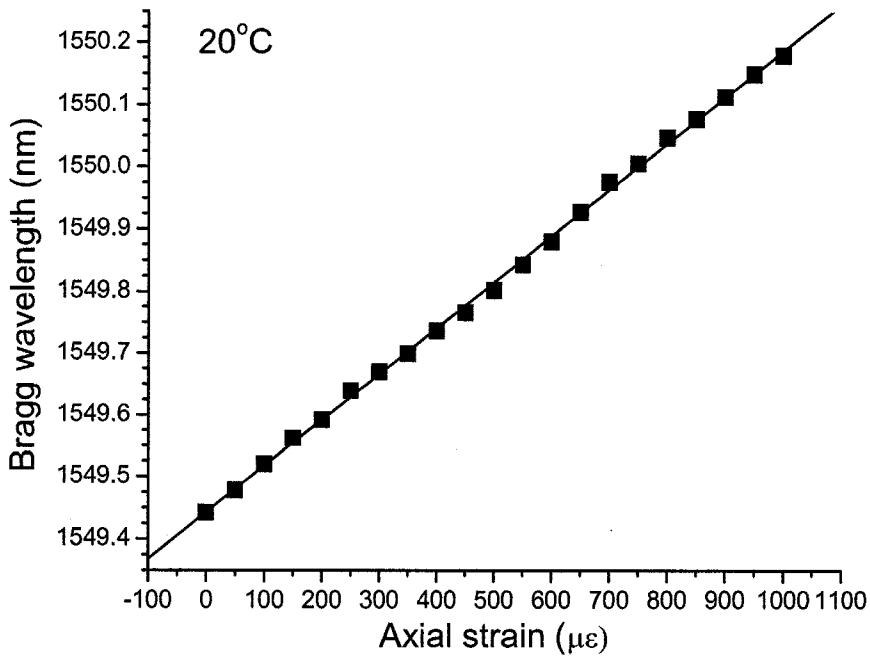

Figure 3-6: Bragg wavelength of the acrylate-coated FBG as a function of axial strain at 20 °C.

The measurement was carried out at different axial strain values from 0 to 1000 με with a step of 200 με. At each axial strain value, the Bragg wavelength as a function of temperature was measured. Figure 3-7 gives the dependence of the Bragg wavelength of the acrylate-coated FBG on temperature under different axial strain values. The axial

strain sensitivities at temperatures of 30, 40, 50, 60, 70, and 80 °C are 0.732, 0.714, 0.72, 0.732, 0.738, and 0.756 pm/με, respectively. The average axial strain sensitivity is 0.732 pm/με that is close to the sensitivity derived form Fig. 3-6. The temperature sensitivities at different strain levels of 0, 200, 400, 600, 800, and 1000 με are 0.0083, 0.0082, 0.0079, 0.0081, 0.0087, and 0.0083 nm/°C, respectively. The average temperature sensitivity is 0.0083 nm/°C.

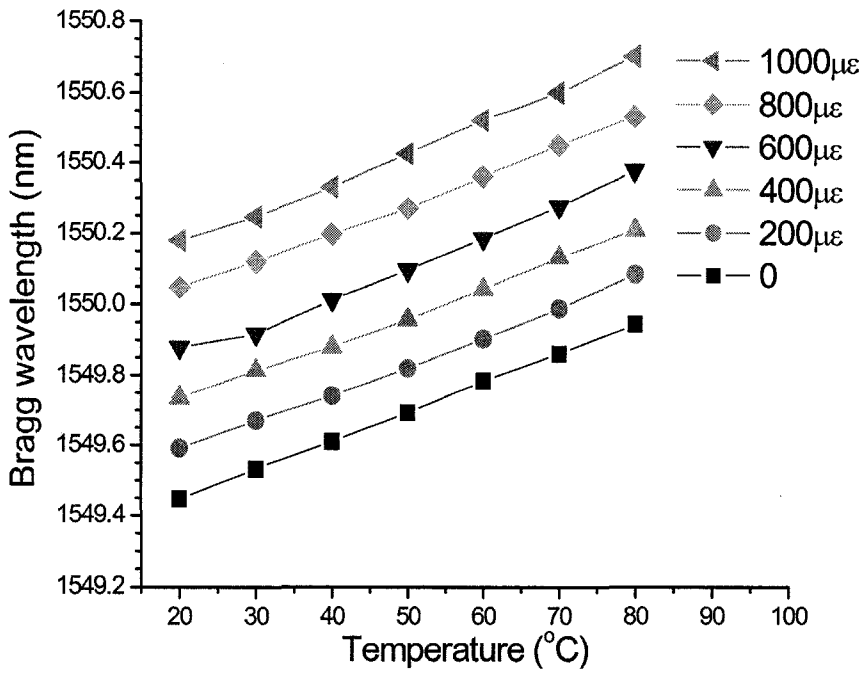

Figure 3-7: Bragg wavelength of the acrylate-coated FBG as a function of temperature under different axial strain values.

Figures 3-8 and 3-9 show the responses of the two sensing gratings to the applied temperature and strain variations, respectively. Different temperature and axial strain

sensitivities are observed for the two gratings. In this case, the character matrix $M_{T\varepsilon}$ can be used to determine the variations in the axial strain and temperature from the amounts of the wavelength shifts of the two gratings:

$$\begin{bmatrix} \Delta\lambda_{acrylate} \\ \Delta\lambda_{polyimide} \end{bmatrix} = \begin{bmatrix} 0.0083 & 732 \\ 0.0093 & 990 \end{bmatrix} \begin{bmatrix} \Delta T \\ \Delta\varepsilon \end{bmatrix}. \tag{3-4}$$

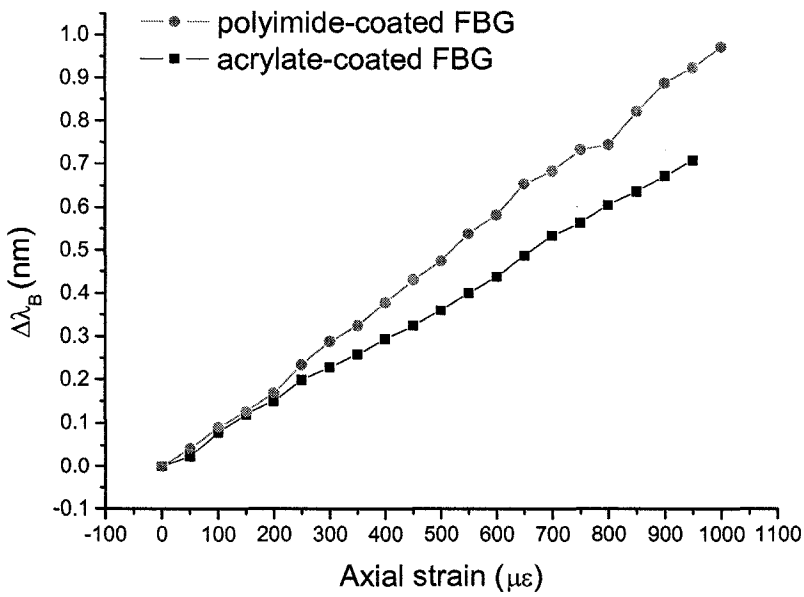

Figure 3-8: Dependence of the Bragg wavelength shifts of the polyimide- and acrylate-coated FBGs on the axial strain.

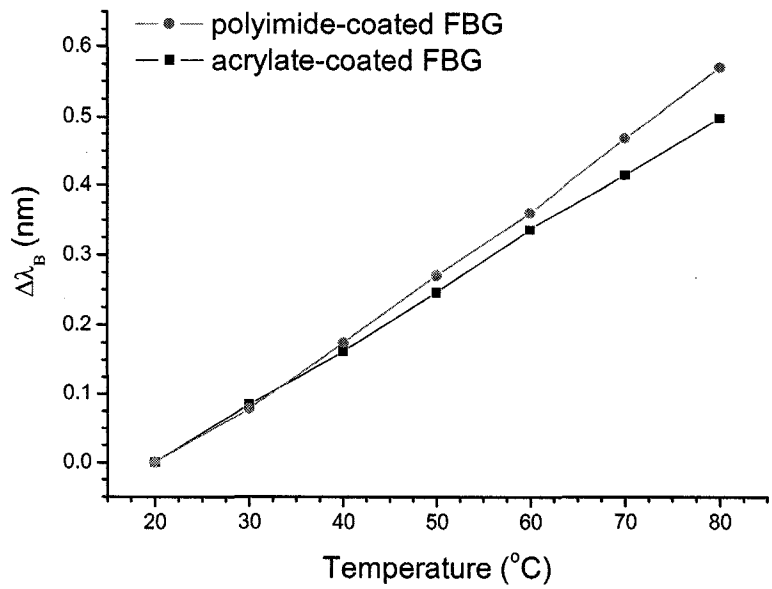

Figure 3-9: Dependence of the Bragg wavelength shifts of the polyimide- and acrylate-coated FBGs on the temperature.

The character matrix, as the most important parameter of a multiplexed polymer-coated FBG sensor system, provides us with a new approach to predict the axial strain and temperature simultaneously applied to the sensor system, that is to say, the cross sensitivity of the axial strain and temperature has been perfectly resolved.

3.4 Bending Sensitivity

3.4.1 Experimental Setup for Bending Sensing Measurement

In this section the bending sensitivity of an acrylate-coated FBG was investigated in

detail. The schematic diagram of the FBG bending measurement is shown in Fig. 3-10. An erbium-doped broadband source was used as a light source. Light passing through the FBG was received by the optical spectrum analyzer. The fibre was attached on one side of a steel bar using epoxy glue. The steel bar was fixed onto a vertical frame. The FBG sample was in air at 20 °C. The bending effect of the steel bar was generated with a motion stage (ATS100, Aerotech, Inc.) controlled by a personal computer through GPIB and LabVIEW program. The motion stage move forward and from either side of the steel bar to change the bending direction. During the process of attaching the fibre onto the steel bar, the fibre was stretched to produce a pre-strained state. The motion stage moved forward to induce a convex bending on the steel bar and hence the FBG that stayed in a stretched state. When the motion stage was installed on the opposite side of the steel bar, the FBG on the steel bar experienced concave bending and stayed in a shrunk state. The deformation process is illustrated in Fig. 3-11.

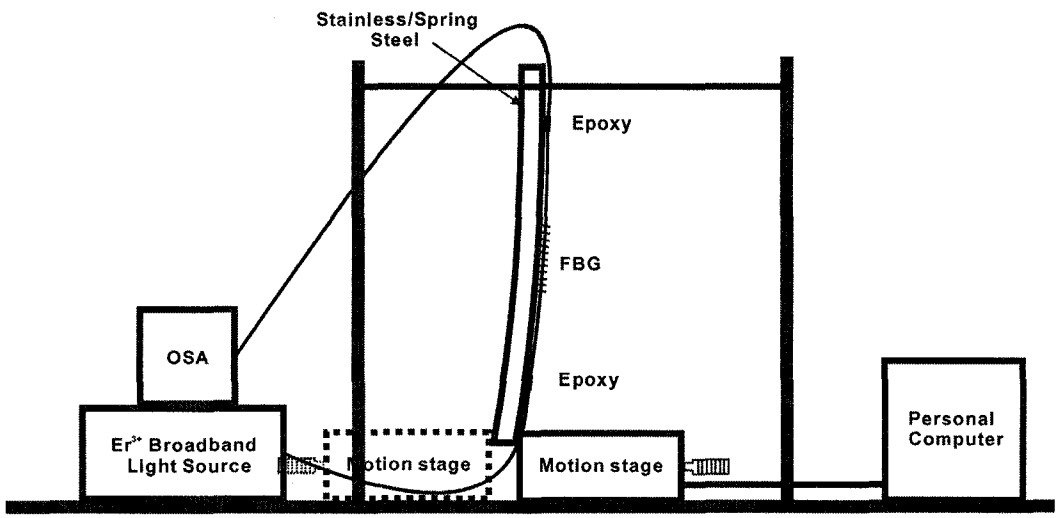

Figure 3-10: Schematic diagram of the bending measurement system.

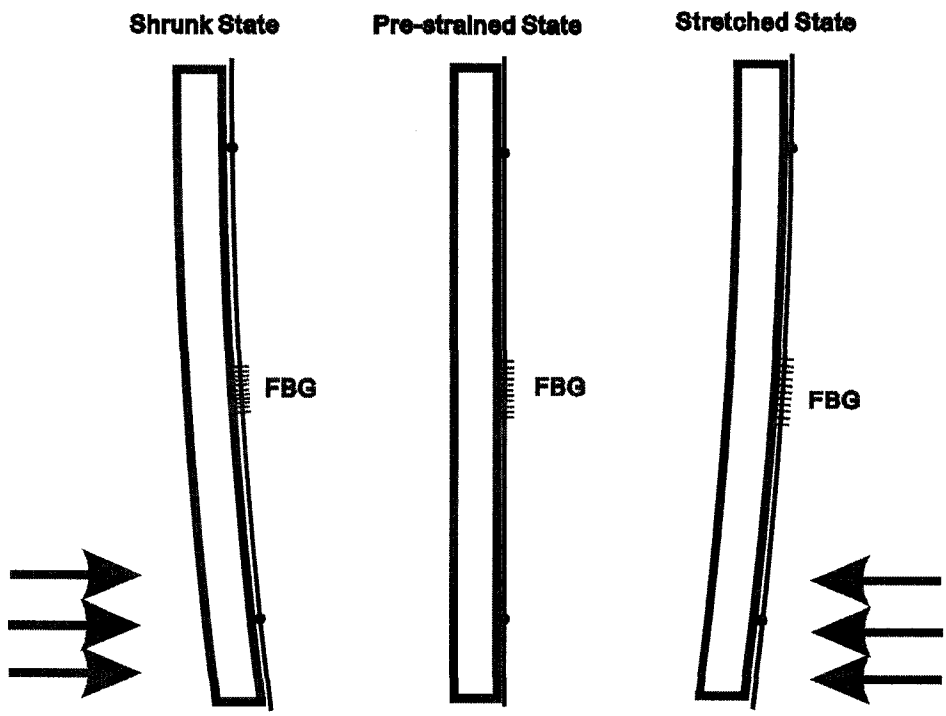

Figure 3-11: Deformation of a FBG on a steel bar under two-directional impacts.

3.4.2 Operation Principles of Bending Measurement

Figure 3-12 shows the schematic diagram of fibre elongation. For an initial segment of the steel bar, denoted as $\overline{AC}$ in Fig. 3-12 with an initial length of L, it becomes an arc AB with an effective length of L' after convex bending. It is obvious from the figure that, for the angle θ corresponding to the arc AB, the fibre length change from its initial value of l to l' after convex bending during the forward shift of the motion stage with an amount of D. The elongation length Δl of the fibre can be calculated using the geometry relation

$$\tan\left(\frac{\pi}{2}-\frac{\pi-\theta}{2}\right)=\frac{D}{L} \tag{3-5}$$

and

$$\left[2\pi(R+d)-2\pi R\right]\cdot\frac{\theta}{2\pi}\cdot\frac{l}{L}=\Delta l\,. \tag{3-6}$$

After substituting Eqn. (3-6) into Eqn. (3-5), the relationship between Δl and D is

$$\Delta l=\frac{2dl}{L}\arctan\left(\frac{D}{L}\right). \tag{3-7}$$

Following Eqn. (3-2), the Bragg wavelength shift is

$$\Delta\lambda_B=\frac{2d\lambda_B\left(1-\hat{P}_e\right)}{L}\arctan\left(\frac{D}{L}\right). \tag{3-8}$$

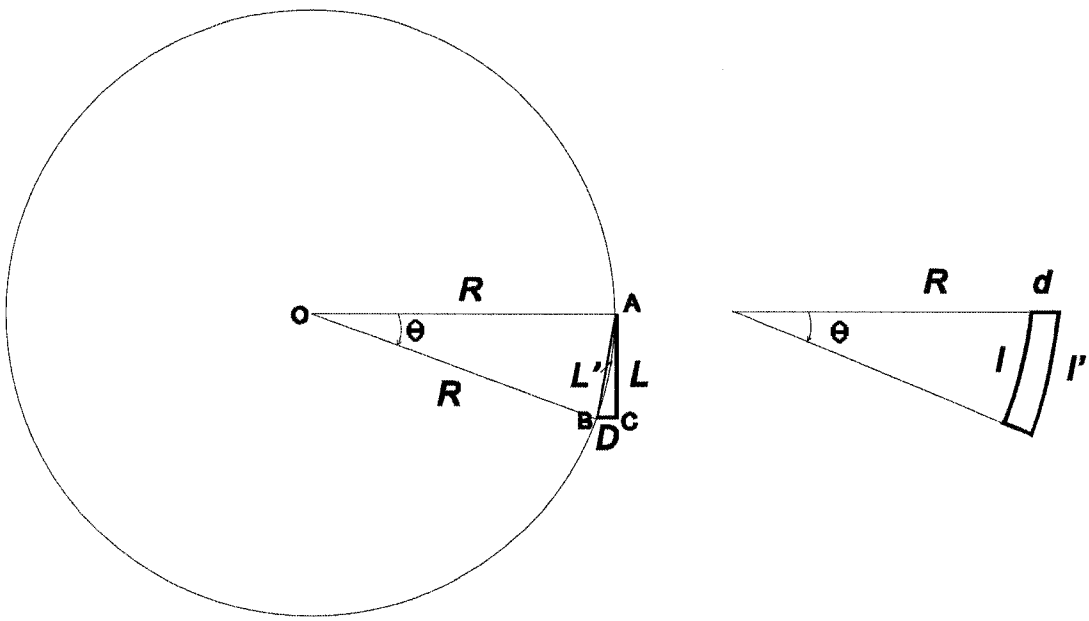

Figure 3-12: Schematic diagram of fibre elongation.

For an initial segment of steel bar, denoted as $\overline{AC}$ in Fig. 3-13 with an initial length of L, it becomes an arc AB with an effective length of L' after concave bending. It is obvious from the figure that, for the angle θ corresponding to the arc AB, the fibre length change from its initial length of l to l' after concave bending during the forward shift of the motion stage with an amount of D. The elongation length Δl of the fibre can be calculated using the geometry relation. The shortened length Δl of the fibre can be calculated from the geometry relation in Fig. 3-13

$$\tan\left(\frac{\pi}{2}-\frac{\pi-\theta}{2}\right)=\frac{D}{L} \tag{3-9}$$

and

$$[2\pi R-2\pi(R+d)]\cdot\frac{\theta}{2\pi}\cdot\frac{l}{L}=\Delta l\,. \tag{3-10}$$

From Eqns. (3-9) and (3-10), the relationship between Δl and D becomes

$$\Delta l=\frac{2dl}{L}\arctan\left(\frac{D}{L}\right). \tag{3-11}$$

Following Eqn. (3-2), the Bragg wavelength shift is given by

$$\Delta\lambda_B=\frac{2d\lambda_B\left(1-\hat{P}_e\right)}{L}\arctan\left(\frac{D}{L}\right). \tag{3-12}$$

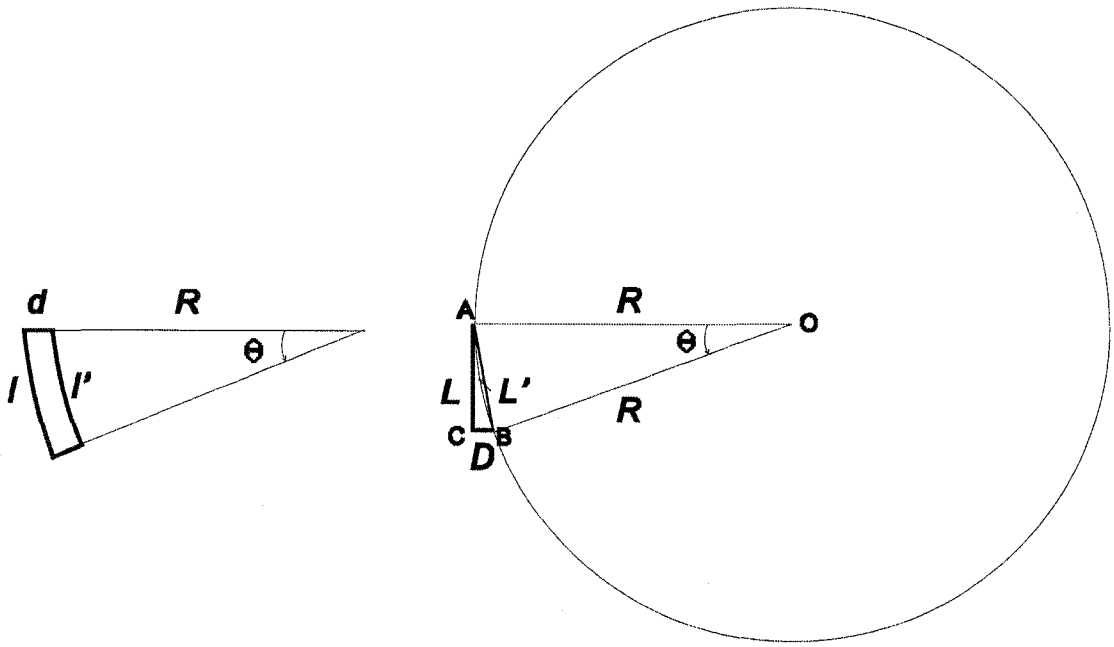

Figure 3-13: Schematic diagram of fibre shrinkage.

3.4.3 Micro-bending Sensing Measurement with a Stainless Steel Bar-mounted Fibre Bragg grating

In the bending sensing experiment, we used two different steel-mounted FBG schemes. First we adopted a stainless steel bar-mounted FBG, which is shown in Fig. 3-12 with a fibre length of 200 mm. The top section (30 mm) of the steel bar was fixed and the bottom section (10 mm) was pushed by the motion stage. The effective length of the steel bar was 260 mm.

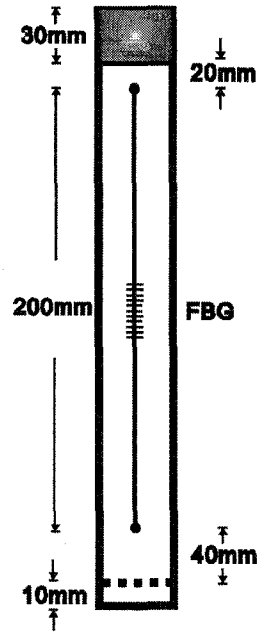

Figure 3-14: Schematic diagram of the stainless steel bar-mounted fibre Bragg grating.

The motion stage located on the side of the fibre with regard to the steel bar moved forward 27 mm at a step of 1 mm. At each specific position, the Bragg wavelength was recorded by the OSA. The Bragg wavelength as a function of shift imposed by the motion stage is given in Fig. 3-15. It shows that the red-shift of the FBG resonant peak wavelength with respect to the increasing bending shift was measured to be 0.192 nm. When the motion stage was separated from the fibre by the steel bar and moved forward 7 mm in steps of 1 mm, the Bragg wavelength as a function of the shift imposed by the motion stage is shown in Fig. 3-16. This figure indicates that the blue-shift of the FBG resonant peak wavelength with respect to the increasing bending radius was measured to be 0.051 nm. After passing this length, the Bragg wavelength did not shift any more due

to the relaxation of the fibre. Further increase in the bending shift of the steel bar did not influence the change in the Bragg wavelength. Figure 3-17 gives the dependence of the Bragg wavelength of the FBG on the bending shift at 20 °C. It is obvious that the stainless steel bar-mounted FBG can distinguish both the rate and the direction of bending.

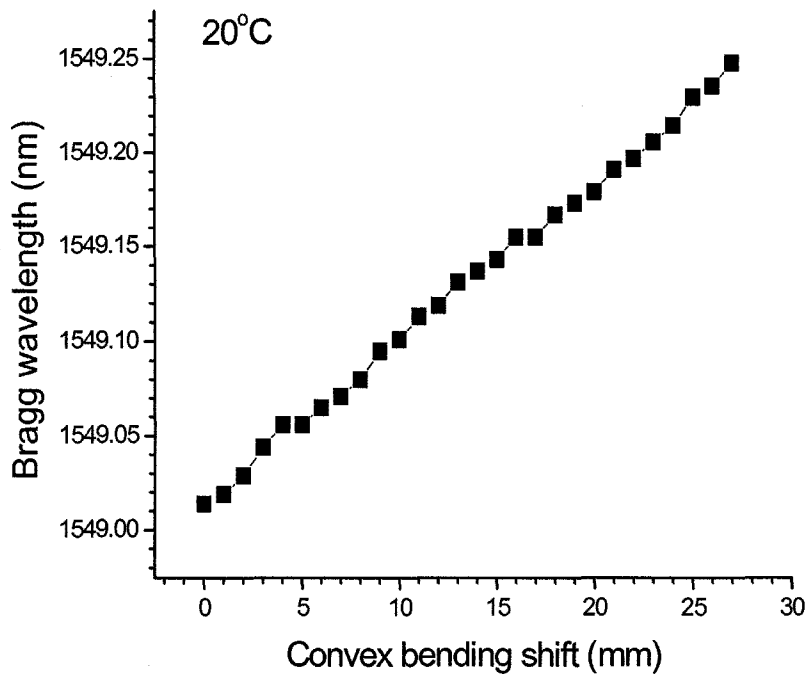

Figure 3-15: Bragg wavelength of the FBG during the convex bending at 20°C.

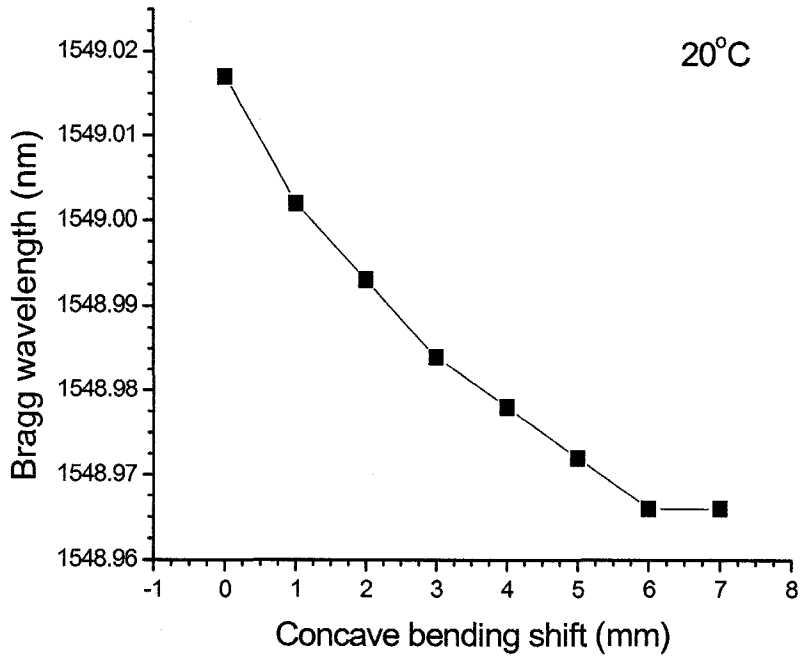

Figure 3-16: Bragg wavelength of the FBG during the concave bending at 20 °C.

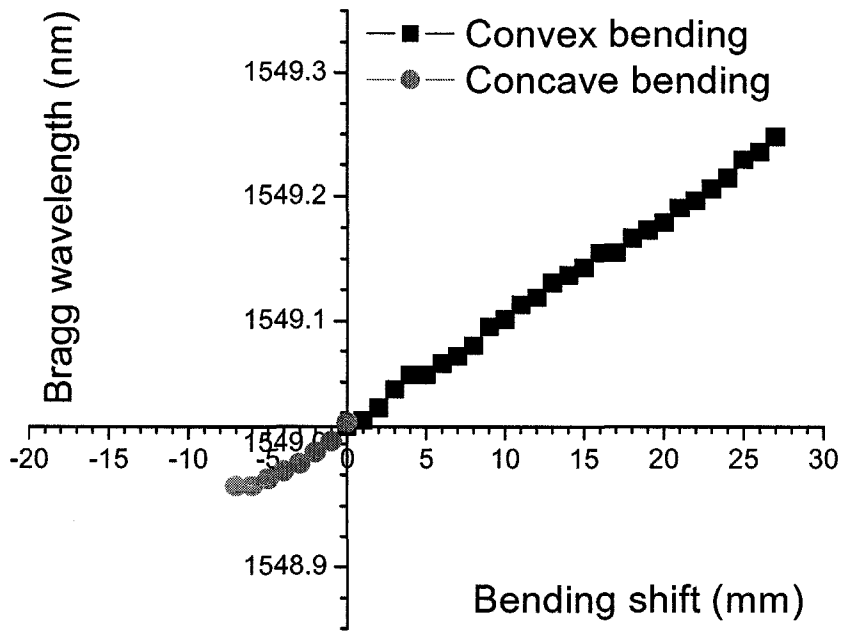

Figure 3-17: Dependence of the Bragg wavelength of the FBG on the bending shift at 20 °C.

For the stainless steel bar-mounted FBG, the coating thickness was 250 μm and the initial length of the steel bar was 260 mm. The shifts of the convex and concave bending were 27 mm and 7 mm, respectively. From Eqn. 3-8, the Bragg wavelength shift due to the stretched fibre can be found to be 0.242 nm. The simulation result of a Bragg centre wavelength shift as a function of bending is approaching the experimental value of 0.192 nm. From Eqn. 3-12, we obtained the Bragg wavelength shift due to the shrunk fibre to be 0.054 nm. The simulation result of the Bragg wavelength shift as a function of the bending is in good agreement with the experimental value of 0.051 nm. Figure 3-18 gives the simulation result of the dependence of the Bragg wavelength of the FBG on the bending shift.

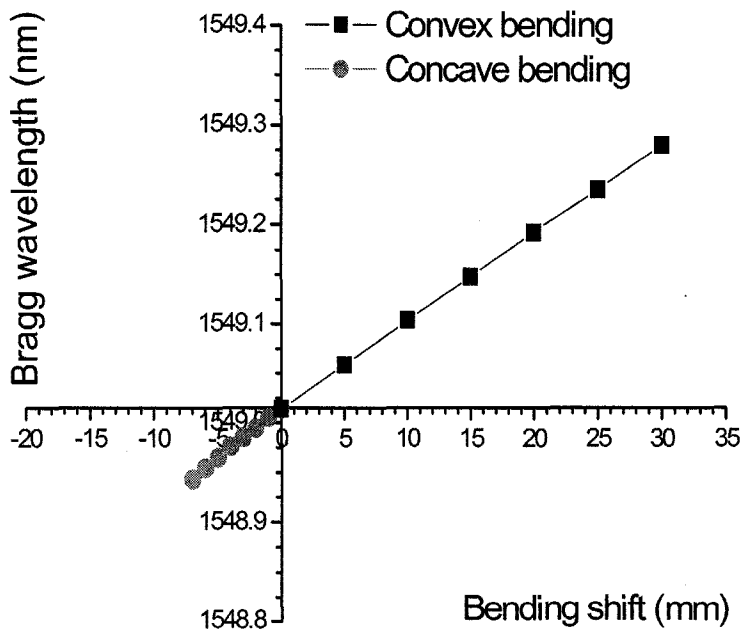

Figure 3-18: Simulation result of the dependence of the Bragg wavelength of the FBG on the bending shift.

3.4.4 Macro-bending Sensing Measurement with a Spring Steel Bar-mounted Fibre Bragg Grating

In order to evaluate the FBG sensing response under different bending effects, a spring steel bar was adopted as the mounting host for the FBG. Spring steel has a very high yield strength, which allows it return to its original shape easily despite of significant bending. Figure 3-19 shows the schematic diagram of the spring steel bar-mounted FBG. The fibre length was 180 mm. The top section (30 mm) of the steel bar was fixed and the bottom section (10 mm) was pushed by the motion stage.

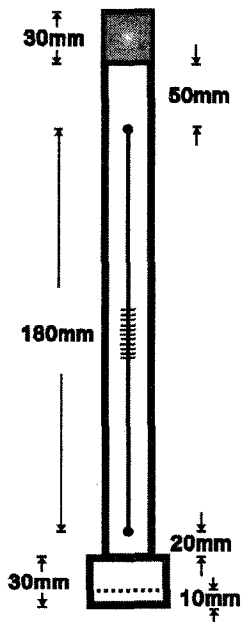

Figure 3-19: Schematic diagram of the spring steel bar-mounted fibre Bragg grating.

The motion stage located on the side of the fibre with regard to the steel bar moved forward 90 mm in steps of 1 mm. At each specific position, the Bragg wavelength was recorded by the OSA. The Bragg wavelength as a function of shift imposed by the motion stage was given in Fig. 3-20. It shows that the red-shift of the FBG resonant peak wavelength with respect to the increasing bending shift was measured to be 0.716 nm. The motion stage was separated from the fibre by the steel bar and moved forward 11 mm at a step of 1 mm. The Bragg wavelength as a function of the shift imposed by the motion stage was given in Fig. 3-21. It shows that the blue-shift of the FBG resonant peak wavelength with respect to the increasing bending radius was measured to be 0.097 nm. After passing this position, the Bragg wavelength did not shift any more due to the relaxation of the fibre. Further increase in the bending shift of the steel bar did not influence the change in the Bragg wavelength. Figure 3-22 gives the dependence of the Bragg wavelength of the FBG on the bending shift at 20 °C. It is obvious that the spring steel bar-mounted FBG can distinguish both the magnitude and the direction of bending.

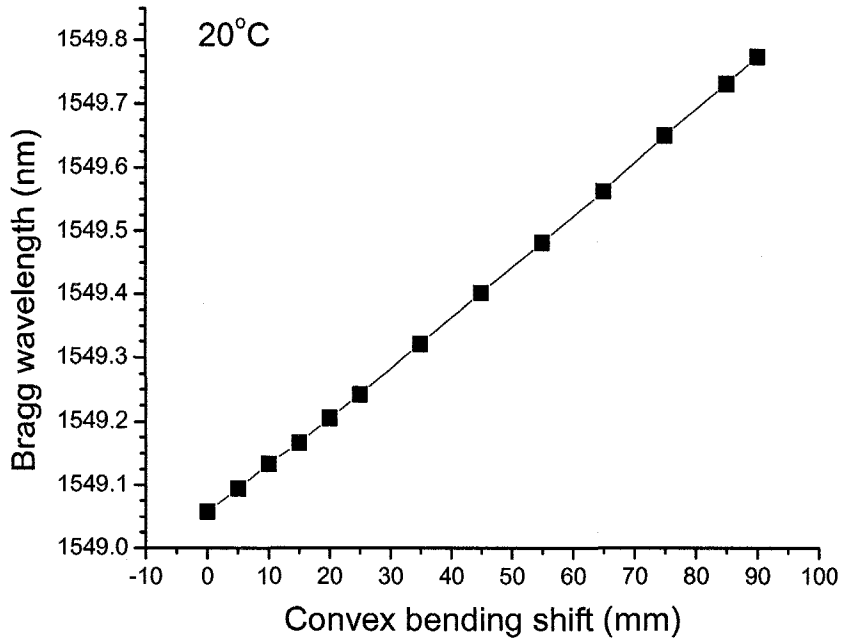

Figure 3-20: Bragg wavelength of the FBG during the convex bending 20 °C.

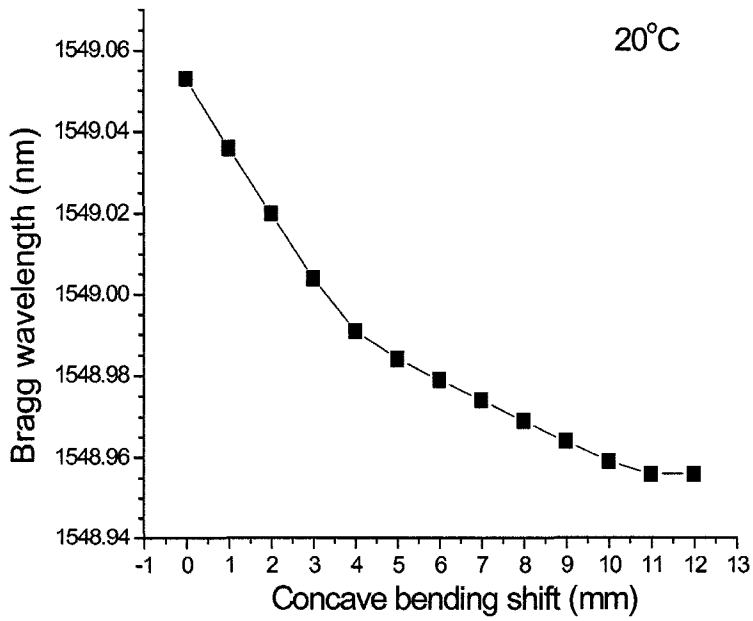

Figure 3-21: Bragg wavelength of the FBG during the concave bending 20 °C.

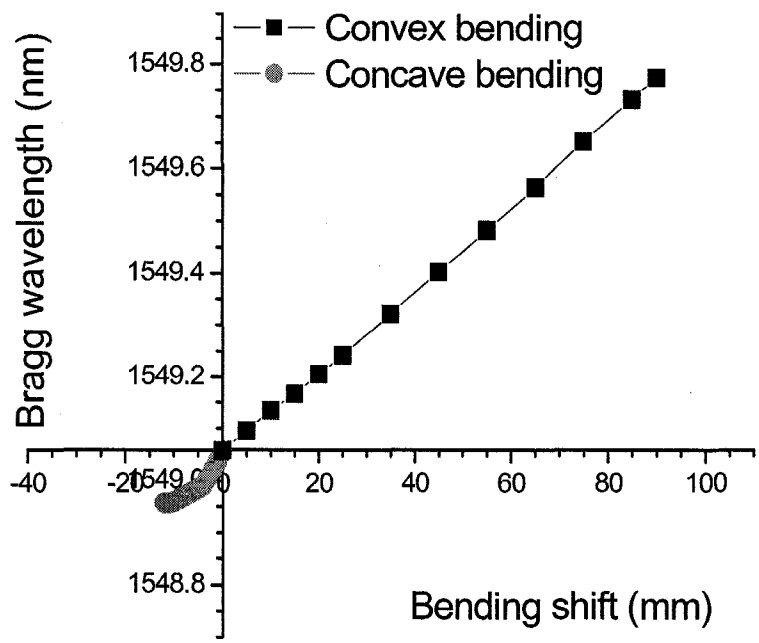

Figure 3-22: Bragg wavelength as a function of motion stage shift at 20 °C.

For the spring steel bar-mounted FBG, the coating thickness is 250 μm and the initial effective length of the steel bar is 270 mm. The shifts of convex and concave bending are 90 mm and 11 mm, respectively. From Eqn. (3-8), the Bragg wavelength shift due to the stretched fibre can be found as 0.727 nm. The simulation result of a Bragg centre wavelength shift as a function of bending is approaching the experimental value 0.716 nm. From Eqn. (3-12), we get the Bragg wavelength shift due to the shrink fibre is 0.100 nm. The simulation result of the Bragg wavelength shift as a function of bending is in good agreement with the experimental value of 0.097 nm. Figure 3-23 gives the simulation result of the dependence of the Bragg wavelength of the FBG on bending shift.

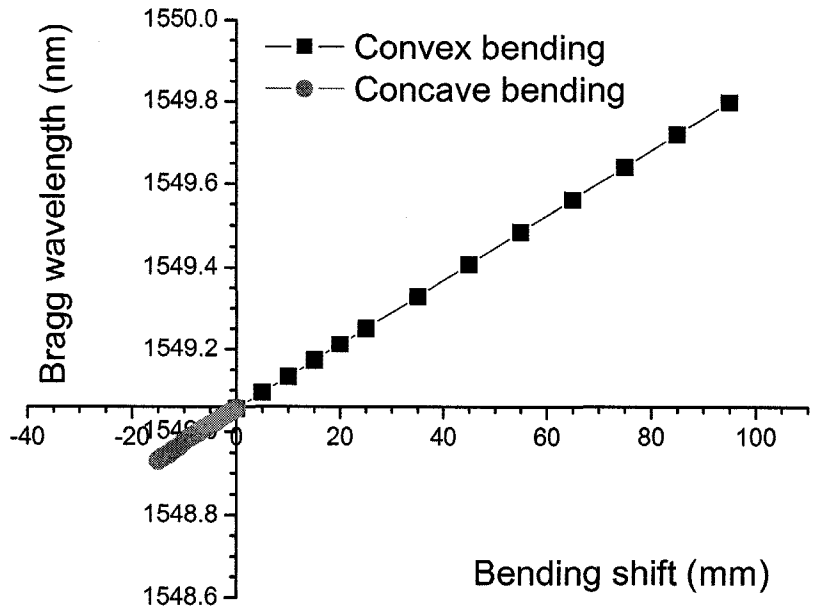

Figure 3-23: Simulation result of the dependence of the Bragg wavelength of the FBG on the bending shift.

3.5 Water Flow Measurement

In this section water flow measurement using acrylate-coated FBG will be discussed. The schematic diagram of the FBG water flow measurement is shown in Fig. 3-24. An erbium-doped broadband source was used as a light source. Light passing through the FBG was received by the optical spectrum analyzer. The fibre was attached on one side of a steel bar using epoxy glue. The steel bar was fixed onto a vertical frame. The FBG sample was kept in air at 20 °C. The steel bar was bent by the impact of water flow.

Change in the water flow direction resulted in the change in the steel bar bending direction. During the process of attaching the fibre onto the steel bar, the fibre was stretched to produce a pre-strained state. The water flow strikes the steel bar from the same side of the fibre with regard to the stainless/spring steel in order to induce a convex bend on the steel bar for the FBG to stay in a stretched state. When the water flows oppositely, the FBG on the steel bar will experience concave bending and stay in a shrunk state.

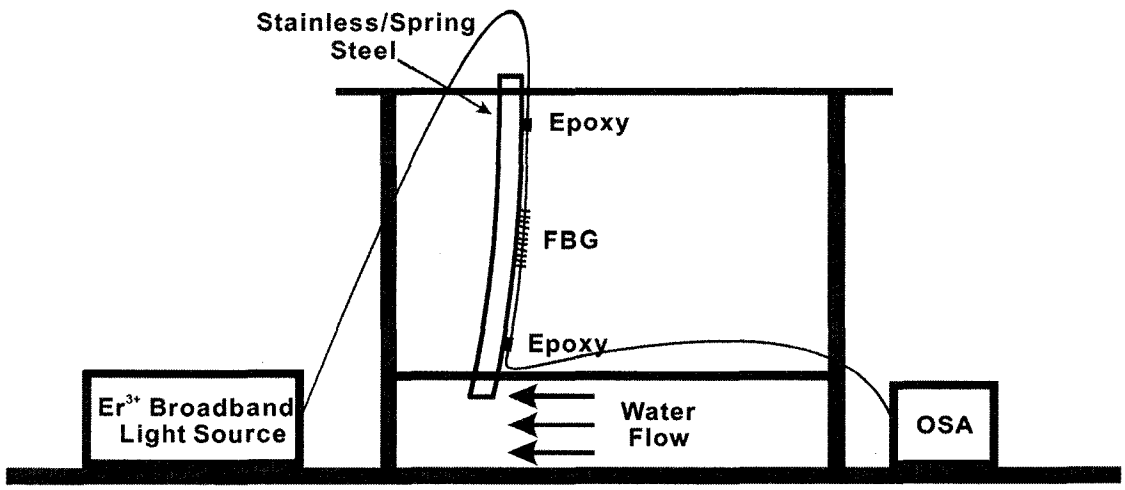

Figure 3-24: Schematic diagram of the water flow measurement system.

In the water flow experiment, we used two different steel-mounted FBG schemes, which were the same as those used in the bending sensing measurement. First we adopted a stainless steel bar-mounted FBG. The schematic diagram of the stainless steel bar-mounted FBG has been shown in Fig. 3-14.

First the water flow hit the stainless steel bar from the same side of the fibre with regard to the stainless steel bar (forward water flow). The water flow was increased from

0 to 90 cm^3/s. At each specific water flow rate, the FBG spectrum was recorded by the OSA. The Bragg wavelength of the FBG as a function of water flow rate is given in Fig. 3-25. This water flow change yields a wavelength shift of approximately 0.077 nm.

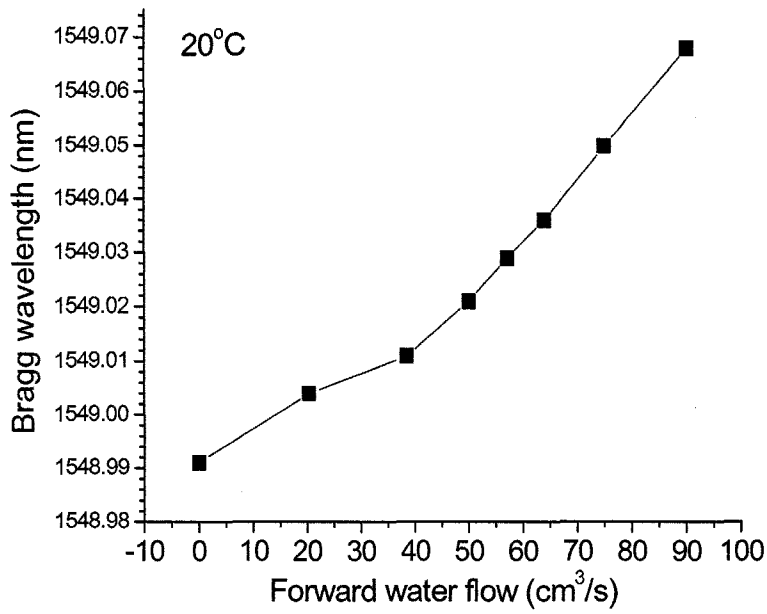

Figure 3-25: Bragg wavelength of the FBG as a function of forward water flow rate at 20 °C.

Figure 3-26 displays the transmission spectra of the FBG when the forward water flow rate was increased. As the water flow rate was increased, the Bragg wavelength was found to shift toward the longer wavelength, which is consistent with the elongation of the FBG caused by the convex bending of the stainless steel bar.

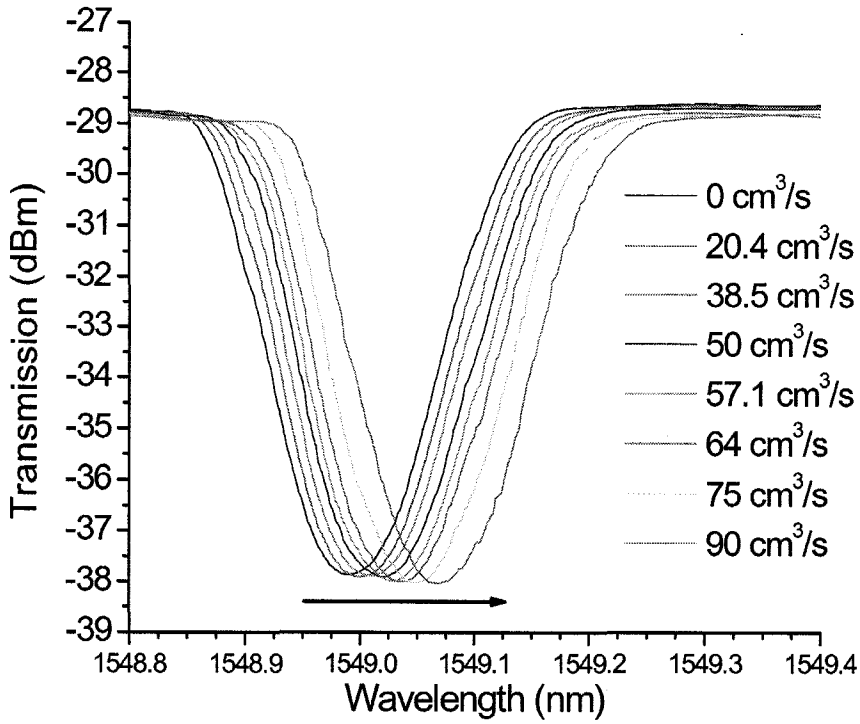

Figure 3-26: Transmission spectra of the FBG under different forward water flow rates.

When the water flow was changed to the opposite direction and the flow rate was increased from 0 to 90 cm^3/s, the FBG spectra were recorded by the OSA. The Bragg wavelength of the FBG as a function of the water flow is shown in Fig. 3-27. This water flow change yields a wavelength shift of approximately 0.027 nm. Figure 3-28 displays blue-shifts of the FBG transmission spectra red-shifts when the backward water flow rate was increased. As the water flow was increased, the wavelength was found to shift toward the shorter wavelength, which is consistent with the shrinkage of the FBG caused by the concave bending of the stainless steel bar.

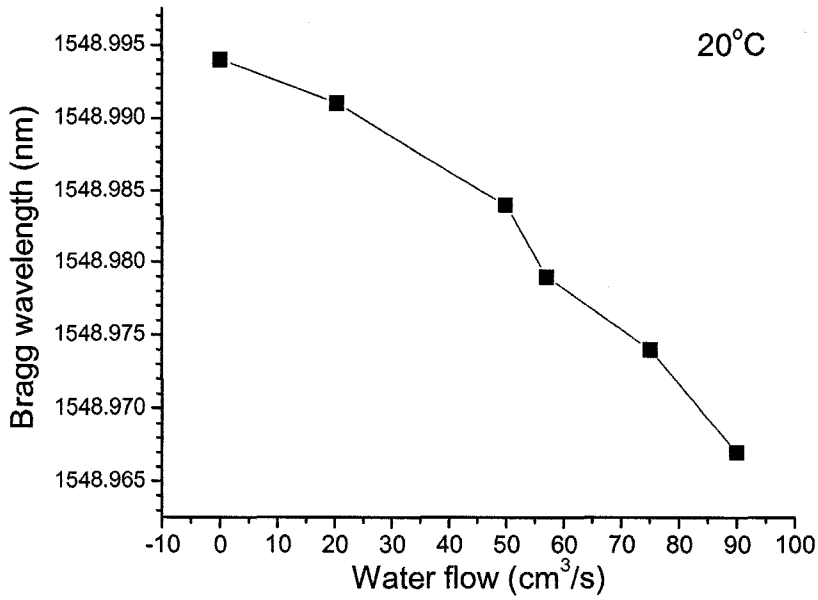

Figure 3-27: Bragg wavelength of the FBG as a function of backward water flow rate at 20 °C.

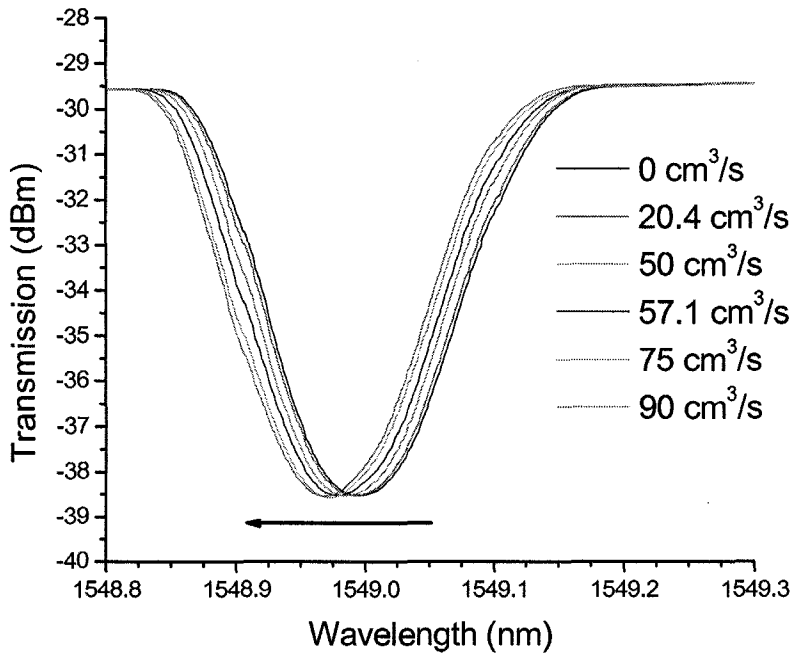

Figure 3-28: Transmission spectra of the FBG under different backward water flow rates.

In order to compare with the results from the bending measurement, the water flow induced shift of the steel bar was recorded. The steel bar shift induced by the water flow and the Bragg wavelength corresponding to the motion stage induced bending effect as a function of water flow is shown in Fig. 3-29. It shows that red-shift of the FBG resonant peaks with respect to the increasing water flow rate is 0.081 nm. The experimental result of a Bragg centre wavelength shift as a function of water flow rate 0.077 nm is in good agreement with the simulation result.

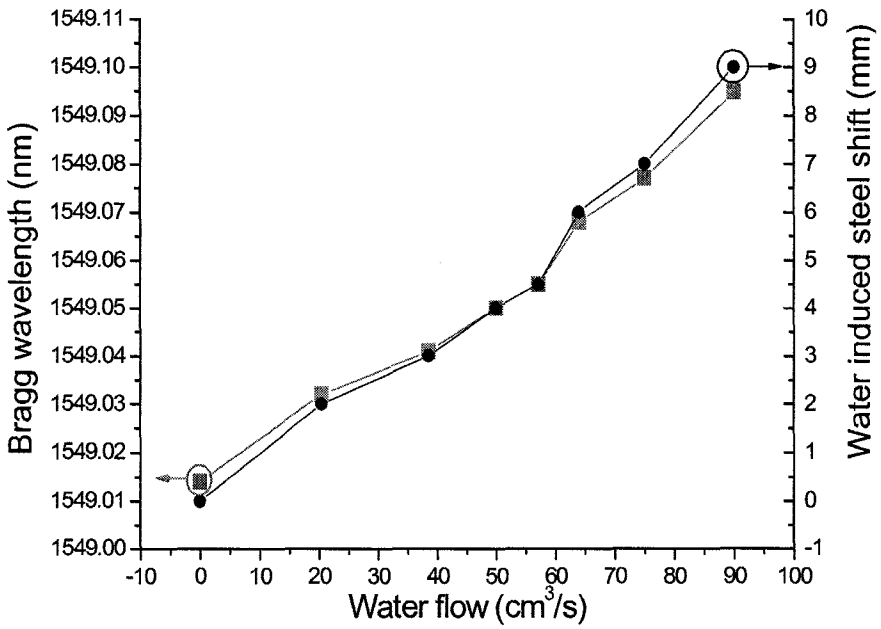

Figure 3-29: The FBG in water flow measurement: ●, bending shifts of the steel bar under different water flow rates; ■, the corresponding Bragg wavelength due to the same amount of bending shift induced by the motion stage.

Figure 3-30 shows the Bragg wavelength of the FBG as a function of the water flow rate, which demonstrates that the stainless steel bar-mounted FBG can realize the sensing of water flow rate and direction simultaneously.

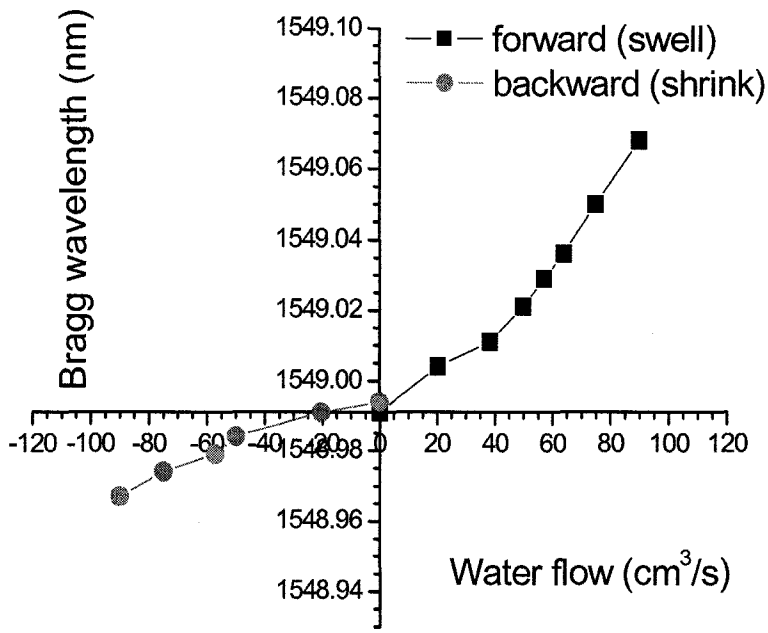

Figure 3-30: Bragg wavelength of the FBG as a function of water flow rate at 20 °C.

For a spring steel bar-mounted FBG as the second scheme to measure the water flow, its schematic diagram has been shown in Fig. 3-19. First the water flow hit the spring steel bar from the same side of the fibre with regard to the spring steel bar (forward water flow). The water flow was increased from 0 to 90 cm^3/s. At each specific water flow rate, the FBG spectrum was recorded by the OSA. The Bragg wavelength as a function of the water flow rate is given in Fig. 3-31. This water flow change yields a wavelength shift of

approximately 0.826 nm. Figure 3-32 displays the transmission spectra of the FBG when the forward water flow rate is increased. As the water flow rate was increased, the Bragg wavelength was found to shift toward the longer wavelength, which is consistent with the elongation of the FBG caused by the convex bending of the spring steel bar.

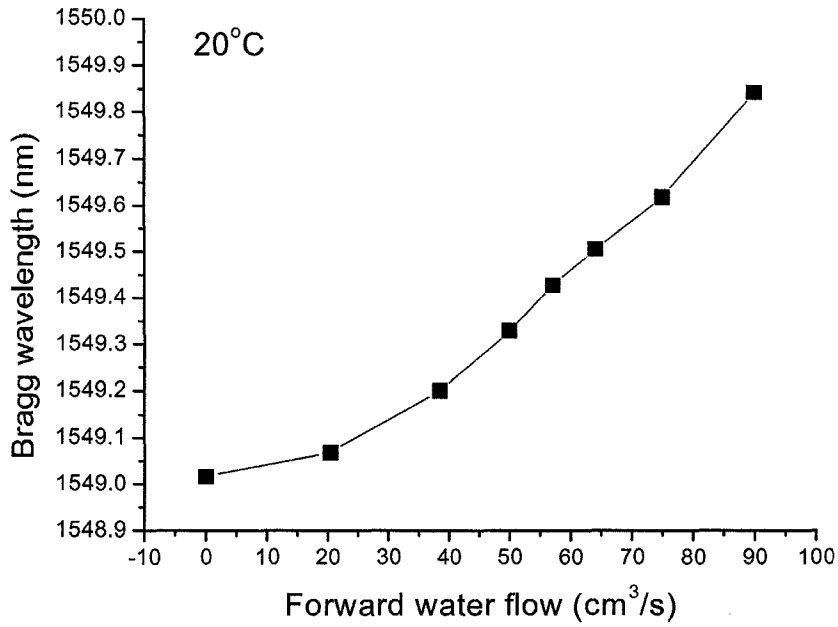

Figure 3-31: Bragg wavelength of the FBG as a function of forward water flow rate at 20 °C.

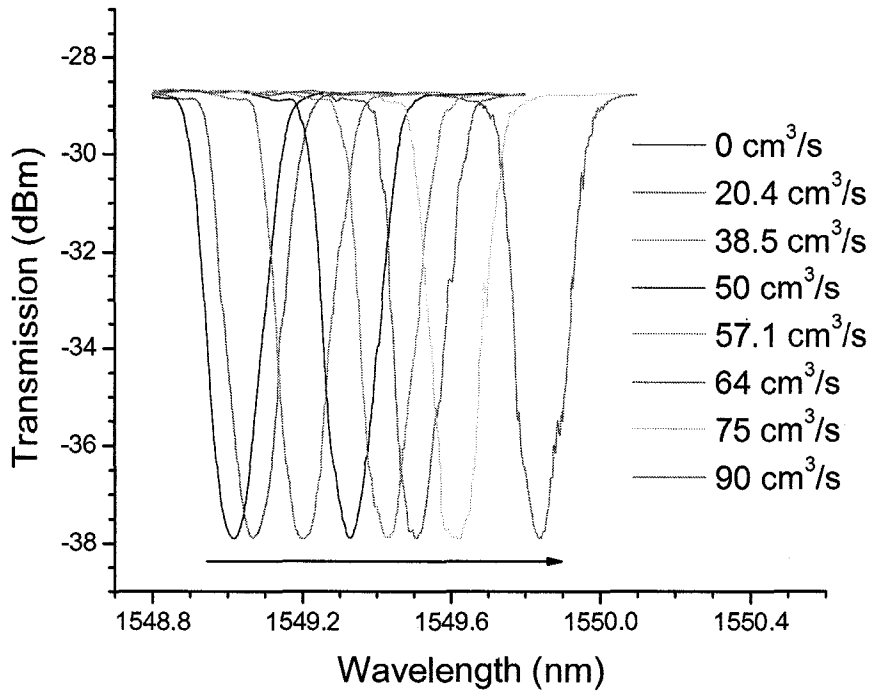

Figure 3-32: Transmission spectra of the FBG under forward water flow.

When the water flow was changed to the opposite direction and the flow rate was increased from 0 to 90 cm^3/s, the FBG spectra were recorded by OSA. The Bragg wavelength of the FBG as a function of water flow rate is shown in Fig. 3-33. When the water flow rate reaches about 20 cm^3/s, the Bragg wavelength will not blue-shift further due to the complete relaxation of the fibre.

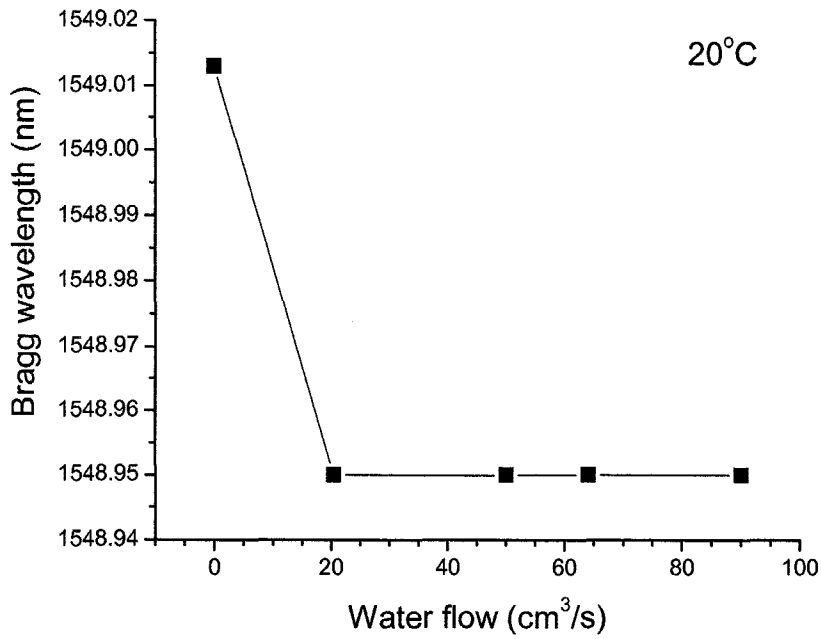

Figure 3-33: Bragg wavelength as a function of backward water flow at 20 °C.

In order to compare with the results from the bending measurement result, the water flow induced shift of the steel bar was recorded. The steel bar shift induced by the water flow and the Bragg wavelength corresponding to the motion stage induced bending effect as a function of water flow is shown in Fig 3-34. It shows that red-shift of the FBG resonant peaks with respect to the increasing water flow rate is 0.698 nm. The experimental result with a value of 0.826 nm indicates a discrepancy from the simulation result, which is believed to result from the unstable water flow from the tap water.

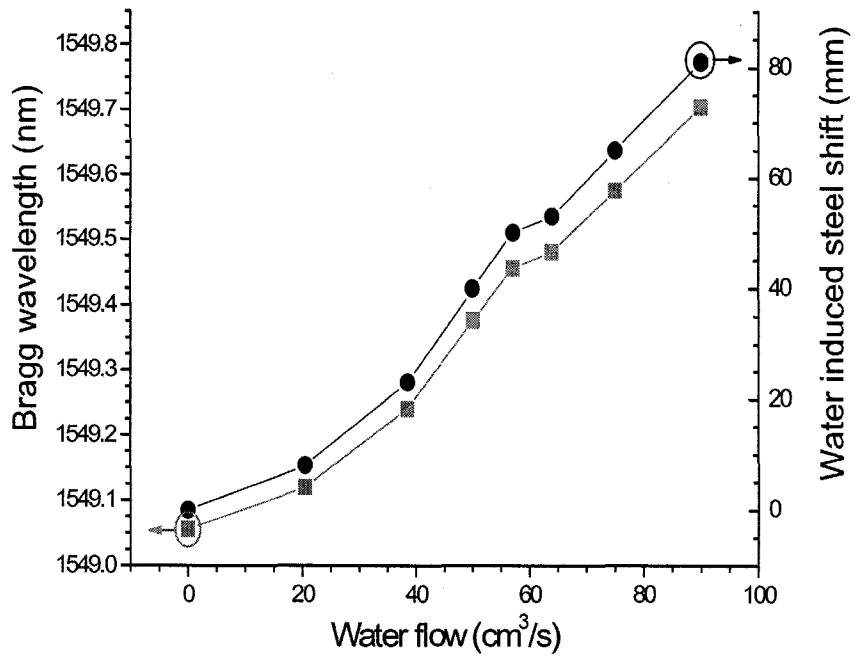

Figure 3-34: The FBG in water flow measurement: •, bending shifts of the steel bar under different water flow rates; ■, the corresponding Bragg wavelength due to the same amount of bending shift induced by the motion stage.

3.6 Conclusion

This chapter reports strain sensitivity of FBGs and its several applications. The axial strain sensitivity was firstly studied, which indicated that the axial strain changes resulted in a linear shift of the Bragg wavelength of the FBGs. Simultaneous measurement of axial strain and temperature was realized using two polymer-coated FBGs, which demonstrated that the dual-wavelengths of the FBGs have different responses to the

temperature and axial strain. This multiplexed FBGs scheme can realize the discrimination between axial strain and temperature effects. Secondly, the bending sensing experiment is reported. The result shows that steel-mounted FBG can be an excellent bending sensor as a shape sensor or a smart structure sensor. Thirdly, the water flow measurement based on the bending sensor was conducted. The steel-mounted FBG can distinguish both the magnitude and the direction of water flow. The advantage of the water flow sensor is its simplicity in the sensing principle and fabrication. Based on the instinctive temperature and strain sensitivity and their unique properties, FBGs have been considered as excellent sensor elements.

Chapter 4

Polarization Characterization of Fibre Bragg Gratings

4.1 Introduction

In chapters 2 and 3, sensing of various measurands by using FBGs have be investigated. In this chapter, a new sensing application based on the polarization characterization of FBGs will be discussed.

The polarization characterization is increasingly important in optical communication systems. The polarization dependent loss (PDL) characteristics of single mode uniform FBGs will be presented first. The PDL in FBGs was measured by applying the polarization scanning method and the Mueller matrix method. The experimental results

indicate that the wavelength dependent PDL in a uniform FBG has the potential to realize temperature sensing measurement. The temperature response of a polarization maintaining FBG was investigated. The Bragg wavelengths corresponding to fast-axis mode and slow-axis mode and their wavelength difference are sensitive to the temperature change. The temperature sensing applications based on the polarization characterization can thus be realized.

4.2 Polarization Dependent Loss of Single Mode Uniform Fibre Bragg Gratings

4.2.1 Theory of Polarization Dependent Loss

Polarization dependent loss is the difference between the minimum and the maximum transmission of an optical component versus all possible input polarization states. Many optical components, such as fibre optical coupler, optical attenuators and optical isolators, exhibit PDL. Single-side irradiation of the fibre by an UV laser through a phase mask during the grating inscription process contributes to the FBG birefringence [108, 109]. The birefringence leads to the polarization dependent loss in the transmission power of FBGs. For applications in telecommunication, PDL in a long distance optical communication system should be as small as possible because the existence of PDL combined with polarization mode dispersion (PMD) causes pulse distortion and

deteriorates system performance. However in the case of sensor networks, PDL may be desirable in some cases, for example, Oh *et al.* demonstrated a new technique to discriminate temperature and strain effects using a single FBG which was based on the Mueller matrix method measurement of the maximum PDL value of the FBG [82].

There are three basic methods to measure PDL: the polarization scanning method, the Jones matrix and the Mueller matrix method. The operation principle of the Mueller matrix method is to generate four specific input polarization states, *i.e.* linear horizontal, linear vertical, linear at 45° and right-hand circular, pass through the FBG and measure the optical power transmission at these four states [110]. The incident polarized light of Stokes vector $\vec{S}_{in}$ interacts with the FBG (Mueller matrix M). The Stokes vector $\vec{S}_{out}$ of the output light, can then be expressed as

$$\vec{S}_{out} = M \cdot \vec{S}_{in} = \begin{bmatrix} m_{11} & m_{12} & m_{13} & m_{14} \\ m_{21} & m_{22} & m_{33} & m_{44} \\ m_{31} & m_{32} & m_{33} & m_{34} \\ m_{41} & m_{42} & m_{43} & m_{44} \end{bmatrix} \begin{bmatrix} S_0 \\ S_1 \\ S_2 \\ S_3 \end{bmatrix}_{in} \tag{4-1}$$

where S_0 is the total intensity, S_1 is the difference in the intensities between the horizontal and vertical linearly polarized components, S_2 is the difference in the intensities between the linearly polarized components oriented at +45° and -45°, S_3 is the difference in the intensities between the right and left circularly polarized components.

The matrix elements of the first row of the Mueller matrix, m_{11}, m_{12}, m_{13} and m_{14} are useful to calculate the PDL value. The maximum and minimum power transmissions

are calculated as

$$T_{\max} = m_{11} + \sqrt{m_{12}^2 + m_{13}^2 + m_{14}^2} \tag{4-2}$$

and

$$T_{\min} = m_{11} - \sqrt{m_{12}^2 + m_{13}^2 + m_{14}^2}\ . \tag{4-3}$$

The PDL can be expressed from its definition:

$$PDL = 10\log_{10}\left(T_{\max} / T_{\min}\right) \tag{4-4}$$

where $T_{\max}$ and $T_{\min}$ denote the maximum and minimum transmission powers through the FBG, respectively.

The polarization scanning method measures the maximum and minimum changes in the power transmission through the FBG over all possible input polarization states. The PDL of the FBG is then obtained from the Eqn. (4-4).

Birefringence in optical fibres is the difference in refractive index Δn between a particular pair of orthogonal polarization modes (x and y modes). Their refractive index is defined by Eqn. (4-5) where n_{eff} is the core effective refractive index given by:

$$n_{eff,x} = n_{eff} + \frac{\Delta n}{2};\ n_{eff,y} = n_{eff} - \frac{\Delta n}{2}. \tag{4-5}$$

The x and y modes undergo different couplings due to Δn. The transmitted signal is thus the combination of the signals corresponding to the x and y modes.

The Jones vector corresponding to the transmitted signal is defined by [111]:

$$\begin{pmatrix} E_{t,x} \\ E_{t,y} \end{pmatrix} = J \cdot \begin{pmatrix} E_{i,x} \\ E_{i,y} \end{pmatrix} = \begin{bmatrix} \rho_x & 0 \\ 0 & \rho_y \end{bmatrix} \begin{pmatrix} E_{i,x} \\ E_{i,y} \end{pmatrix} = \begin{pmatrix} \rho_x E_{i,x} \\ \rho_y E_{i,y} \end{pmatrix} \tag{4-6}$$

where $\begin{pmatrix} E_{i,x} \\ E_{i,y} \end{pmatrix}$ is the Jones vector of the input signal and $\rho_{x(y)}$ denotes the transmission coefficient of the uniform FBG corresponding to the $x(y)$ mode. The expression of $\rho_{x(y)}$ can be derived from the coupled mode theory [53]:

$$\rho_{x(y)} = \frac{-k_{x(y)} \sinh\left(\sqrt{k_{x(y)}^2 - \sigma^2} L\right)}{\sigma_{x(y)} \sinh\left(\sqrt{k_{x(y)}^2 - \sigma_{x(y)}^2} L\right) + i\sqrt{k_{x(y)}^2 - \sigma_{x(y)}^2} \cosh\left(\sqrt{k_{x(y)}^2 - \sigma_{x(y)}^2} L\right)} \quad (4\text{-}7)$$

and

$$R_{x(y)} = \left|\rho_{x(y)}\right|^2 . \quad (4\text{-}8)$$

Thus the PDL in a FBG is given by:

$$PDL = 10\log_{10}\left(R_x / R_y\right). \quad (4\text{-}9)$$

4.2.2 Polarization Dependent Loss Measurement

The measurement setup for the transmission spectrum and the PDL of polyimide-coated FBG is shown in Fig. 4-1. The polarization scanning method and the Mueller matrix method were adopted in this experiment. The transmission spectrum and the PDL were measured using a tunable laser (TUNICS-PR, Photonetics), a polarization controller (HP 11896) and a power meter. The LabVIEW front panels of the PDL measurement we designed by using the polarization scanning method are shown in Fig. 4-2. For the polarization scanning method, the fibre-coil-based polarization controller generates polarization states in a pseudo-random manner. The power meter records maximum and

minimum transmissions by a personal computer through LabVIEW control. For the Mueller matrix method, the polarization controller (PS3 PDL-multimeter, JDS Uniphase) comprises a polarizer, a quarter-wave plate and a half-wave plate which can synthesize the four specific polarization states. The LabVIEW front panels of PDL measurement we designed by using the Mueller matrix method are shown in Fig. 4-3. The FBG was immersed in a microprocessor-controlled water bath in which the temperature was changed from 25 °C to 45 °C.

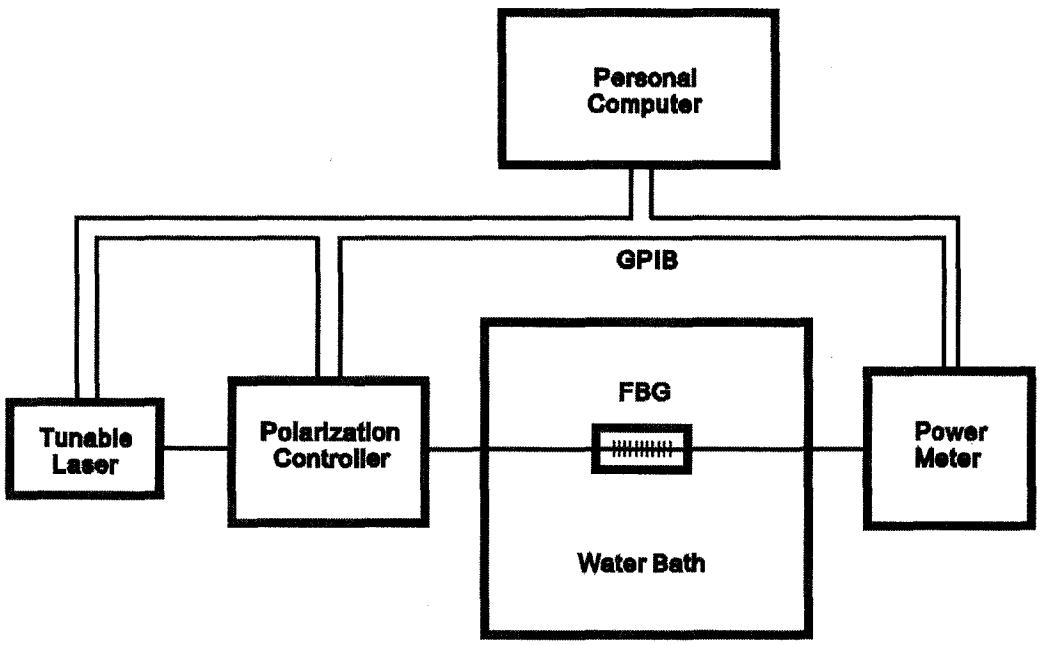

Figure 4-1: Schematic diagram of PDL measurement system.

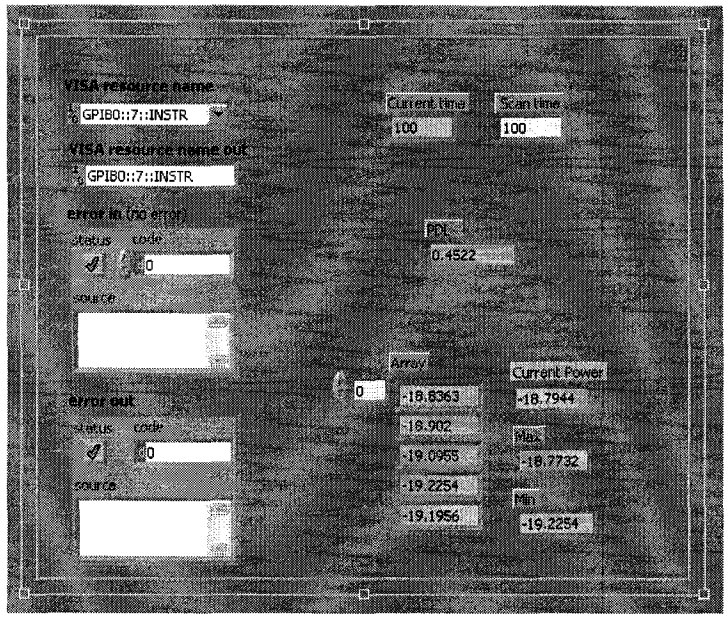

Figure 4-2: LabVIEW front panel of the polarization scanning method.

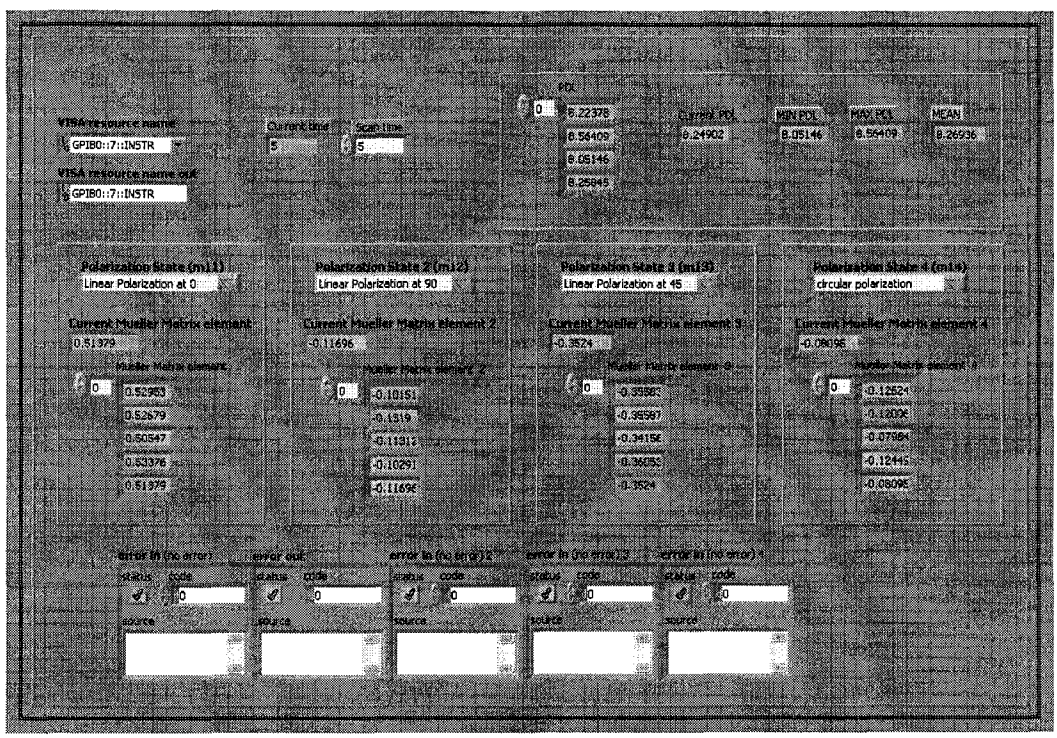

Figure 4-3: LabVIEW front panel of the Mueller matrix method.

4.2.3 Temperature Sensing Application of Polarization Dependent Loss

For the PDL polarization scanning measurement, two transmission spectra of a FBG were obtained as show in Fig. 4-4: one corresponds to the maximum transmission power T_{max} and the other one corresponding to the minimum transmission power T_{min}. These two signals represent x and y modes or fast and slow axis modes and the PDL can be calculated from Eqn. (4-4). The transmission spectrum and the PDL of a FBG for the temperature in the range of 25 to 45 °C have been measured and shown in Fig. 4-5. There are two PDL peaks and one pit in the PDL evolution spectrum. As the temperature increased from 25 to 45 °C, the PDL increased from 8.3 to 11.4 dB (inset of Fig. 4-5). The results indicate that the maximum PDL increases due to the enhanced birefringence as the temperature increases. Thus we can measure the maximum PDL of a FBG and reveal the corresponding temperature around the FBG. In addition, the wavelength of the first PDL MAX, second PDL MAX, MIN transmission and MAX transmission also linearly increase with the increasing temperature because the PDL spectrum and FBG transmission spectrum red shifte with the increasing temperature. The temperature sensitivities of these parameters are 0.01, 0.0113, 0.0112 and 0.0115 nm/°C, respectively (Fig. 4-6).

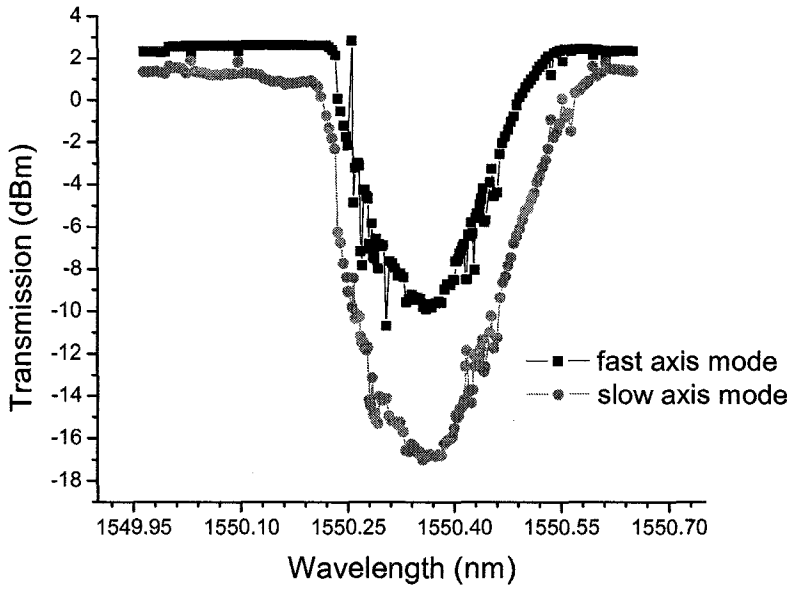

Figure 4-4: Transmission spectra of the fast and slow axis modes.

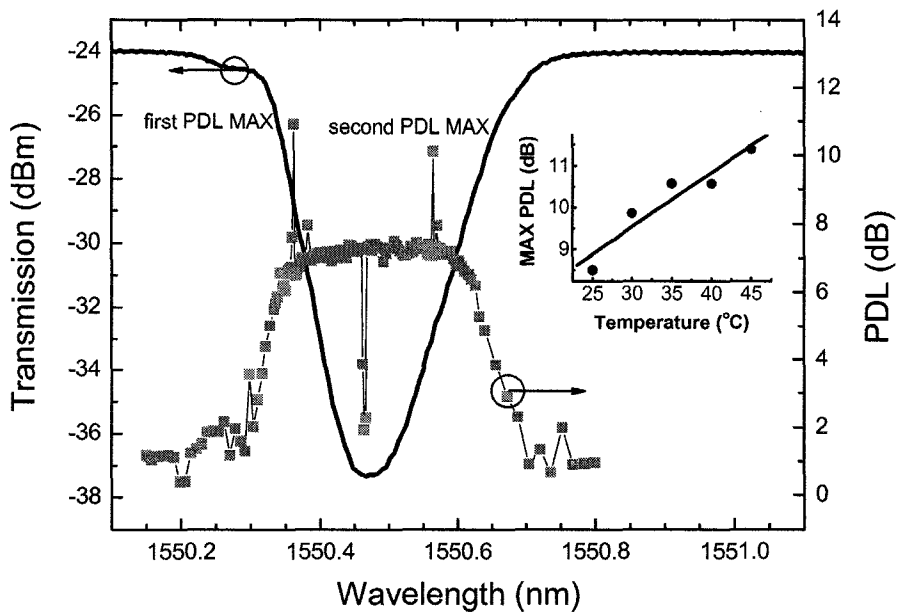

Figure 4-5: Experimental results of the transmission and PDL of the FBG obtained from the polarization scanning method at 30 °C. Inset: dependence of the maximum PDL on the temperature.

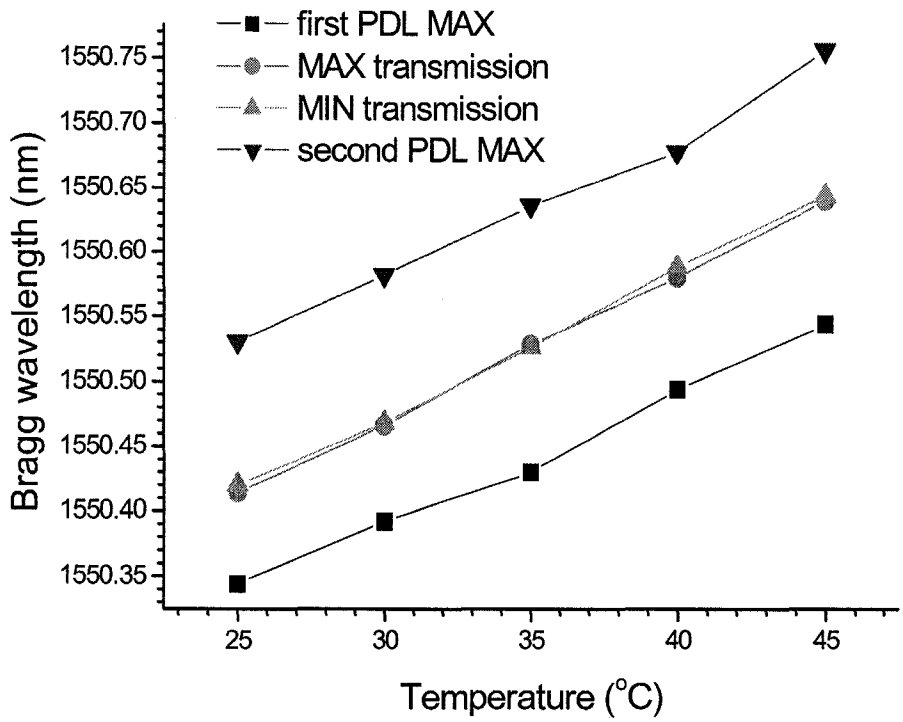

Figure 4-6: Bragg wavelengths of the first PDL MAX, second PDL MAX, MIN transmission, and MAX transmission as a function of increasing temperature.

For the Mueller matrix method, the experimental results are shown in Fig. 4-7. The corresponding wavelengths of the first and second PDL maximum linearly increase with the increasing temperature. The temperature sensitivities of these two Bragg wavelengths are 0.0128 nm/°C and 0.01 nm/°C, respectively.

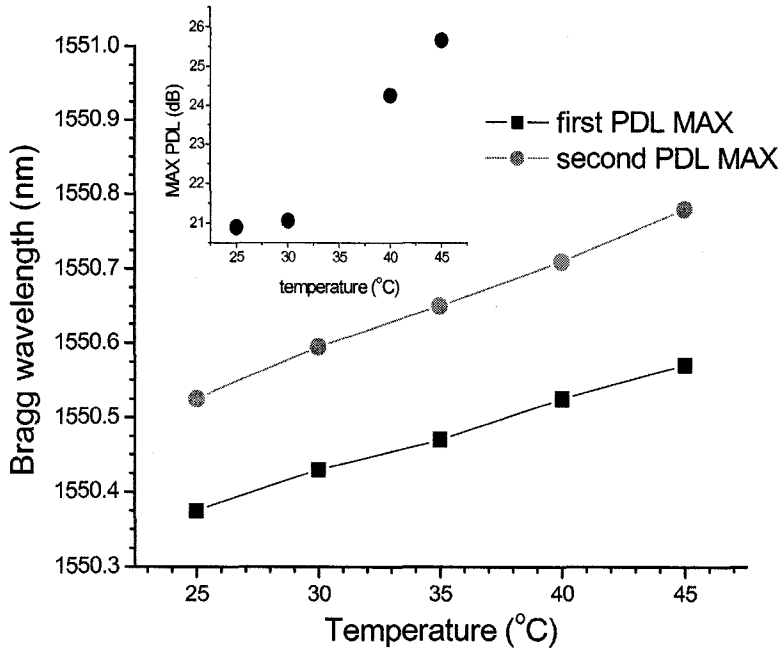

Figure 4-7: Dependence of the maximum PDL and corresponding wavelength on temperature.

Given enough scanning time, the polarization scanning method is more practical due to its simple scheme. Compared with the polarization scanning method, the Mueller matrix method is less time-consuming, which is suitable to perform wavelength dependent PDL measurements.

In order to compare the PDL evolutions observed from experiments, the physical parameters of the measured FBG were numerically reconstructed using the mathematical model of FBG discussed in section 1-3. Figure 4-8 simulates the numerically reconstructed evolutions for a uniform FBG of which the physical parameters are: $l = 1$ cm, $\Lambda = 528$ nm, $\delta n = 1.0 \times 10^{-4}$ and $\Delta n = 4 \times 10^{-6}$. A good agreement between experimental and simulated evolutions is obtained.

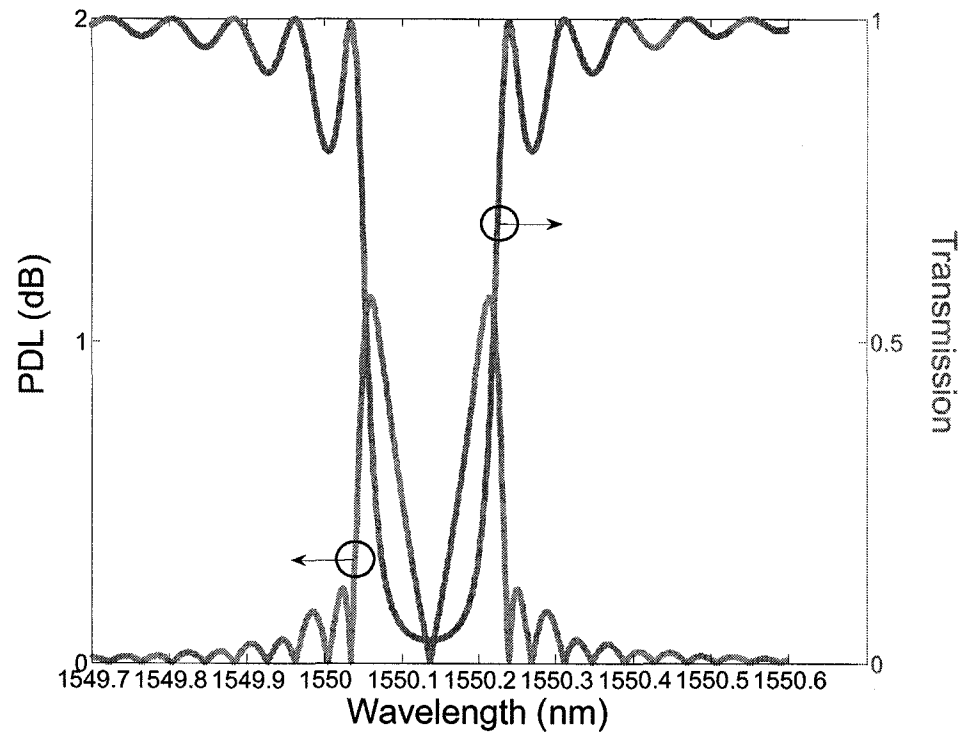

Figure 4-8: Simulation results of the transmission and PDL of the FBG.

4.3 Polarization Characterization of Polarization Maintaining Fibre Bragg Gratings

4.3.1 Polarization Maintaining Fibre Bragg Grating

A polarization maintaining (PM) optical fibre is an optical fibre in which the polarization planes of light waves launched into the fibre are maintained during propagation with little or no cross-coupling of optical power between the polarization modes. A typical PM fibre, polarization-maintaining and absorption reducing fibre (PANDA), has been used in this

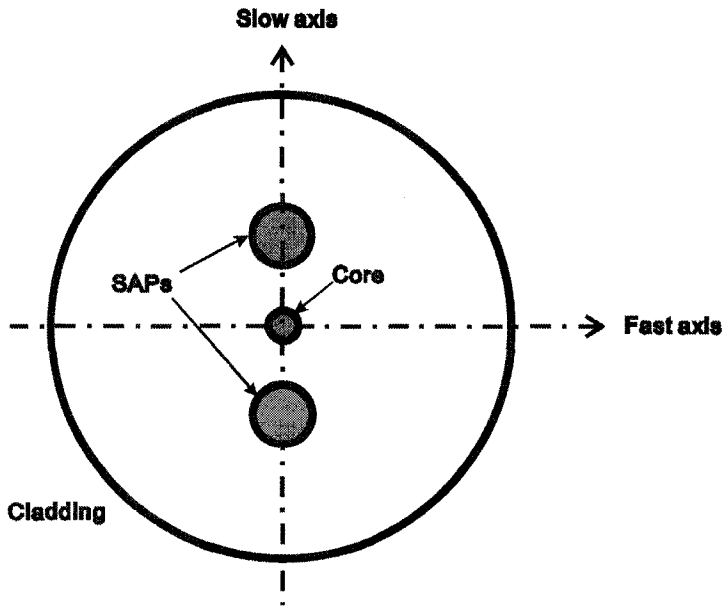

Figure 4-9: Cross section of a PANDA fibre.

temperature sensing experiment. Figure 4-9 shows the cross section of a PANDA fibre.

The core is in the centre of the fibre cross section. There are two stress applying parts (SAPs) on either side of the core to induce polarization. The two SAPs and the core comprise the slow axis and the orthogonal direction can be considered as the fast axis.

When a grating is inscribed in a PM fibre, because of the slight difference in the effective refractive indices of the two orthogonal polarization modes, there will be two reflective peaks at slightly different wavelengths. Their Bragg wavelengths can be written as

$$\lambda_F = 2n_F \cdot \Lambda \tag{4-10}$$

$$\lambda_S = 2n_S \cdot \Lambda \tag{4-11}$$

where λ_F (λ_S) and n_F (n_S) are the Bragg wavelength and the effective refractive

index corresponding to the fast-axis (slow-axis) mode, respectively. Λ is the period of grating.

4.3.2 Temperature Measurement Using a Polarization Maintaining Fibre Bragg Grating

Figure 4-10 illustrates the setup used to measure the temperature performance using a PM FBG. Light from the Er^{3+} broadband light source was launched into one end of the fibre containing the grating via an in-line fibre polarizer and a polarization controller (HP 11896). The in-line fibre polarizer produced linearly polarized light. The transmission spectrum was measured by the optical spectrum analyzer. The PM FBG was placed in the water bath where the temperature was precisely controlled.

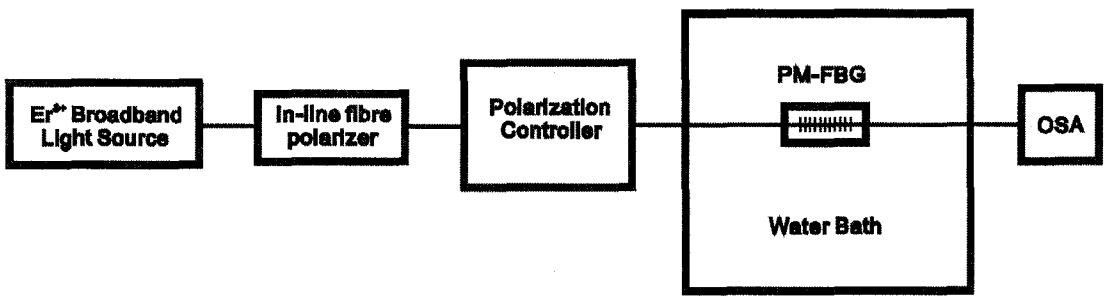

Figure 4-10: Schematic diagram of temperature sensing measurement system using a PM FBG.

4.3.3 Temperature Sensitivity of Polarization Maintaining Fibre Bragg Grating

Figure 4-11 gives the transmission spectrum of the PM FBG at room temperature in which the left Bragg wavelength corresponds to the fast-axis mode and the right one for the slow-axis mode.

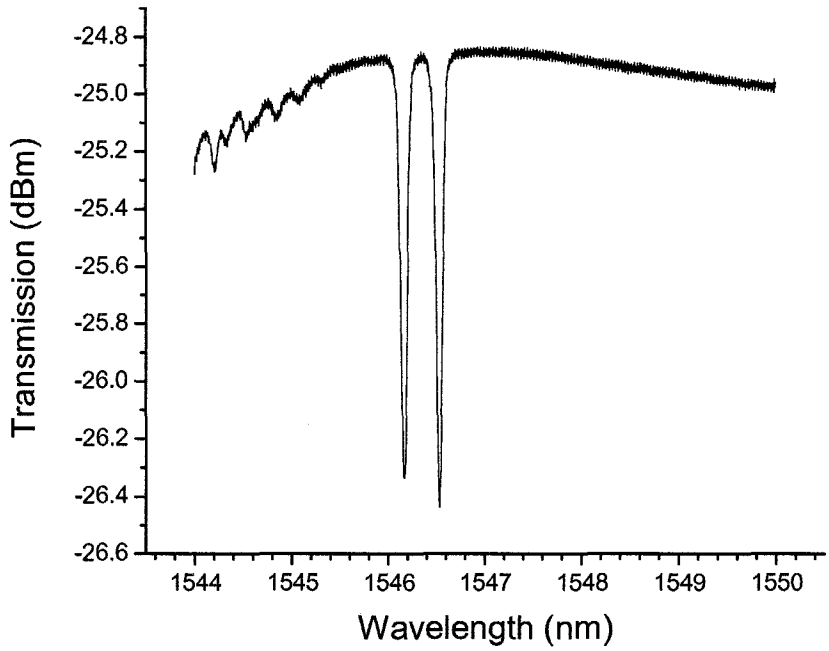

Figure 4-11: Transmission spectrum of the PM FBG at room temperature.

The physical parameters of PM FBG have been numerically reconstructed by using the mathematical model of FBGs. Figure 4-12 shows the simulation results of the transmission spectrum of the PM FBG. A good agreement between the experimental and the simulated evolutions is obtained.

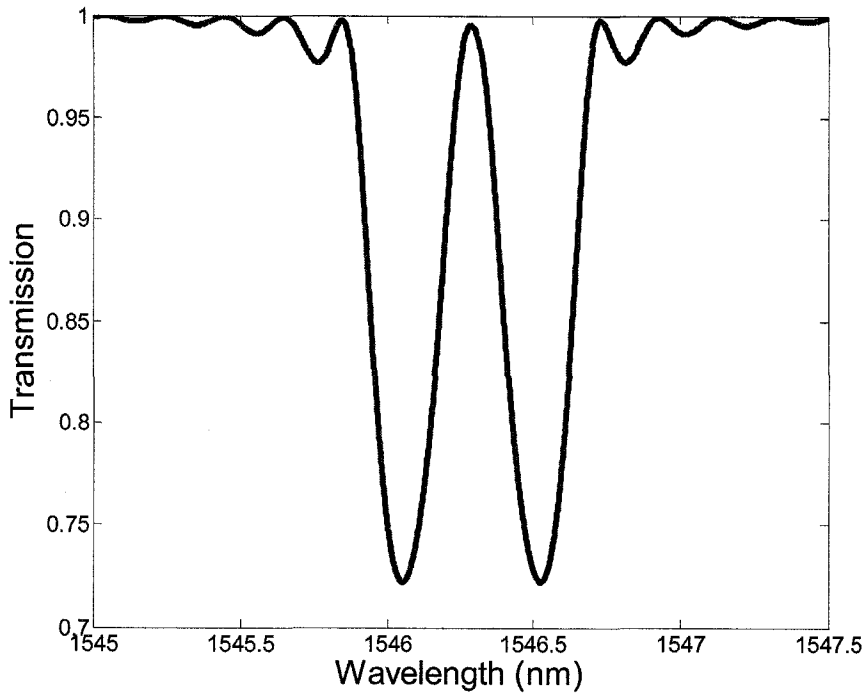

Figure 4-12: Simulation results of the transmission spectrum of the PM FBG.

When the unpolarized light launched into one end of the in-line fibre polarizer, linearly polarized light was output from the other end. The state of polarization in fibre could be adjusted using the polarization controller to achieve a rotation of 180° with an interval of 1.62°. Figure 4-13 shows that the Bragg wavelengths corresponding to the fast-axis and slow-axis modes do not shift with the changing state of polarization at 25°C. The Bragg wavelengths corresponding to the fast-axis and slow-axis modes are 1546.102 ± 0.008 nm and 1546.476 ± 0.008 nm for all the states of polarization during the polarization scanning process. However the transmission powers at these two Bragg wavelengths fluctuate from -29.09 dBm to -33.35 dBm due to the change of the state of polarization.

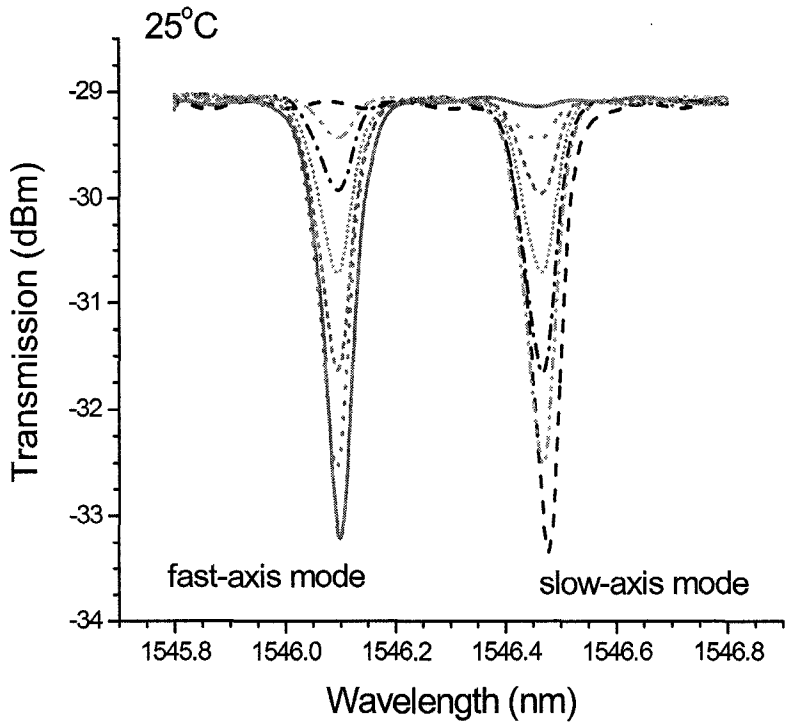

Figure 4-13: Transmission spectra of PM FBG at different states of polarization.

The temperature in the water bath was changed from 25 to 65 °C in steps of 10 °C and sufficient time was allowed to ensure that the system reached thermal equilibrium at each specific temperature. During the temperature changing process, the change of Bragg grating wavelength as a function of increasing temperature is shown in Fig. 4-14. The two Bragg wavelengths red-shift linearly with the temperature increased, however, their difference decreases (Fig. 4-15). The temperature sensitivities of these two Bragg wavelengths, corresponding to the fast-axis mode and the slow-axis mode, are 0.01048 and 0.00983 nm/°C, respectively. The Bragg wavelength difference between the fast-axis mode and the slow-axis mode is decreased by 0.0159 nm.

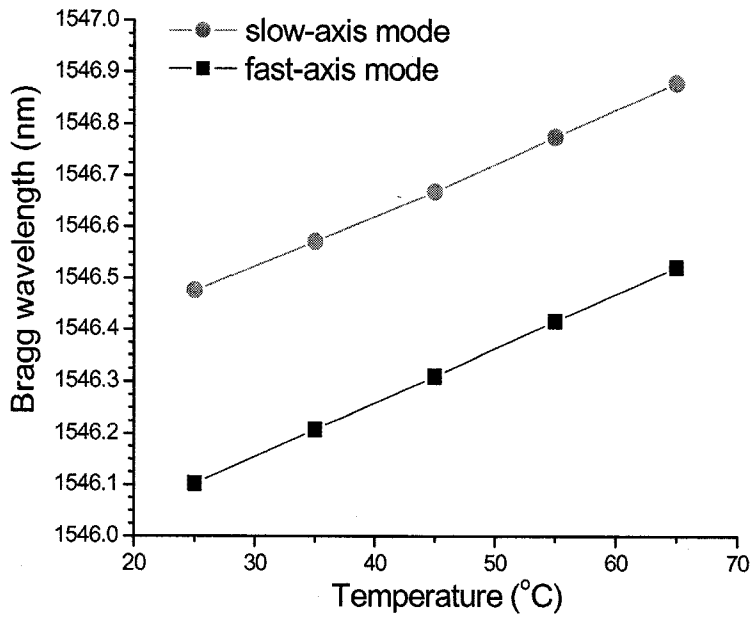

Figure 4-14: Bragg wavelengths of the slow-axis and the fast-axis modes as a function of the increasing temperature.

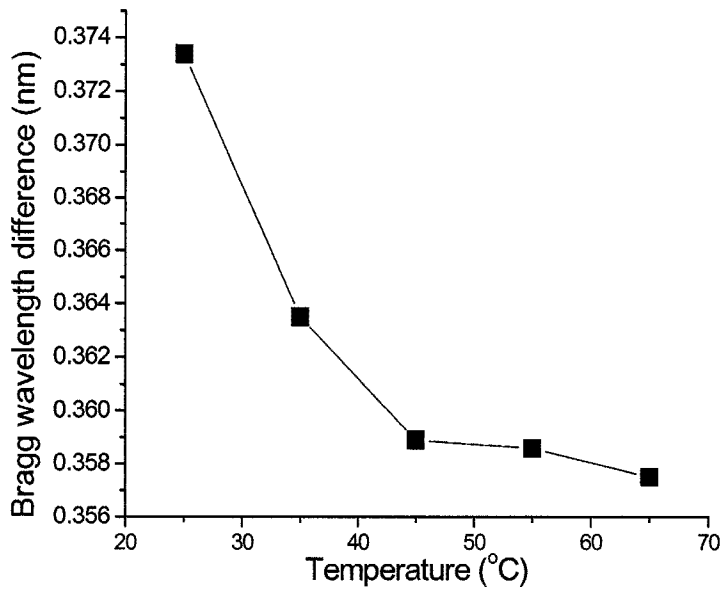

Figure 4-15: Dependence of the difference in the Bragg wavelengths of the fast-axis and slow-axis modes of the PM FBG on temperature.

The birefringence B in a PM FBG can be written as

$$B = n_S - n_F . \tag{4-12}$$

Modal birefringence B is also given by [112]

$$B = B_G + B_{So} + B_S \tag{4-13}$$

where B_G is the geometrical component, B_{So} is the self-stress component, and B_S is the outer stress-component.

In the PANDA fibre the modal birefringence components B_G and B_{So} are zero. B_S can be expressed as [112]

$$B_S = \varepsilon_c B_m = \left(1 - \frac{A_y}{A_x}\right) \frac{\alpha_T (T_S - T) n_1^3 (P_{11} - P_{12})(1+\upsilon)}{4(1-\upsilon^2)} \tag{4-14}$$

where T_S is the softening temperature of the optical fibre core (about 690 °C [112]) and T is the temperature around the fibre; the other parameters are all constant [112].

From Eqns. (4-10), (4-11), (4-12) and (4-14), we obtain

$$\lambda_S - \lambda_F = C \cdot (T_S - T) . \tag{4-15}$$

In this experiment, the temperature around the fibre was increased from 25 to 65 °C which is lower than the softening temperature of the optical fibre core. This process caused a decrease in the difference between the environmental temperature and softening temperature. Thus the Bragg wavelength difference of the slow-axis and fast-axis modes will decrease with the increasing temperature.

4.4 Conclusion

In the first part of this chapter, polarization dependent loss of a single mode uniform FBG has been investigated using the polarization scanning method and the Mueller matrix method. The birefringence caused by the single-side irradiation of the fibre by an UV laser during the grating inscription process leads to PDL in the transmission power. The simulation of the transmission spectrum and PDL based on the coupled mode theory and Jones formalism shows good agreement with the experimental results. It is demonstrated that the maximum PDL and the corresponding wavelength will increase with the increase of temperature. The results indicate that PDL measurement is an effective method to achieve temperature sensing.

In the second part of this chapter, the temperature response of a polarization maintaining FBG has been investigated. Both of the Bragg wavelengths corresponding to the fast-axis and the slow-axis modes red shift with the rising temperature while the Bragg wavelength difference of these two modes decreases with the rising temperature.

Chapter 5

Discussion and Conclusion

5.1 Summary of the Results and Contributions

Fibre Bragg Gratings have been demonstrated as useful fibre optic devices for a range of sensing applications including temperature, strain and other physical quantities. In this thesis, the basic properties, mathematical models and sensing applications of FBGs have been reviewed. The experimental results indicate that the temperature changes in different environmental conditions will result in a linear shift of the Bragg resonant wavelength. The polyimide-coated FBG is sensitive to the humidity change while the acrylate-coated FBG not. The schemes for simultaneous measurement of temperature and saccharinity/salinity have been introduced. It is shown that the axial strain changes will result in a linear shift of the Bragg resonant wavelength of the FBGs. Simultaneous

measurement of axial strain and temperature has been realized using two polymer-coated FBGs. The bending sensing experiment showed that FBG sensor can be used as a shape sensor or smart structure sensor. The water flow measurement based on the bending sensor indicated that FBG can distinguish both the magnitude and the direction of water flow. The polarization characterizations of FBGs have also been investigated. In the polarization scanning method and the Mueller matrix method were used to measure the PDL of a uniform single mode FBG. The birefringence caused by the single-side irradiation of the fibre by an UV laser during the grating inscription process leads to the PDL in the transmission power. It is demonstrated that the maximum PDL and the corresponding wavelength increase with the increase of temperature. For the temperature response of a polarization maintaining FBG, the Bragg wavelengths corresponding to the fast-axis and the slow-axis modes red-shift with the rising temperature. The Bragg wavelength difference of these two modes decreases with the rising temperature. The sensing applications based on the polarization characterization of FBG have been successfully demonstrated.

Part of the results in this thesis has been reported or submitted to the following journals and conferences. Several journal submissions are currently in preparation.

1. Ping Lu and Qiying Chen, "In-situ saccharinity and temperature monitoring with a multiplexed fibre Bragg grating sensor system", submitted to IEEE Sensor Journal.

2. Ping Lu and Qiying Chen, "A fibre optic sensor for simultaneous temperature and saccharinity measurement", Advanced Environmental, Chemical, and Biological Sensing

Technologies V, Optics East 2007, Sept. 9-12, 2007, Boston, MA, USA.

3. Qiying Chen, Ping Lu, and Liqiu Men, "Simultaneous temperature and salinity monitoring with a fibre optic sensor", Chemical and Biological Sensors for Industrial and Environmental Monitoring III, Optics East 2007, Sept. 9-12, 2007, Boston, MA, USA.

4. Qiying Chen, Ping Lu, and Liqiu Men, "Fibre-optic sensor probing with a thermoreversible film", Sensors for Harsh Environments III, Optics East 2007, Sept. 9-12, 2007, Boston, MA, USA.

5. Ping Lu and Qiying Chen, "Polarization-dependent loss of fibre Bragg gratings and sensing applications", Photonics North 2007, June 3-7, 2007, Ottawa, Ontario, Canada, Proc. SPIE, 2007, in press.

6. Liqiu Men, Ping Lu, and Qiying Chen, "A fibre-optic temperature sensor with a thermo-reversible compound as a transducer", Photonics North 2007, June 3-7, 2007, Ottawa, Ontario, Canada, Proc. SPIE, 2007, in press.

7. Qiying Chen, Ping Lu, and Liqiu Men, "Photosensitivity of optical fibre gratings and sensing applications", Optical Components and Materials IV, Photonics West 2007, Jan. 20-25, 2007, San Jose, California, USA, Proc. SPIE, 2007, 6469, 6469-31.

5.2 Future Work

This thesis has studied the sensing applications of FBGs. Additional work in this field can be carried out in the following aspects:

1. Further investigation on the dependence of the relative humidity (saccharinity/salinity) sensitivity on the polyimide-coating thickness of FBG is needed. Different thickness of the polyimide coating may have different diffusion process, which will result in different response of the fibre grating. In addition, the equilibrium processes under different thickness of the polyimide-coating will also be different.

2. Simultaneous measurement of multi-direction strain using one single mode FBG can be investigated further. In this thesis, only strain along one direction has been studied. Further investigation on multi-direction, for example, transverse, and the discrimination of strain along different directions will be very important from the point of view of practical applications.

3. Further study of the polarization characterization of different kinds of SM FBG and PM FBG is necessary, including quantitatively determination of polarization dependent loss in FBG, discrimination between strain and temperature effect on FBG using polarization properties, and polarization mode dispersion in FBGs.

References

[1] K. O. Hill, Y. Fujii, D. C. Johnson, and B. S. Kawasaki, *Applied Physics Letters* **1978**, 32, 647-649.

[2] G. Meltz, W. W. Morey, and W. H. Glenn, *Optics Letters* **1989**, 14, 823-825.

[3] L. Reekie, R. Mears, S. Poole, and D. Payne, *Journal of Lightwave Technology* **1986**, 4, 956-960.

[4] V. Mizrahi, D.J. DiGiovanni, R.M. Atkins, S.G. Grubb, Yong-Kwan Park, and J.-M.P. Delavaux, *Journal of Lightwave Technology* **1993**, 11, 2021-2025.

[5] E. M. Dianov, A. A. Abramov, M. M. Bubnov, A. V. Shipulin, A. M. Prokhorov, S. L. Semjonov, A. G. Schebunjaev, G. G. Devjatykh, A. N. Guryanov and V. F. Khopin, *Optical Fibre Technology* **1995**, 1, 236-238.

[6] K. O. Hill, D.C. Johnson, F. Bilodeau, and S. Faucher, *Electronics Letters* **1987**, 23, 464-465.

[7] F. Bilodeau, K. O. Hill, B. Malo, D. C. Johnson, and J. Albert, *IEEE Photonics Technology Letters* **1994**, 6, 80-82.

[8] D.C. Johnson, K.O. Hill, F. Bilodeau, and S. Faucher, *Electronics Letters* **1987**, 23, 668-669.

[9] T.J. Cullen, H.N. Rourke, C.P. Chew, S.R. Baker, T. Bricheno, K.C. Byron and A. Fielding, *Electronics Letters* **1994**, 30, 2160-2161.

[10] F. Bilodeau, D.C. Johnson, S. Thenault, B. Malo, J. Albert, and K.O. Hill, *IEEE Photonics Technology Letters* **1995**, 7, 388-390.

[11] L. Dong, P. Hua, T. A. Birks, L. Reekie, and P. St. J. Russell, *IEEE Photonics Technology Letters* **1996**, 8, 1656-1658.

[12] H. G. Winful, *Applied Physics Letters* **1985**, 46, 527-529.

[13] P.M. Cavaleiro, F.M. Araujo, L.A. Ferreira, J.L. Santos, and F. Farahi, *IEEE Photonics Technology Letters* **1999**, 11, 1635-1637.

[14] Chunn-Yenn Lin, L. A. Wang, IEEE, and Gia-Wei Chern, *Journal of Lightwave Technology* **2001**, 19, 1159-1168.

[15] Chun-Liu Zhao, Xiufeng Yang, M. S. Demokan, and W. Jin, *Journal of Lightwave Technology* **2006**, 24, 879-883.

[16] M. G. Xu, L. Reekie, Y. T. Chow and J. P. Dakin, *Electronics Letters* **1993**, 29, 389-399.

[17] Y. Zhao, Qing-yao Meng, and K. Chen, *Sensors and Actuators A* **2006**, 126, 112-116.

[18] R. Falciai, A.G. Mignani, and A. Vannini, *Sensors and Actuators B* **2001**, 74, 74-77.

[19] D. K. W. Lam, and Brian K. Garside, *Applied Optics* **1981**, 20, 440-445.

[20] V. Mizrahi, and J. E. Sipe, *IEEE Journal of lightwave Technology* **1993**, 11, 1513-1517.

[21] T. Erdogan, and J. E. Sipe, *Journal of the Optical Society of America A* **1996**, 13, 296-313.

[22] B. S. Kawasaki, K. O. Hill, D. C. Johnson, and Y. Fujii, *Optics Letters* **1978**, 3, 66–68.

[23] R. M.Atkins, and V. Mizrahi, *Electron Letters* **1992**. 28, 1743-1744.

[24] D.P. Hand, and P.St. J. Russell, *Optical Letters* **1990**, 15, 102-104.

[25] J.P Bernandin, and N. M. Lawandy, *Optical Communication* **1990**, 79, 194-199.

[26] M.Douay, W.X.Xie, T.Taunay, P.Bernage, P.Niay, P.Cordier, B. Poumellec, L.Dong, J.F.Bayon, H. Poignant, and E. Delevaque, *IEEE Journal of Lightwave Technology* **1997**. 15, 1329-1342.

[27] P.Y.Fonjallaz, H.G. Limberge, R.P.Salathe, F.Cochet, and B.Leuenberger, *Optics Letters* **1995**, 20, 1346-1348.

[28] N.H. Ky, H.G.Limberge, R.P.Salathe, F.Cochet, and L.Dong, *Physics Letters* **1999**, 74, 516-518.

[29] H. G. Limberge, P. Y. Fonjallaz, R. P. Salathe, and F. Cochet, *Applied Physics Letters* **1996**, 68, 3069-3071.

[30] P. J. Lemaire, R. M. Atkins, V. Mizrahi, and W. A. Reed, *Electron Letters* **1993,** 29, pp.1191.

[31] R. M. Atkins, P. J. Lemaire, T. Erdogan, and V. Mizrahi, *Electron Letters* **1993,** 29, pp.1234.

[32] K. Awazu, H. Kawazoe, and M. Yamane, *Journal of Applied Physics* **1990**, 68, pp.2713.

[33] F. Bilodeau, B. Malo, J. Albert, D. C. Johnson, and K. O. Hill, *Optics Letters* **1993,** 18, pp.953.

[34] D. L. Williams, B. J. Ainslie, R. Armitage, R. Kashyap, and R. Campbell, *Electron Letters* **1993**,.29, pp.45.

[35] D. L. Williams, B. J. Ainslie, R. Kashyap, G. D. Maxwell, J. R. Armitage, R. J. Campbell, and R. Wyatt, *Proc. SPIE* **1993**, 2044, pp.55.

[36] J. Albert, B. Malo, F. Bilodeau, D. C. Johnson, K. O. Hill, Y. Hibino, and M. Kawachi, *Optics Letters* **1994**, 19, pp.387.

[37] P. E. Dyer, R. J. Farley, R. Gied, K. C. Byron, and D. Reid, *Electron Letters* **1994**, 30, pp.860.

[38] K. O. Hill, B. Malo, F. Bilodeau, D. C. Johnson, and J. Albert, *Applied Physics Letters* **1993**, 62, pp.1035.

[39] D. Z. Anderson, V. Mizrahi, T. Erdogan, and A. E. White, *Proceedings of the Conference on Optical Fibre Communication, OFC'93, Technical Digest,* **1993**, p.68.

[40] B. Malo, K. O. Hill, F. Bilodeau, D. C. Johnson, and J. Albert, *Electron Letters* **1993**, 29, pp. 1668.

[41] A. D. Kersey, M. A. Davis, H. J. Patrick, M. LeBlanc, K. P. Koo, C. G. Askins, M. A. Putnam, and E. J. Friebele, *IEEE Journal of lightwave Technology* **1997**, 15, 1442-1463.

[42] B. Ball, and W. W. More, *Optics Letters* **1992**, 17, 420-422.

[43] A. Othonnos, A. T. Alavie, S. M. Serge, S. E. Karr, and R. M. Measures, *Optical Engineering* **1993**, 32, 2841-2846.

[44] A. T. Alavie, S. E. Karr, A. Othonos, and R. M. Measures, *IEEE Photonics Technology Letters* **1993**, 5, 1112-1114.

[45] K. O. Hill, F. Bilodeau, and S. Faucher, B. Malo, D. C. Johnson, *Electronics Letters* **1991**, 27, 1548-1550.

[46] G. Laffont and P. Ferdinand, *Measurement Science and Technology* **2001**, 12, 765–770.

[47] Williams, J. A. R., I. Bennion, K. Sugden, and N. J. Doran, *Electronics Letters* **1994**, 30, 985-987.

[48] R. Kashyap, S. V. Chernikov, P. F. Mckee, and J. R. Taylor, *Electronics Letters* **1994**, 30, 1078-1080.

[49] R. W. Fallon, L. Zhang, A. Gloag, and I. Bennion, *Electronics Letters* **1997**, 33, 1997, 705-706.

[50] M. A. Putnam, G. M. Williams, and E. J. Friebele, *Electronics Letters* **1995**, 31, 309-311.

[51] M. Leblanc, S. Y. Huang, M. Ohn, R. M. Measures, A. Guemes, and A. Othonos, *Optics Letters* **1996**,.21, 1405-1407.

[52] S. Huang, M. Leblanc, M. M. Ohn, and R. M. Measures, *Applied Optics* **1995**, 34, 5003-5009.

[53] T. Erdogan, *IEEE Journal of lightwave Technology* **1997**, 14, 1277-1294

[54] M. Born and E. Wolf, "*Principles of Optics.*" New York: Pergamon, **1987**, sec. 8.6.1, Eq. (8).

[55] A. Yariv, *IEEE Journal of Quantum Electronic* **1973**, QE-9, 919–933.

[56] H. Kogelnik, "*Theory of optical waveguides*," in *Guided-Wave Optoelectronics*, T. Tamir, Ed. New York: Springer-Verlag, 1990.

[57] A. Othonos and K. Kalli, "Fibre Bragg gratings Fundamentals and Applications in Telecommunications and Sensing," 1999, (Boston, MA: Artech House), 98–99

[58] Daniel C. Betz, Graham Thursby, Brian Culshaw, and Wieslaw J. Staszewski, *IEEE Journal of Lightwave Technology* **2006**. 24, 1019-1026.

[59] J. Botsis, L. Humbert, F. Colpo and P. Giaccari, *Optics and Lasers in Engineering* **2005**, 43, 491–510.

[60] A. D. Kersey, T. A. Berkoff, and W. W. Morey, *Optics Letters* **1993**, 18, 1370-1372.

[61] A Fernandez Fernandez, F Berghmans, B Brichard, P Megret, M Decreton, M Blondel and A Delchambre, *Measurement Science and Technology* **2001**, 12, 1–4.

[62] Jaehoon Jung, Hui Nam, Byoungho Lee, Jae Oh Byun, and Nam Seong Kim, *APPLIED OPTICS* **1999**, 38, 2752-2754.

[63] Gordon M. H. Flockhart, Robert R. J. Maier, James S. Barton, William N. MacPherson, Julian D. C. Jones, Karen E. Chisholm, Lin Zhang, Ian Bennion, Ian Read, and Peter D. Foote, *APPLIED OPTICS* **2004**, 43, 2744-2751.

[64] G. Meltz and W.W.Morey, *Proceedings SPIE* **1991**, 1516, 185-199.

[65] P. Kronenberg, P. K. Rastogi, P. Giaccari, and H. G. Limberger, *Optics Letters* **2002**, 27, 1385-1387.

[66] Teck L. Yeo, Tong Sun, Kenneth T. V. Grattan, David Parry, Rob Lade, and Brian D. Powell, *IEEE Sensor Journal* **2005**, 5, 1082-1089.

[67] Xingfa Dong, Yonglin Huang, Kewei Lang, Weigang Zhang, Guiyun Kai, Xiaoyi Dong, *Microwave and Optical Technology Letters* **2004**, 42, 474 – 476.

[68] Wojtek J. Bock and Wacław Urbańczyk, *Applied Optics* **1998**, 37, 3897-3901.

[69] Y. S. Hsu, Likarn Wang, Wen-Fung Liu, and Y. J. Chiang, *IEEE Photonics Technology Letters* **2006**, 18, 874-876.

[70] Bao-Jin Peng, Yong Zhao, Jian Yang and Mingguo Zhao, *Measurement* **2005**, 38, 176–180.

[71] Chun-Liu Zhao, Xiufeng Yang, M. S. Demokan, and W. Jin, *Journal of Lightwave Technology* **2006**, 24, 879-883.

[72] A. Iadicicco, S. Campopianoa, A. Cutoloa, M. Giordanob and A. Cusanoa, *Sensors and Actuators B* **2006**, 120, 231–237.

[73] Xuewen Shu, Bashir A. L. Gwandu, Yu Liu, Lin Zhang, Ian Bennion, *Optics Letters* **2001**, 26, 774-776.

[74] Agostino Iadicicco, Stefania Campopiano, Antonello Cutolo, Michele Giordano, and Andrea Cusano *IEEE Photonics Technology Letters* **2005**, 17, 1250-1252.

[75] Jaw-Luen Tang and Jian-Neng Wang, *Sensors and Transducers* **2006**, 68, 597-605.

[76] M. Song, S. B. Lee, S. S. Choi, and B. Lee, *Optical Fiber Technology* **1997**, 3, 194–196.

[77] M. G. Xu, J.-L. Archambault, L. Reekie and J. P. Dakin, *Electronics Letter* **1994,** 30, 1085–1087.

[78] S.W. James, M.L. Dockney and R.P. Tatam, *Electronics Letter* **1996,** 32, 1133–1134.

[79] M Song, B Lee, SB Lee, and SS Choi, *Optics Letters***1997** , 22, 790–792.

[80] O Frazao, and L Ferreira, *Journal of Optics A: Pure and Applied Optics* **2005**, 7, 427–430.

[81] C. Caucheteur, S. Bette, H. Ottevaere, T. Nasilowski, M. Wuilpart, F. Berghmans, H. Thienpont, P. Mégret, *Proceeding SPIE* **2005**, 309-312.

[82] S Oh, W Han, U Paek, and Y Chung, *Optics Express* **2004**, 12, 724-729.

[83] C. Caucheteur, F. Lhommé, K. Chah, M. Blondel and P. Mégret, *Optics and Lasers in Engineering* **2006**, 44, 411–422.

[84] AD Kersey and A Dandridge, *Proceeding SPIE* **1988**, 985, 113–116.

[85] T. A. Berkoff, *et al. Proceeding SPIE* **1995**, 2444, 288-294.

[86] Askins, Charles G., Putnam, Martin A., and Friebele, E. Joseph, *Proceeding SPIE* **1995**, 2444, 257-266.

[87] E J Friebele, *et al.*, *Smart Materials and Structures* **1999**, 8, 813–838.

[88] Zhi Zhou, Thomas W. Graver, Luke Hsu, Jin-ping Ou, *Pacific Science Review* **2003**, 5, 116-121

[89] Yoji Okabe, *et al. Smart Materials and Structures* **2002**, 11, 892–898.

[90] Leif Bjerkan, "Application of fibre-optic Bragg grating sensors in monitoring environmental loads of overhead power transmission lines", APPLIED OPTICS, Vol. 39, No. 4, 1 February 2000

[91] Vincent P. Wnuk, Alexis Mendez, Steve Ferguson and Tom Graver, *Proceeding SPIE* **2005**, 5758, 46-53.

[92] P. St. J. Russel, *et al.* "Fibre gratings," *Physics World* **1993**, Oct., 41-46.

[93] G. B. Hocker, *Applied Optics* **1979**, 18, 1445-1448.

[94] "Pyralin Product Information," HD MicroSystems (2001).

[95] A.T. Alavie, R. Maaskant, R. Stubbe, A. Othonos, M. Ohn, B. Sahlgren, R.M. Measures, *SPIE* **1995**, 2444, 528-535.

[96] F.P. Mallinder, B.A. Proctor, *Physics of Chemistry of Glasses* **1964**, **5**, 91-103.

[97] K. Sager, A. Schroth, A. Nakladal, and G. Gerlach, *Sensors and Actuators A* **1996**, 53, 330–334.

[98] A. Fick, *Ann. Physik* **1855**, Leipzig, 170, pp59

[99] N. Mohammad, W. Szyszkowski, W. J. Zhang, E. I. Haddad, J. Zou, W. Jamroz, and R. Kruzelecky, *IEEE Journal of Lightwave Technology* **2004**, 22, 2001-2013.

[100] Mrotek JL, Matthewson MJ, Kurkjian CR, *IEEE Journal of Lightwave Technology* **2001**, 19, 988-993.

[101] B. Budiansky, D. C. Drucker, G. S. Kino and J. R. Rice, *Applied Optics* **1979,** 18, 4085–4088

[102] A. Bertholds, and R. Daendliker, *IEEE Journal of Lightwave Technology* **1998**, 6, 17-20.

[103] A. D. Kersey, T. A. Berkoff, and W. W. Morey, *Optics Letters* **1993**, 18, 72–74.

[104] M. Xu, J. L. Archambault, L. Reekie, and J. P. Dakin, *Electron Letters* **1996**, 30, pp. 1085–1087.

[105] H. J. Patrick, G. M. Williams, A. D. Kersey, J. R. Pedrazzani, and A. M. Vengsarkar, *IEEE Photonics Technology Letters* **1996**, 8, 1223–1225.

[106] S. E. Kanellopoulos, V. A. Handerek, and A. J. Rogers, *Optics Letters* **1995**, 20, 333–335.

[107] S. W. James, M. L. Dockney, and R. P. Tatam, *Electron Letters* **1996**, 32, pp. 1133–1134.

[108] T. Erdogan, V. Mizrahi, *Journal of the Optical Society of America B* **1994**, 11, 2100-2105.

[109] A. M. Vengsarkar, Q. Zhong, D. Inniss, W. A. Reed, P. Lemaire, S. G. Kosinski, *Optics Letters* **1994**, 19, 1260-1262.

[110] R. M. Craig, S. L. Gilbert, and P. D. Hale, *IEEE Photonics Technology Letters* **1998**, 16, 1285–1294.

[111] M. Wuilpart, C. Caucheteur, S. Bette, M. Blondel, P. Mégret, *Optics Communications* **2005**, 247, 239-245.

[112] J. Noda, K. Okamoto, and Y. Sasaki, *IEEE Journal of Lightwave technology* **1986**, LT-4, pp.1183.